Development of Ni catalysts with low metal content and improved stability in the dry reforming of methane to syngas

Dissertation

zur Erlangung des akademischen Grades
doctor rerum naturalium (Dr. rer. nat.)
an der Mathematisch-Naturwissenschaftlichen Fakultät
der Universität Rostock

vorgelegt von
Quan Luu Manh Ha
aus Ho-Chi-Minh Stadt, Vietnam
Rostock, 2019

https://doi.org/10.18453/rosdok_id00002741

Gutachter:

1. Gutachter: Prof. Dr. Udo Kragl

Institut für Chemie, Abteilung Technische und Analytische Chemie, Universität Rostock

2. Gutachter: Prof. Dr. Martin Muhler

Lehrstuhl für Technische Chemie, Ruhr-Universität Bochum

Jahr der Einreichung: 2019

Jahr der Verteidigung: 2019

Erklärung

Hiermit erkläre ich, dass ich die vorliegende Arbeit selbstständig verfasst und keine anderen als die angegebenen Quellen und Hilfsmittel benutzt zu habe.

Rostock, 26.04.2019

Quan Luu Manh Ha

Acknowledgment

I would like to thank God Almighty for giving me health and a chance in my life to meet and work with the wonderful people during my PhD time in Germany.

First of all, I would like to express my gratefulness to PD Dr. Andreas Martin who provided me an excellent opportunity to be a PhD student in LIKAT and supervising me as well in my hard time in the initial period. Besides, I would like to send my thankfulness to Prof. Dr. Udo Kragl for the great supervision with remarkable provision and encouragement during my researching time.

I would like to warmly acknowledge Dr. Udo Armbruster with special appreciation for his very precious guidance and advice by his own practical experience in scientific works. My ideas and expectations in the whole of this research cannot be fruitful without his managing and supporting efforts. I am delighted to learn from him the strongly motivated contribution in the scientific profession that will be an excellent example for my future career. At the same time, I also want to thank Dr. Sebastian Wohlrab for his supports with the necessary improvements and suggestions on my publications and presentations.

I would like to give my appreciation to Dr. Carsten Kreyenschulte for his hard-working experiments and careful explanations to my concerns correlating with STEM measurements. Further thanks to Dr. Henrik Lund for the measurements and important instructions relating to XRD characterization, Dr. Stephan Bartling for XPS experiments, Mrs. Anja Simmula for the ICP-OCS measurements, Mrs. Astrid Lehmann for element analyses.

I also thank Dr. Huyen T. Vuong for all of her supports from my initial PhD time, not only with her contribution to the UV-VIS-DR results in my thesis and other work-relating problems but also in normal life caring, like a sister. The sincere thanks go to my office-mates Dr. Hanan Atia and Reinhard Eckelt who have always been supportive with beneficial academic guidance and technical solutions in my daily laboratory works besides their delicate help with TPX and BET measurements. Also, I want to thank all other group-mates including Dr. Angela Köckritz, Ms. Regina Bienert, Dr. Elka Kraleva, Mrs. Amely Täufer, Dr. Katja Neubauer, Mr. Markus Vogt, and Mr. Tom Brunzel for the warm atmosphere with their compassion and friendship. We all have great talks, meetings and parties that are all especially memorable to me about my time in LIKAT.

The further compliments go to all members of the LIKAT administration, workshops, and purchasing department for their assists and friendly working atmosphere.

I am also grateful for the financial support from German Academic Exchange Service (DAAD) and additional support from Vietnam Petroleum Institute (VPI).

I want to give many thanks to the Vietnamese friends in Rostock for the warm events that I will never forget.

Finally, I want to give my deepest gratitude to my parents, my brother and my fiancée, who always give me their unconditional love with the sacrifice, patience and meaningful encouragement throughout the years of my life here for PhD studying.

Zusammenfassung

Dry Reforming (CO_2-Reforming von Methan, DRM) wandelt diese beiden Treibhausgase miteinander in Synthesegas (H_2, CO) mit hohem wirtschaftlichem und ökologischem Nutzen um. Die Reaktion wurde zunächst an Katalysatoren mit niedrigem Ni-Gehalt auf verschiedenen Mg-Al-Mischoxiden untersucht, um die Deaktivierungsmechanismen aufzuklären und stabile wettbewerbsfähige Katalysatoren sowohl für milde (stöchiometrische) als auch CH_4-reiche Bedingungen zu erhalten, wobei letztere perspektivisch interessant sind, um die direkte Umwandlung von Biogas oder bestimmten Erdgasen nachzuahmen.

Diese geträgerten Ni-Katalysatoren wurden aus Hydrotalcit-Vorläufern mit verschiedenen Zusammensetzungen und Strukturen hergestellt. Die Katalysatoren wurden letztendlich durch Naßimprägnierung und Kalzinierung bei hoher Temperatur hergestellt. Der Ni^{2+}-Precursor wurde mit Zitronensäure (CA) komplexiert und/oder mit La^{3+}, Sc^{3+} oder Gd^{3+} coimprägniert und der Ni-Gehalt wurde auf 2,5 Gew.-% eingestellt. Die Materialien wurden mit N_2-Physisorption, Röntgenbeugung, temperaturprogrammierter Reduktion, Röntgenphotoelektronen-Spektroskopie, UV-Vis-Diffus-Reflexionsspektroskopie und Rasterelektronen-Mikroskopie mit energiedispersiver Röntgenspektroskopie charakterisiert.

DRM läuft oberhalb von 600 °C und die Katalysatoren deaktivieren durch Metallagglomeration oder Verkokung (CH_4-Spaltung, CO-Disproportionierung). Letztere kann zur Reaktorblockade führen. Die Desaktivierungspfade hängen von den Reaktionsbedingungen ab und sind bei Katalysatoren mit niedrigem Ni-Gehalt gut unterscheidbar. $Ni/Mg_{1,3}AlO_x$, mit Ni-Spezies eingebettet in ein Mischoxid aus MgO und Al_2O, zeigte selbst bei 500 °C hohe DRM-Aktivität. Dieser Katalysator neigte jedoch zur Verkokung im stöchiometrischen DRM bei niedriger Temperatur oder im CH_4-reichen DRM und litt unter Agglomeration aufgrund geringer Ni-Dispersion und niedriger Metall-Träger-Wechselwirkung.

Durch verschiedene Modifikationen wurden Katalysatoren mit hoher Leistung und Stabilität für verschiedene DRM-Bedingungen entwickelt. Im stöchiometrischen DRM wies der mit La und CA modifizierte Ni-Katalysator die höchste Stabilität gegenüber der Ni-Reoxidation und der Agglomeration auf. Dieser Katalysator zeigte außerdem eine niedrige Verkokung und erzielte über 160 h eine hohe Aktivität und Produktivität für Wasserstoff (118 $L/(g_{cat} \times h)$). Im CH_4-reichen DRM zeigte der auf La und CA basierende Ni-Katalysator ($Mg_{1,3}AlOx$ Support bei 1000 °C vorbehandelt), eine deutlich verbesserte Verkokungsbeständigkeit. Ein Gd- und Ni-dotierter Katalysator ($Gd.Ni/Mg_{1,3}AlO_x$) führte ebenfalls zu verminderter Verkokung. Beide Katalysatoren erzielten hohe Aktivität über einen Zeitraum von 100 h mit einer Kohlenstoffablagerung von etwa 6 Gew.-%. Diese Ergebnisse sind vielversprechend für die Entwicklung von Ni-Katalysatoren für das DRM im industriellen Maßstab.

Abstract

Dry reforming also known as CO_2 reforming of methane (DRM) is a process that simultaneously transforms these two greenhouse gases into syngas (H_2, CO) with high economic and environmental benefit. This reaction was firstly studied over catalysts with low Ni content supported on various Mg-Al mixed oxides to identify different deactivation mechanisms and to develop stable and competitive DRM catalysts at either mild (stoichiometric) or severe (CH_4-rich) conditions with the latter having the perspective to mimic the direct conversion of biogas or specific natural gases.

Named Ni catalysts supported on Mg-Al mixed oxides were prepared from hydrotalcite precursors with various compositions and structures. The final catalysts were then obtained by wet impregnation followed by calcination at high temperature. The precursor Ni^{2+} was either complexed with citric acid (CA) and/or co-impregnated with La^{3+}, Sc^{3+} or Gd^{3+} and the Ni content in final catalyst was fixed at 2.5 wt%. The solids were characterized using N_2 physisorption, X-ray diffraction, temperature-programmed reduction, X-ray photoelectron spectroscopy, UV-Vis diffuse reflectance spectroscopy, and scanning transmission electron microscopy with energy-dispersive X-ray spectroscopy.

DRM runs at temperatures above 600 °C, and the catalysts deactivate due to metal particle sintering or coking (methane decomposition, CO disproportionation). The latter effect may lead to reactor blockage. The deactivation pathways depend on the reaction conditions and can be differentiated well on low Ni content catalysts. $Ni/Mg_{1.3}AlO_x$ with Ni species embedded in a solid solution of MgO and Al_2O_3 shows high DRM activity even at low temperature (500 °C). However, this catalyst was prone to carbon deposition, in stoichiometric DRM at low temperature or in CH_4-rich DRM, and suffered from metal agglomeration due to poor Ni dispersion and low metal support interaction (MSI).

By applying different modification routes catalysts with exceptional performance and stability at different DRM conditions were developed. In stoichiometric DRM, the Ni catalyst modified with La and CA-assisted synthesis showed the highest stability against both Ni re-oxidation and agglomeration. This catalyst revealed low coking rate and maintained high activity over 160 h with outstandingly high productivity of hydrogen (118 $L/(g_{cat} \times h)$). In severe CH_4-rich DRM, the La- and CA-modified Ni catalyst supported on thermally pre-treated $Mg_{1.3}AlO_x$ at 1000 °C revealed highest coking resistance. Likewise, $Gd.Ni/Mg_{1.3}AlO_x$ exposed good carbon suppression and both catalysts accomplished high and quite stable activity over 100 h on stream with limited carbon deposition (approx. 6 wt%). These results are promising for Ni catalyst development for industrial-scale DRM.

Contents

List of abbreviations

ABF	**A**nnular **B**right **F**ield
a.u.	**A**rbitrary **u**nits
BD	**B**ou**d**ouard reaction
BET	**B**runauer-**E**mmet-**T**eller
CA	**C**itric **a**cid
CT	**C**harge **t**ransfer
DR	**D**iffuse **r**eflectance
DRM	**D**ry **r**eforming of **m**ethane
EDXS	**E**nergy-**d**ispersive **X**-ray-**s**pectrometer
Eq.	**Eq**uation
GC	**G**as **c**hromatography
GHG	**G**reen **H**ouse **G**as
GHSV	**G**as **h**ourly **s**pace **v**elocity
GTL	**G**as **t**o **l**iquid
HAADF	**H**igh-**A**ngle **A**nnular **D**ark **F**ield
H_2-TPR	**H**ydrogen **t**emperature-**p**rogrammed **r**eduction
ICDD	**I**nternational **C**entre for **D**iffraction **D**ata
ICP-OES	**I**nductively **c**oupled **p**lasma **o**ptical **e**mission **s**pectrometry
LMCT	**L**igand to **m**etal **c**harge **t**ransfer
MD	**M**ethane **d**ecomposition (**c**racking) reaction
MS	**M**ass **s**pectrometry
MSI	**M**etal **s**upport **i**nteraction
RE	**R**are **e**arth elements (La, Sc, Gd)

RWGS	**R**everse **w**ater **g**as **s**hift
STEM	**S**canning **t**ransmission **e**lectron **m**icroscopy
TOS	**T**ime **o**n **s**tream
TPR	**T**emperature-**p**rogrammed **r**eduction
UV-Vis	**U**ltra**v**iolet-**vis**ible
UV-Vis-DRS	**D**iffuse **r**eflectance **u**ltra**v**iolet-**vis**ible **s**pectroscopy
Vol%	**V**olume percentage
Wt%	**W**eight percentage
XPS	**X**-ray **p**hotoelectron **s**pectroscopy
XRD	**X**-**r**ay **d**iffraction

1 Motivation and Objective

1.1 Motivation

The global energy demand is rapidly growing adapted to human activities, and about 86% thereof is covered by fossil fuels at the recent time (2015) [1]. However, such societal behaviour leads to the unavoidable increasing of anthropogenic greenhouse gas (GHG) emissions causing the worldwide environmental problems, mostly known with the rising of global temperatures and the increasing volatility of global weather patterns [2, 3]. CO_2 is the greenhouse gas (GHG) that has the largest contribution to climate change due to its long live and abundance in the atmosphere [4, 5]. Before 1950, atmospheric carbon dioxide was never higher than 320 ppm [6, 7]. However, in 2017, it reached 405 ppm with growth rate risen from 0.6 ppm/year in the early 1960s to an average of 2.3 ppm/year during the past ten years [5]. Such increases of atmospheric carbon dioxide concentration are predominantly responsible for the total energy imbalance that is causing Earth's temperature to rise [2]. As a result, there were attempts to limit CO_2 emission from industry activities as well as to reduce atmospheric CO_2 by applying technological progress for CO_2 capture and storage (CCS) and utilization (CCU) [8, 9]. However, CO_2 is also a natural source of carbon that can be used as a building block for chemical processes that may achieve both commercial and environmental values [10]. Among these are the CO_2 transformation via hydrogenation to form oxygenates and/or hydrocarbons (such as methanol synthesis) or via reforming into syngas or synthesis of organic carbonates using preferably heterogeneous oxide catalysts [11].

CH_4 is the second major GHG that is mainly emitted from two sources: from naturally occurring activities (40%) and anthropogenic activities (60%) [5, 12]. In oil and gas processing, CH_4 is the main component of natural gas (NG) which is still the preferred feedstock for energy market [13] firstly due to its abundance, with total proved reserves of 193.5 trillion cubic meters (2017) [14]. Besides, usage of CH_4 is also less complicated and expensive in industrial processes compared to other fossil sources [15]. Regarding the composition, NG may contain a minor amount of other hydrocarbons and also include inert molecules such as nitrogen and carbon dioxide [16]. For instance, in 2011 Vietnam discovered the “Blue Whale” gas field with a large reserve of about 150 billion m^3 of high content CO_2 (~ 30 vol%) natural gas available for power generation and industrial purposes [17, 18].

Away from the natural gas reserves, methane can also be generated from biogas sources produced from the anaerobic decomposition of organic material. These sources comprise different compositions but mainly concentrated CH_4 and CO_2. For example, some landfill gas contains 40‑45% methane and 55‑60% carbon dioxide by volume [19] while biogas in Germany is expected to have 50‑75% and 25‑45% by volume of methane and carbon dioxide, respectively [2].

Rather than energy purposes mainly for industrial heating, residential, and electricity generation, there are extensive industry applications and researches implemented to indirectly or directly convert methane into chemicals, liquid fuels or higher hydrocarbons through different gas to liquid GTL technologies [2, 9, 20, 21]. However, the CH_4 direct oxidative conversion processes have low yields and are not yet industrialized [21, 22]. In contrast, indirect NG conversions to liquids can be achieved via several processes, such as widely deployed Fischer-Tropsch (FT) technologies, Gas to methanol, Gas to dimethyl ether and Gas to olefins, resulting in a range of high-value products [20]. The first step to apply these technologies is the production of synthesis gas (syngas) from NG, as being the preferred starting material in these large-scale chemical syntheses [23]. In this step, the carbon and hydrogen from the CH_4 and transformed into carbon monoxide and hydrogen [20]. There are three common processes applicable for such transformation which are steam reforming of methane (Eq. 1), partial oxidation of methane with oxygen or air (Eq. 2) and dry reforming of methane with carbon dioxide (Eq. 3) with equations described below [2, 24, 25]:

$$H_2O + CH_4 \rightarrow CO + 3\ H_2 \qquad \Delta H_{298} = 206\ kJ/mol \qquad \text{(Eq. 1)}$$

$$\frac{1}{2}\ O_2 + CH_4 \rightarrow CO + 2\ H_2 \qquad \Delta H_{298} = -35.6\ kJ/mol \qquad \text{(Eq. 2)}$$

Steam reforming and partial oxidation of methane are both well-established technologies for producing syngas from NG in the industry but still also encounter some limitations relating to CO_2 emission and requirement of water sources to generate steam [26, 27]. Methane steam reforming generates a syngas with high ratio of $H_2/CO = 3$ which may be suitable for H_2, NH_3 or urea synthesis and also applicable for Fischer−Tropsch or methanol synthesis ($H_2/CO = 2$) with the availability of combined processes adjusting the H_2/CO ratio [20, 26, 28-31]. Partial oxidation reaction can be applied to produce syngas from CH_4 [32]. This partial oxidation of methane offers some benefits, such as high conversion, high selectivity and very short residence time [33]. However, this reaction has the exothermic nature that may generate hot spots on catalyst due to slow heat removal, leading to the operation difficulty and complexity.

Unlike steam reforming and partial oxidation, dry reforming also known as CO_2 reforming of methane (DRM) has not been industrialized. However, the reaction gathers attention because it transforms two stable and refractory molecules over various metal catalysts into syngas with equimolar ratio of H_2 and CO. Besides, as CO_2 extraction is economically unprofitable, DRM can be considered to process aforementioned CO_2-rich gases with a wide range of CO_2 content up to 70% [3, 34].

However, DRM is a highly endothermic reaction requiring high temperature that on the other side leads to serious catalyst deactivation mainly due to the fast agglomeration of metal active sites and high coking rate [2, 35]. These obstacles are the main reasons that delay this promising process to be commercialized. There were made many attempts to improve the coking resistance of DRM catalysts, e. g., dispersion improvement by supporting the active metals on suitable supports, controlling the metal particle size and selecting suitable modification/promotion routes [2].

DRM was most commonly studied on Ni-based catalysts due to their high activity, obtainability, and acceptable price compared to other transition and noble metals [36-38]. Particle size plays an important role in the limitation of carbon deposition and for achieving higher catalytic activity and stability in DRM [39]. The small Ni particle size can be generated by reducing the metal content in the catalyst [40]. Therefore, by preparing catalysts with low Ni content supported on suitable metal oxides preferring strong metal-support interaction, highly dispersed Ni particles can be obtained which are beneficial for catalyst performance and stability against serious metal migration and carbon deposition [17, 40, 41]. While alumina was commonly applied as support material of active species in DRM, Ni/Al_2O_3 catalyst systems may encounter problems relating to low basicity, reducibility and stability under harsh reaction conditions [2, 3, 42]. The addition of MgO to such material results in a mixed oxide support that can be used to prepare the Ni catalyst with improved performance via strong metal support interaction and increased basicity [42-44]. However, as less focused in DRM studies, low Ni content catalyst might be less active due to the partial formation of stable but poorly active phases, such as $NiAl_2O_4$ spinel or NiO-MgO solid solution [45-47][34]. These structures may limit the availability of Ni as the active species for the reaction, subsequently decreasing the activity. Besides, even the stability in DRM of these Ni catalysts with low metal loading is controversial. Opposing to those results in the literature claiming the benefits of low Ni content in coking limitation and good performance, there were several recent investigations stating the deactivation of such Ni catalysts. The authors in the study [48] recognized that small metal particles achieved with 2 wt% Ni/MgO are more prone to be sintered and oxidized during the reaction but without clear proofs from their characterization. On the other hand, the investigation [49] concluded that the gradual deactivation of 2.5 wt% Ni catalyst supported on modified Mg-Al mixed oxide is the result of “mild” coking behaviour although the carbon contents were quite negligible and this study itself later found evidence for sintering of Ni particles. As a result, the performance and deactivation mechanism of these low Ni catalysts was still not clearly confirmed, leaving the gaps for their application in DRM.

Coking resistance is the next factor to be considered. Suitable modifiers/promoters that are able to adjust the acidity/basicity or oxidation/reduction manners of the catalyst could be applied to improve the catalyst performance and inhibit carbon deposition [2]. Generally, noble metals are effective for Ni catalyst promotion in order to stabilize Ni in the metallic state against re-oxidation by CO_2 and to improve the catalyst resistance to carbon deposition, but are expensive [50]. Adding rare earth metal oxides would strongly promote the CO_2 dissociative adsorption that enhances the availability of surface oxygen species which contribute significantly to both activity and coking resistance of a DRM catalyst [51, 52]. However, it was reported that the addition of such elements could result in lower Ni dispersion due to their commonly large sizes [53]. Therefore, a multi-agent modification routine might be preferred.

The addition of chelating agents is a second potential approach to modify the catalyst preparation procedure. The availability of such organic additives leads to the establishment of metal complexes which are more evenly and stably spread over the solid support during both the impregnation and drying steps [54, 55], finally heading to higher metal dispersion with smaller metal particle size, inhibiting the rapid coking [56]. It should be noted regarding the thermodynamics at temperatures higher than 700 °C, that methane cracking is the main source of carbon deposition [57]. However, the gasification is also favoured at such temperature, offering the potential of CO_2 to remove carbon from such methane decomposition. As a result, the benefits of catalyst modifications in terms of coking resistance in high-temperature DRM maybe unclear. In order to evaluate such carbon resistance, it was also suggested to conduct the stoichiometric DRM at lower temperature [57] although probably leading to low reactants conversions and H_2 selectivity.

Regarding the sources of CH_4 at industrial scale, natural gas and biogas are the most focused feedstocks that provide wide ranges of CH_4 and CO_2 concentrations. It was reported that these CH_4 sources might include CO_2 with contents lower than 5% [9] in case of natural gas but from 25% up to 55% [58] in case of biogas, and both cases require suitable processing technologies. Therefore, in many cases, the DRM studies on stoichiometric CH_4:CO_2 ratio found in literature may not be applicable for processing these methane sources. Consequently, the influence of such ratio on the catalyst activity and stability should be studied in order to evaluate the potential application of Ni catalysts for that purpose. Particularly, the high CH_4/CO_2 ratio (>1) can imitate natural gas (CO_2 content up to 30%) which is observed in a promising exploration project in Vietnam [59], offering high economic value for this developing country. It should be noted that DRM conducted with such feedstock, especially at high temperature, can reduce the effect of reverse water gas shift reaction and increase H_2 productivity (as the H percentage in the feed is higher) but creates operational complications due to serious carbon deposition [2].

Besides, carbon gasification could be hampered in such DRM due to the lack of CO_2 in the feed, leaving the necessity to evaluate different coking resistance pathways of modified Ni catalysts.

1.2 Objective

There is a vital need to figure out the suitable formulations and preparation routines that both make active and stable catalysts for DRM, especially when the severe but application-relevant conditions are applied. It is the main task of this thesis to investigate whether it is possible to apply MgO-Al_2O_3 mixed oxides as supports for low Ni content catalysts in DRM wherein the catalyst can maintain high activity and low carbon deposition in long-term tests at different CH_4/CO_2 ratios and reaction temperatures. Moreover, catalyst deactivation, especially the coking mechanisms, as well as the relations between the catalysts' physicochemical properties and performance, must be studied by a combination of proper characterization technologies and reaction conditions. To this end, the following strategies will be employed:

- Varying the hydrotalcite Mg/Al ratios during preparation and the calcination temperatures to obtain suited support for Ni catalyst that has high activity in stoichiometric DRM (Chapter 4).

- Modifying the Ni catalyst by adding rare earth metal oxides and chelating agent in impregnation steps to stabilize Ni catalyst without significantly reducing its activity (chapters 5 and 7).

- Applying non-stoichiometric CH_4/CO_2 ratio to study the application-related performance of Ni catalysts (chapters 6 and 7).

- Verifying different deactivation effects and studying the coke formation mechanism on low Ni content catalysts by varying the reaction temperature and CH_4/CO_2 ratio (chapters 5 and 6).

- Indicating different measures to augment coking resistance with various catalyst modification routes.

- Investigating the relationship between the catalyst physicochemical properties and performance by characterising the fresh and spent catalysts.

2 State of the Art

2.1 Dry reforming of methane

2.1.1 Thermodynamics

Dry reforming of methane was first thoroughly studied by Fischer and Tropsch in 1928 over Ni and Co catalysts [57]. DRM is a highly endothermic process (higher heat of reaction than that of steam reforming (Eq. 1). This requires high temperatures to maintain the reaction and to achieve the equilibrium conversion to syngas. Indeed, according to Gibbs free energy of DRM (Eq. 4) [60], this reaction can only be spontaneous above 644 °C, assuming $\Delta G = 0$. Furthermore, CH_4 and CO_2 are very stable molecules with high dissociation energy (435 kJ/mol for CH_3-H and 526 kJ/mol for CO-O) and therefore catalysts are required for activation [8]. DRM can be considered as a component/step in exothermic-endothermic reaction cycle systems for transport and storage of energy from renewables or nuclear energy that empower such endothermic process [3, 34]. Besides, the equilibrium for the production of syngas in DRM is affected by the simultaneous influence of the reverse water-gas-shift (RWGS) reaction (Eq. 5) [60].

$$CO_2 + CH_4 \rightarrow 2CO + 2H_2 \qquad \Delta H_{298} = 260.5 \text{ kJ/mol} \qquad \text{(Eq. 3)}$$

$$\Delta G^0 = 258 - 0.28T \text{ (kJ/mol)} \qquad \text{(Eq. 4)}$$

$$CO_2 + H_2 \rightarrow CO + H_2O \qquad \Delta H_{298} = 41 \text{ kJ/mol} \qquad \text{(Eq. 5)}$$

$$\Delta G^0 = -35 + 0.03T \text{ (kJ/mol)} \qquad \text{(Eq. 6)}$$

Therefore, the conversion of CO_2 is always higher than that of CH_4 in DRM and the reaction yields syngas with the H_2/CO ratio lower than unity, which is at first unsuited for the synthesis of long-chain hydrocarbons or oxygenate chemicals [50]. If necessary, higher H_2/CO values for methanol and other Fischer-Tropsch syntheses [8] could be achieved by water-gas-shift reaction in the presence of H_2O to convert CO into CO_2 and H_2 [61].

2.1.2 Reaction mechanism

The kinetics and mechanism of DRM were reviewed in different articles studying several catalyst systems [38, 51]. According to these articles, the DRM mechanism is illustrated in Figure 2.1 and can be briefly summarized as follows:

The first step is the dissociative adsorption of methane wherein it is adsorbed (reversibly or irreversibly depending on the catalyst system), activated and cracked on the metal surface. The dissociation is generally agreed to be one of the slow reaction steps in the reaction sequence. It was found out that steps of the metal crystals are more active for methane cracking than close-packed surfaces and the decomposition of methane preferentially proceeds on small crystal surfaces.

The second (parallel) step is CO_2 adsorption and activation. Most kinetic studies of DRM consider dissociative adsorption of CO_2 in this step, which is important for catalytic activity and stability. For many catalyst systems, the adsorption of CO_2 is a fast step and reaches thermodynamic equilibrium. Adsorption of CO_2 is dissociative on Fe, Ni, Re, Al and Mg surfaces. The activated CO_2 species either transform into surface adsorbed CO and O species or react with surface hydrogen species, which originate from CH_4 decomposition (step 1), via RWGS reaction and surface CO and OH species are formed. Such proposed dissociative adsorption mechanism of CO_2 is likely affected by the presence of surface atoms, reactive oxygen species, oxygen vacancies, oxides of rare earth metals, particularly ceria and lanthana. Besides, highly dispersed metal is expected to exhibit good activity as the metal–support interface is maximized which is the favourite adsorption site for CO_2.

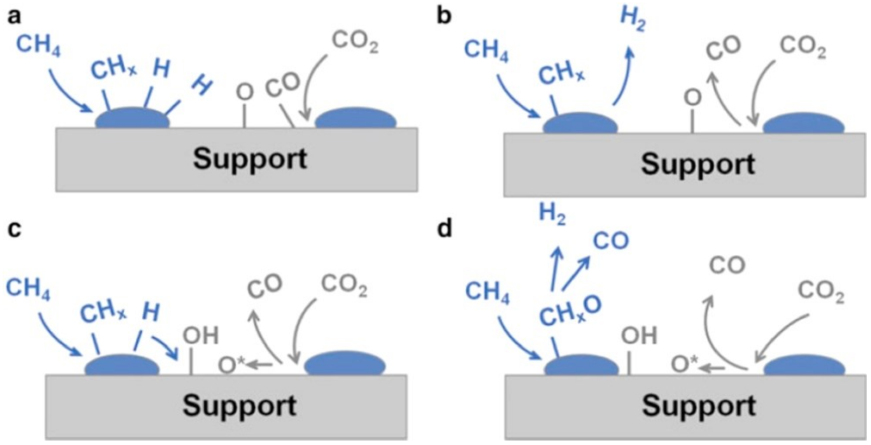

Figure 2.1. Reaction steps in DRM: (a) Dissociative adsorption of CH_4 and CO_2 on metal surface and metal-support interface. (b) Fast desorption of CO and hydrogen. (c) Formation of surface hydroxyls and oxygen spillover. (d) Surface hydroxyls and oxygen species oxidize CH_x species and form CO and H_2. (Republished with permission from ref. [51]. Copyright 2012 Springer New York.)

The oxidation of intermediate CH_x species and CO/H_2 desorption is considered as the final step of the DRM. In this step, surface hydroxyl and/or oxygen species originating from CO_2 migrate on the metal surfaces and react with the hydrogen-depleted CH_x species, forming surface H_2 and CO species. Actually, the origin of such CO species is controversial. Some studies claimed that the surface CH_xO groups appear to be precursors that subsequently convert into CO while others suggest that CO species are formed directly from CH_x. There is another assertion about the reduction of carbonates into CO by carbon. Such CO_3^{2-} species are found generated from CO_2 adsorbed on basic sites, especially rare earth compounds such as metal oxides of La or Gd. Additionally, the catalyst nature and operating conditions also play an important role that makes the reaction mechanism on the surface of the catalysts still uncertain. However, in most of the studies, the formation and/or decomposition of surface CH_xO to CO and H_2, if available, is considered the rate-determining step, while the desorption of CO and H_2 is fast. Therefore, it is more important to indicate the relative rate of slow surface CH_x oxidation step compared to their dissociation. Higher rate of oxidation results in the formation of CH_xO while the opposite order causes the generation of surface C atoms, subsequently accumulating into complex carbonaceous species that lead to catalyst deactivation. The fast deactivation of the catalyst due to coking is a serious issue for the DRM, delaying such process to be commercialized.

2.1.3 Catalyst deactivation

Deactivation of catalysts operating under DRM conditions may occur via different mechanisms such as agglomeration of the metallic phase, poisoning caused by impurities contained in the feed (most commonly H_2S) and the accumulation of carbonaceous deposits [51]. The carbon deposition tendency can be predicted by the ratios of O/C and H/C in the feed. Generally, a higher deposition rate will be observed at lower O/C and H/C ratios [23]. In the case of methane steam reforming ($CH_4/H_2O=1/1$) and partial oxidation of methane ($CH_4/O_2=2$), O/C ratios are both unity and the H/C ratios are 6 and 4, respectively. On the other hand, while the O/C ratio in DRM is also 1, the H/C ratio of the DRM feed mixture is 2 and lower than for the two former reactions. As a consequence, DRM has a higher possibility of carbon accumulation compared to steam reforming and partial oxidation of methane [62].

Considering the sources of the deposited carbon during DRM, there are two side reactions that may run simultaneously with the reforming reaction depending on the operating temperature and reactant partial pressure [50]. These first include CH_4 decomposition (MD) reaction (Eq. 7) into solid carbon on the catalyst surface and H_2. Secondly, the Boudouard (BD) reaction (Eq. 9) occurs where the disproportionation of carbon monoxide leads to the formation of carbon dioxide and surface carbon.

$$CH_4 \rightarrow C + 2H_2 \qquad \Delta H_{298} = 75\ kJ/mol \qquad (Eq.\ 7)$$

$$\Delta G^0 = 92 - 0.11T\ (kJ/mol) \qquad (Eq.\ 8)$$

$$2\ CO \rightarrow CO_2 + C \qquad \Delta H_{298} = -171\ kJ/mol \qquad (Eq.\ 9)$$

$$\Delta G^0 = -167 + 0.17T\ (kJ/mol) \qquad (Eq.\ 10)$$

These C_1 species are subsequently saturated at preferable conditions to generate more complex carbonaceous domains which vary in appearance, reactivity, stability and crystallography [51].

The carbon species deposited during the DRM process can be categorized as C_α, C_β, C_γ, C_v, and C_c which are formed following the proposed mechanism illustrated in (Figure 2.2.) [57]. For example, CO and CH_4 dissociate at the catalyst surface and give C_α, an adsorbed atomic carbon. C_α then reacts to form C_β, representing polymeric amorphous films that react and transform/condense into other types of carbon: C_γ (Ni carbide), C_v (vermicular filaments or whiskers), and C_c (graphite platelet films) with different complexity [63].

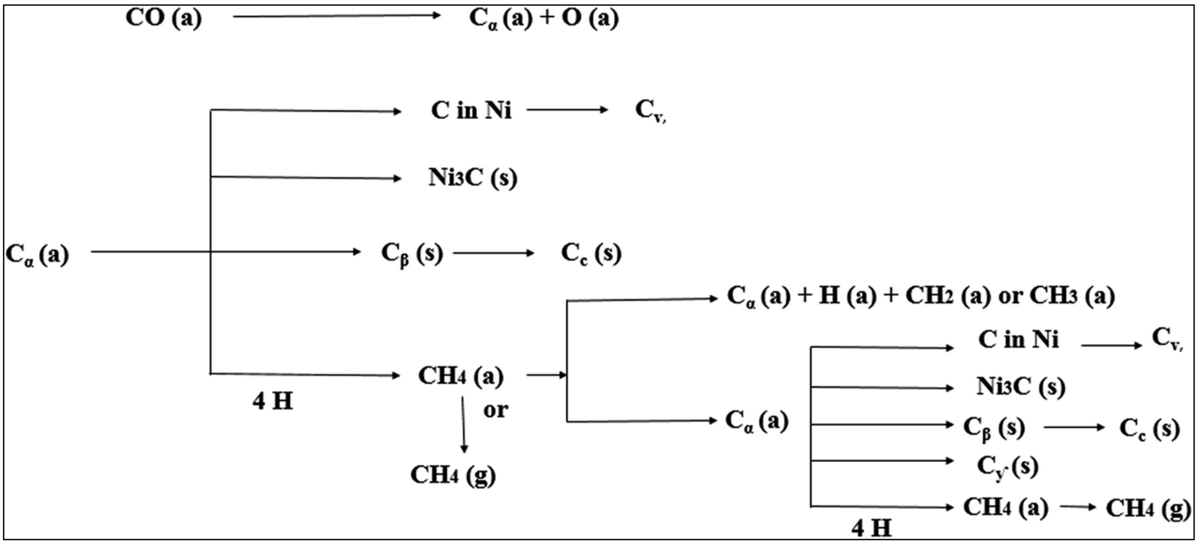

Figure 2.2. Mechanism of carbon formation on the catalyst surface. (Republished with permission from ref. [57]. Copyright 2016 RSC Publishing).

Depending on the carbon growth mechanism and the catalyst system, the accumulation may let particles to be encapsulated or detached from the support that causes the catalyst deactivation. Besides, the high coking rate can result in increasing of the pressure drop or even reactor blockage [51].

Regarding the influence of temperature, the corresponding standard free energies (ΔG^0) indicate the driving force for DRM and other side reactions (Eq. 3) to (Eq. 9). According to the free energy calculations in [60], it can be inferred that DRM preferably proceeds towards syngas formation above 640 °C while the RWGS can run up to 820 °C. The carbon formation can mainly run due to the contribution of MD above 557 °C and of BD below 700 °C. Therefore, coking studies should be implemented in the temperature range of 557–700 °C in order to investigate the influence of both carbon forming reactions. This range can be also seen in the equilibrium data plot (Figure 2.3) calculated by HSC Chemistry 7.1 for the DRM assuming the occurrence of carbon formation [64].

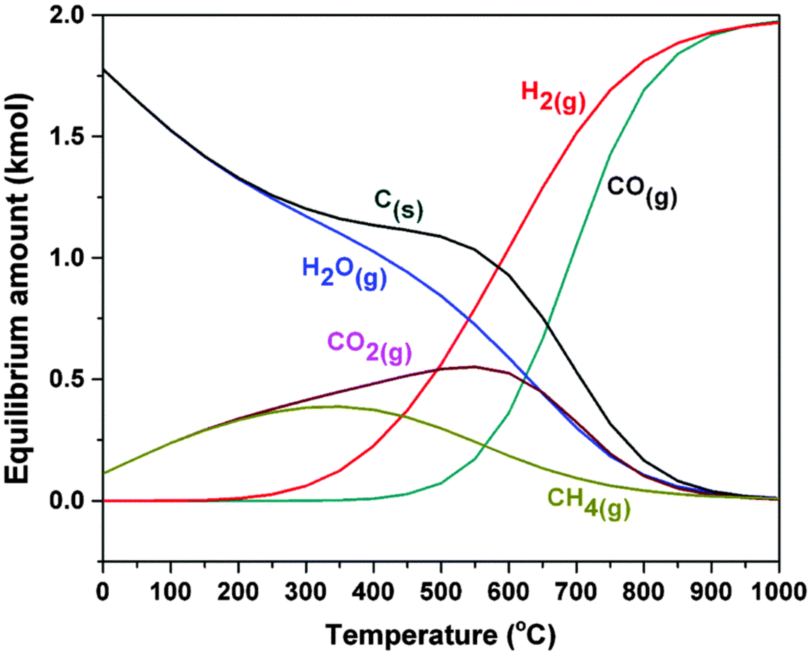

Figure 2.3. Thermodynamic equilibrium plots for DRM at 1 bar, from 0-1000 °C and at inlet feed ratio of CO_2/CH_4 = 1, assuming carbon formation occurs. (Republished with permission from ref. [64]. Copyright 2013 Elsevier.)

Considering the feed composition, it was proposed that in order to minimize the influence of RWGS (Eq. 5) and to increase H_2 yield and selectivity related to H_2O, higher temperature (>750 °C) or higher ratio of CH_4/CO_2 (>1) should be used [18]. As an important additional result, the aforementioned CH_4-rich gases can be processed in DRM with CO_2 being removed completely. However, a higher ratio of CH_4/CO_2 may result in the uncontrolled rising of coking rate that leads to operational complexities [3].

It should be noted that both reactions MD and BD proceed on the metal surface, and the extent of the contribution of each on carbon accumulation also depends on catalyst properties and composition. Therefore, the study of DRM catalyst is essential to enhance not only the catalytic performance but also coking resistance.

2.2 DRM Catalyst

2.2.1 Influence of active site

Dry reforming of methane has been investigated on catalysts with a wide variety of active components including both noble (Pt, Pd, Rh, Ir and Ru) and non-noble metals (Ni, Co and Fe) [65, 66]. Noble metal catalysts gather attention for their excellent coking resistance, stability and activity especially at higher temperature (>750 °C) [67]. However, noble metals with their superior attributes cannot be applied on the industrial scale due to their high costs [66]. From such point of view, non-noble metal-based catalysts turn out to be a proper alternative for DRM due to their low price [65, 68]. Among these, nickel was the most commonly used base metal in DRM-related literature [66] because of its lower cost and high availability [51]. Regarding the DRM catalytic activity, Ni is the only transition metal that is comparable to precious metals [54].

Unfortunately, nickel catalysts encounter fast deactivation arising from coke deposition [69]. The resulting poor stability delays the commercial application of Ni-based catalysts for DRM [54]. Consequently, these catalysts were intensively investigated to overcome the coking problem by adjusting the acidity-basicity or enhancing the Ni dispersion but maintaining the high activity of the Ni-based catalyst systems [66]. This can be achieved via applying basic supports, adding dopants/modifiers, controlling the metal loading, or focusing on preparation method and thermal pre-treatment procedures [2, 51].

2.2.2 Influence of support on catalytic activity

The performance of a catalyst is not only influenced by the nature of the active metals, but also by the supporting materials (or supports) that play a vital role in DRM reaction in the case of nickel catalysts [51, 70]. Basically, the supports are supposed to provide classical properties such as high surface area and mechanical and thermal stability to the catalyst and desired dispersion of active atoms, governing the high productivity that may meet the industrial needs [51, 71]. In case of DRM, the reaction has to go through the adsorptive dissociation of methane, which is the rate-limiting step preferably occurring on the small metal surfaces. On the other side, carbon deposition favourably runs on larger ensembles than those needed for CH_4 reforming [51, 72]. This explains the crucial role of nickel dispersion. Therefore, the supports are required to offer additional properties firstly stated as strong metal-support interaction (MSI) that can maximize and stabilize mentioned dispersion of Ni atoms [71, 73]. That property is also good for high availability of metal–support interfaces, enhancing adsorption and dissociation of CO_2 which is beneficial for DRM and surface carbon gasification [51]. Then the surface acidity–basicity may play some role in the adsorption of CO_2 which produces surface species that can react with carbon to form CO [72, 74].

Among the metal oxides, alumina was commonly applied as support material of active species in DRM [2, 3, 66] due to its high availability, high specific surface area and low price [42]. According to the database in a recent review on catalytic dry reforming [66], over 24 different support materials were used in such reaction with the lead of γ-Al_2O_3, which was the choice in about 39% of the data points while other supports like ZrO_2, CeO_2, MgO, SiO_2 and TiO_2 were also used but in lower frequency. As a result, Ni/Al_2O_3 catalyst system is well studied and commonly considered as a benchmark in many DRM studies [51]. Generally, crystallographic forms, preparation procedure, and active species loading play important roles in Al_2O_3 supported catalyst performance. However, it is hard to obtain a Ni/Al_2O_3 catalyst that has high DRM activity but at low coking rate. For instance, in order to increase the resistance to coke formation of such catalyst, there were attempts to increase the metal dispersion by lowering the Ni loading or stabilize the active sites in defined structure such as $NiAl_2O_4$ spinel instead of bulk NiO species by applying higher calcination temperature [34]. However, such high-temperature pre-treatment suppresses catalytic activity, especially at low reaction temperatures (below 700 °C), because strong Ni-O bond in $NiAl_2O_4$ hinders the Ni^{2+} reduction to Ni^0 which is the active site for DRM. Besides, the catalyst basicity and stability of the catalyst is also important. This is a challenge for DRM application when pure Ni/Al_2O_3 mostly features a relatively moderate CO_2 adsorption which may not properly promote surface carbon gasification in DRM [51, 71]. The DRM performance of Ni/Al_2O_3 was also claimed to be unstable under severe conditions and the catalyst was rapidly deactivated [75]. Then, the support modification is needed to enhance the basicity and stability of the catalyst. Additionally, the conventional impregnation of Ni precursor onto Al_2O_3 may not be appropriate because it led to irregularly distributed and larger Ni particles [34]. That random deposition of Ni species is responsible for the agglomeration under the reduction and/or reaction conditions that causes the unavoidable high coking rate [51].

Magnesia is another material widely studied for supported Ni-based DRM catalysts [66]. MgO is an inexpensive support that has as well high thermal stability. By these benefits, MgO is suitable for practical utilization on the industrial scale [51]. Another advantage of using MgO for Ni-based DRM catalyst preparation relates to the possible formation of a NiO-MgO solid solution at any molar ratio due to the similarity of Mg^{2+} and Ni^{2+} anion radii as well as the crystal structures and lattice parameters of both oxides [34]. Indeed, Ni^{2+} (0.069 nm) is slightly smaller than that of Mg^{2+} (0.072 nm) [76] and the former can diffuse into MgO cubic lattice, creating mentioned mixed oxide structures with strong interactions between the two phases [72, 74]. As a result, NiO is well dispersed in such structure and can only be partially reduced, forming very small nickel crystallites on the surface of the mixed oxides. Therefore, Ni agglomeration and carbon deposition can be prevented. Besides, the relative high basicity of MgO as an alkaline-earth metal oxide enhances CO_2 adsorption on the basic support during DRM which contributes effectively to the suppression of carbon deposition via Boudouard reaction (Eq. 9) [34]. In a DRM study [77], several NiO-MgO catalysts were developed with different preparation methods that varied the dispersity of Ni in order to investigate the preference of carbon removal by CO_2. It was found in this study that rapid oxidation of carbon species on Ni surface by oxygen species stemming from CO_2 through dissociation at the metal-support interface, rather than on nickel metal surface, is a key step for the coking inhibition. By that, $Ni_{1-x}Mg_xO$ with solid solution could excellently adsorb and activate the CO_2 during DRM due to its higher surface basicity and also higher dispersity wherein the latter maximized the metal-support interfaces. Subsequently, these activated CO_2 species are dissociated, providing oxygen species migrating toward Ni atoms and reacting with different carbonaceous intermediates respective coke precursors such as adsorbed CH_x, surface or bulk Ni carbides, thereby establishing the resistance to carbon formation. However, the MgO-supported Ni catalyst may encounter problems of low activity due to poor reducibility, low specific surface area and the existence of lattice defects [51]. As a result, the support modification by partial substitution with other oxides with a proper preparation method and thermal treatment is needed.

Although most of the recent works in the DRM were performed over single oxide supports, there came also ideas of preparing and evaluating mixed material catalysts with benefits from these both two common oxide supports [66]. The beneficial effects of magnesia (enhancing chemisorption of CO_2 that accelerates the gasification of the deposited carbons and prevents the rapid deactivation) and alumina (enhancing thermal stability and specific surface area) can be incorporated in mixed MgO-Al_2O_3 support [34, 38, 57]. Indeed, MgO was previously reported to improve the catalytic performance of Ni/Al_2O_3 because it promoted the strong interaction between Ni and supports and increased the basicity of the mixed oxide support which both could suppress carbon formation in DRM [42, 78]. The specific surface area and total pore volume can also be tuned when both oxides are available compared to Ni/MgO or Ni/Al_2O_3 [79]. Cooperation of Mg and Al oxides in same support material can generate many compositions, such as most common $MgAl_2O_4$ spinel, which is a well-studied structure for Ni catalysts support in several types of reactions due to good chemical stability and mechanical strength [38, 45]. Other structures of MgO-Al_2O_3 mixed oxides could also be formed depending on different factors, e. g., preparation method and Mg/Al ratio, which were also studied as support for catalysts that can offer both good DRM performance and/or coking resistance [44, 47, 79, 80]. There are many structures other than $MgAl_2O_4$ observed in XRD analysis when $MgO/(MgO + Al_2O_3)$ ratio in the Ni catalysts varies between 0.06 to 0.94 but they were still not clearly identified [79]. Among these samples, $Ni/MgO-Al_2O_3$ with intermediate MgO amounts exhibited the highest activity but exposed higher deactivation rate compared to that of the samples with higher MgO contents due to lacking basicity and interaction between support and Ni species. Therefore, in order to simultaneously achieve beneficial targets in DRM, those factors influencing the $MgO-Al_2O_3$ material features have to be optimized in connection with other important parameters of the final catalyst, such as Ni loading and the probable necessity of modifiers/dopants [34].

2.2.3 Influence of modifiers

The addition of modifiers/dopants has an influence on catalyst surface nature and the interaction between the metal and the support [2]. These additives are used to regulate the catalyst acidity/basicity, metal atom electron density and dispersity, which are important factors governing catalyst activity and stability. Besides, adding the modifiers to DRM catalyst may adjust the adsorption, dissociation and activation of methane and carbon dioxide on the catalyst surface, and they can be chosen to improve the performance of the catalyst or enhance the carbon resistance. Alkali metal, alkaline earth metal oxides, as well as the rare earth metal oxides, are frequently used as modifiers for Ni-based catalysts applied for DRM [81]. Addition of these oxides has positive effects in common such as neutralizing the surface acidity of the catalyst, subsequently reducing the rate of methane cracking and dehydrogenation into solid carbon. Also the adsorption of CO_2 on the catalyst surface can be increased due to the enhancement of basic sites. Inversely, rare earth metal oxides such as La_2O_3 and CeO_2 additionally enhance the CO_2 dissociative adsorption that enriches adsorbed oxygen which can be supplied to the oxidation of CH_x species as a slow step in the DRM reaction [51]. By that, the formation of carbonaceous deposits from the over-cracking of CH_4 can be controlled.

La_2O_3 is a good choice among those rare earth metal oxides that improves the reducibility of low Ni content catalysts [82] and promotes the CO_2 activation rate and surface carbon oxidation [83]. These effects accelerate the overall reaction rate and reduce the deactivation caused by rapid coking [2, 50], especially when harsh DRM conditions are applied. For instance, the addition of La^{3+} to Ni/Al_2O_3 catalyst resulted in the formation of $LaAlO_3-Al_2O_3$ and inverse $NiAl_2O_4$ spinel structures that were found to stabilize the catalyst activity over 30 h [84]. La^{3+} was also reported to lead to higher activity of Ni-hydrotalcite-derived catalysts at low temperatures [83].

The presence of rare earth metals (RE_2O_3) in the catalyst could lead to a strong interaction between CO_2 and RE_2O_3 in DRM that accelerates the formation of surface $RE_2O_2CO_3$ species (Eq. 11). There were studies proposing the overall mechanism of DRM on La [85] or Gd [86] containing catalysts which can be illustrated by the following equations:

$$CO_2 + RE_2O_3 \rightarrow RE_2O_2CO_3 \quad \text{(Eq. 11)}$$

$$CH_4 + (5\text{-}x)^* \rightarrow CH_x^* + (4\text{-}x)\ H^* \quad \text{(Eq. 12)}$$

$$RE_2O_2CO_3 + CH_x^* \rightarrow 2CO^* + RE_2O_3 + x/2\ H_2 \quad \text{(Eq. 13)}$$

$$RE_2O_2CO_3 + C \rightarrow 2CO + RE_2O_3 \quad \text{(Eq. 14)}$$

In the suggested reaction pathways, the surface $RE_2O_2CO_3$ species rapidly react with CH_x species generated by CH_4 dissociation (Eq. 13). In this mechanism, the activation of CO_2 was significantly enhanced via formation of $RE_2O_2CO_3$ that in turn further improved the decomposition of CH_4. Therefore, the interfacial area between Ni and oxy-carbonate particles should be the most active sites of the catalyst.

The Ni catalysts can be modified not only by those inorganic oxides but also by organic additives in the stage of Ni catalyst preparation that will be subsequently removed by thermal treatment. Chelating agents are molecules with two or more electron-pair donor atoms which can perform as a ligand attaching to metal ions to form metal complexes [87]. These complexes were then applied to modify the impregnation method. As a result, uniform distributions and high dispersions of the active component over the support were achieved. Such beneficial properties are attributed to the diffusion-controlled even distribution of metal atoms in the precursor structures as well as to the enhanced viscosity of the gel-like material, inhibiting redistribution of the deposited metal species during the subsequent drying step. There were made many efforts in using such complexing agents in catalyst preparation protocols applied for different reactions, such as HDS [55, 88] and CO methanation [89], that led to Ni dispersion improvement. The complexing agent can vary in type, such as ethylenediamine [54], citric acid [90], cyclodextrin [91], arginine [92], that were used for Ni impregnation. In DRM, there have been several studies focusing on Ni/SiO_2 catalysts that applied such complexation-impregnation method to overcome the obstacle of insufficient Ni dispersion [93-95].

2.2.4 Influence of content and metal particle size

Active metal loading is one of the important factors (apart from support type, promoter availability, preparation method and thermal pre-treatment) affecting the metal particle size of the catalyst which plays a key role to suppress of carbon deposition and attain higher catalytic activity and stability [39]. The Ni catalysts applied for DRM were reported to have Ni contents varying from 1 wt% to above 50 wt% [34]. Generally, the increase of metal particle size leads to more serious coking and significant decline in catalytic activity due to loss of active surface [17, 96]. An investigation on catalytic performance and coking in DRM was implemented on Ni-mesoporous alumina with different Ni loadings (7, 10 and 15 wt%), showing the rise of catalytic activity when the Ni content increased from 7 to 15 wt% [97]. However, higher loading of Ni led to the problem of bigger metal particles (>15 nm) due to the low surface area that lowered the conversions of the reactants. Besides, it also was found that the smaller particles (<15 nm) generated the active amorphous carbon species that could be easily removed by the reversed Boudouard reaction. In contrast, larger metal particles created less reactive carbon (as seen in the case of 15 wt% Ni catalyst), mostly initiated by the high-rate methane decomposition, causing the catalyst deactivation.

The increasing carbon formation rate from MD reaction on large metal particles can be explained by a mechanism [51] (and references therein) suggesting that each CH_x species formed from dissociated CH_4 is preferentially located at a site which thereby completed its tetravalency. By that, CH_3 can adsorb on top of a single metal atom, CH_2 presents bridged adsorption on two closed atoms, while CH and C require the associated occupation of higher coordination sites. The two latter species, especially C, would be adsorbed on hollow sites with many nearest neighbouring sites, which occur when big particles/clusters of Ni are created.

The decrease in surface area and catalytic activity by increasing the Ni content from 3.5 to 18.4 wt% was also observed in a study with mesoporous $Ni{-}CaO{-}ZrO_2$ nanocomposite [98]. The highest catalytic activity was attributed to the higher metal dispersion while the smaller particle size prevented carbon deposition.

There were several studies of MgO supported DRM catalysts indicating that the loading of Ni species also regulates metal particle size and thus catalyst performance, independent whether Ni is deposited on MgO [48] or diffused in NiO-MgO solid solution structures [99, 100]. It was found in these publications that Ni content in the range of 5–15 wt% was effective for DRM, whereas at higher Ni contents, the metal particles became large and behaved like the bulk materials, bringing about a negative effect on the anti-coking performance in DRM and thus limiting the catalyst stability. On the other hand, the catalysts with the very low nickel loading (< 2 wt%) encountered low specific activity due to an insufficient amount of active species.

There were very few studies focusing on catalysts with Ni contents in the range of 1-3 wt% (Table 2.1), but collecting the results regarding Ni catalyst systems with high performance and/or stability. Generally, in order to achieve better stability or higher H_2 and CO productivity at high space velocity, higher Ni loadings had to be applied. Exceptionally, the Ni/ZrCe-Al_2O_3 catalyst system with low Ni content (2 wt%) maintained 80% of the original activity after 72 hours on stream at high space velocity [101]. However, the low feed concentration of CH_4 and CO_2 due to dilution by N_2 may have pushed such apparently superior performance.

Table 2.1. Literature results on Ni-based catalysts regarding the performance and/or stability in DRM; (*) A: diluting gases (He, Ar, N_2); (**) thousand h^{-1}, n. a.: no applied data

Nickel Catalyst	**wt%**	**GHSV $L/(g_{cat}\cdot h)$**	**Reactant CH_4:CO_2:A^***	**t (h)**	**T (º C)**	**$X\%_{CH4}$**	**$X\%_{CO2}$**	**Ref**
Ni/MCM-41	1.2	50	1:1:2	30	750	70	n. a.	[102]
Ni/ZrCe-Al_2O_3	2	130	1:1:7	72	700	95	n. a.	[101]
Ni-Zr/MCM-41	2	50	1:1:2	72	750	91	n. a.	[65]
Ni/$Ce_{0.75}Zr_{0.25}O_2$	2.1	13.2	5:5:1	9	850	92	95	[103]
Ni/Al_2O_3	3.8	42	1:1:5	25	650	57	63	[104]
Ni-MgO/ZnO	4.8	40	1:1:12	100	800	99	99	[105]
Ni/Mo/SBA15-La_2O_3	5	12	1:1	120	800	84	96	[106]
Ni/$MgAl_2O_4$	5	90	1:1	60	750	85	96	[45]
Ni-Mo/SBA15	5	12	1:1	100	800	79	96	[107]
Ni/Al_2O_3	5	48	1:1:2	50	800	80	85	[108]
Ni/B_2O_3-Al_2O_3	5	60	1:1	65	700	72.5	69	[109]
Ni-K-Ca/ZSM-5	5	60^{**}	1:1:2.2	140	800	n. a.	90	[110]
Ni-K/MgO-ZrO_2	8	150	1:1:8	14	750	90	91	[111]
Ni/MgO-Al_2O_3	8	60	1:1	100	750	87	89	[75]
Ni/CeO_2-Al_2O_3	9.4	90	4:4:2	25	800	76	86	[112]
Ni/Mg-ZrO_2	10	240	1:1:2	5	600	25	25	[113]
Ni/CeO_2-Al_2O_3	10	20	1:1	250	800	80	90	[114]
Ni/Al_2O_3	10	90	1:1:1	48	800	94	93	[115]
Ni-Ce/SiO_2	10	12	1:1	100	800	85	91	[116]
Ni/SBA15	12.5	12^{**}	1:1	720	800	90	90	[117]
Ni/MgO-Al_2O_3	12.6	30	1:1:1	150	800	92	95	[118]
Ni–$Ce_{0.8}Zr_{0.2}O_2$	15	216	0.98:1.02:1	100	800	92	93	[119]
Ni-MgO-$Ce_{0.8}Zr_{0.2}O_2$	15	480^{**}	1:1:3	200	800	95	96	[120]

Ni/MgO	15.7	60	1:1	150	790	91	97	[121]
$Ni_{0.15}Mg_{0.02}Al_{0.83}O_x$	16.2	15	1:1	100	700	95	96	[122]
$Co_{0.075}Ni_{7.425}Mg_{92.5}O$	16.4	60	1:1	1000	800	81	n. a.	[123]
NiO/MgO	16.4	20.4	25:25:18	100	760	70	83	[124]
Ni−yolk/Ni/SiO_2	18.6	36	1:1:1	90	800	90	95	[125]
$Ni_{0.36}Mg_{0.32}Al_{0.32}O_x$	38	300	10:10:80	8	750	68	90	[126]

3 Experimental section

3.1 Catalyst preparation

In this thesis, low content Ni catalysts were prepared using various types of Mg-Al supports and modified with rare earth metals (RE^{3+}, RE: La, Sc, Gd) and CA-based synthesis. The impregnation (imp.) was the main preparation method. All the catalysts were denoted in Table 3.1 with their parameters varied. These prepared samples can be briefly described as below:

In chapter 4, the pre-treatment and material composition of Mg-Al supports were studied and selected in terms of their corresponding Ni catalyst activity in DRM. Firstly, a Mg-Al mixed-oxide solid with 50 wt% of MgO, obtained by calcining the commercial hydrotalcite at 550 °C in 3 hours, was chosen as the default support due to its published properties [127]. This sample was denoted as $Mg_{1.3}AlO_x$ because of its Mg/Al molar ratio, according to ICP. Then thermal pre-treatments were applied on this material with different temperatures (T = 700 °C, 800 °C, 1000 °C), producing various Mg-Al bare supports denoted as $Mg_{1.3}AlO_x$.T. Then the Ni catalysts were from these supports and finally calcined at 800 °C. Consequently, since Ni/$Mg_{1.3}AlO_x$ with no support pre-treatment was included in the next study of the influence of MgO-Al_2O_3 composition, a series of Mg-Al mixed-oxides with other Mg/Al ratios (0.5, 1.3 or 3.0) were prepared, denoted as Mg_aAlO_x, and applied to Ni catalyst preparation.

In chapter 5, Ni/$Mg_{1.3}AlO_x$ was chosen to study the catalyst modification and activity stabilization. In this investigation, La^{3+} (denoted as La) and/or CA-based synthesis (denoted as (CA)) were applied to modify Ni/$Mg_{1.3}AlO_x$.

In chapter 6, the $Mg_{1.3}AlO_x$.1000 supported Ni catalyst studied in chapter 4 was also applied in order to investigate the catalytic performance and coking resistance in comparison with $Mg_{1.3}AlO_x$, also in CH_4-rich DRM.

In chapter 7, Gd^{3+} (denoted as Gd) and Sc^{3+} (denoted as Sc) modified Ni catalysts were developed for CH_4-rich DRM but still being applicable in stoichiometric DRM.

Several materials applied as the references (Ref.) mainly for characterization can also be found in Table 3.1.

Table 3.1. List of supports, Ni catalysts, and reference samples used in this thesis

Samples	MgO content in support (wt%)	Calcination temperature (°C)	Modification	Chapter
$Mg_{1.3}AlO_x$	50	550		4,5,6,7
$Mg_{1.3}AlO_x$.700	50	700		4
$Mg_{1.3}AlO_x$.800	50	800		4
$Mg_{1.3}AlO_x$.1000	50	1000		4,6,7
Al_2O_3	0	550		4
$Mg_{0.5}AlO_x$	30	550		4
Mg_3AlO_x	70	550		4
MgO	100	550		4
Ni/$Mg_{1.3}AlO_x$	50	800		4;5;6;7
Ni/$Mg_{1.3}AlO_x$.700	50	800		4
Ni/$Mg_{1.3}AlO_x$.800	50	800		4
Ni/$Mg_{1.3}AlO_x$.1000	50	800		4;6
Ni/Al_2O_3	0	800		4
Ni/$Mg_{0.5}AlO_x$	30	800		4
Ni/Mg_3AlO_x	70	800		4
Ni/MgO	100	800		4
Ni(CA)/$Mg_{1.3}AlO_x$	50	800	CA-assisted imp.	5;6
La.Ni/$Mg_{1.3}AlO_x$	50	800	La^{3+}	5;6
La.Ni(CA)/$Mg_{1.3}AlO_x$	50	800	La^{3+}, CA-assisted imp.	5;6
La.Ni(CA)/Al_2O_3	0	800	La^{3+}, CA-assisted imp.	5
La.Ni(CA)/$Mg_{1.3}AlO_x$.1000	50	800	La^{3+}, CA-assisted imp.	6;7
Sc.Ni/$Mg_{1.3}AlO_x$	50	800	Sc^{3+}	7
Gd.Ni/$Mg_{1.3}AlO_x$	50	800	Gd^{3+}	7
$MgAl_2O_4$	30	1000		Ref.
NiO	N/A	800		Ref.
$LaNiO_3$	N/A	800		Ref.
La.Ni/MgO	100	800	La^{3+}	Ref.
La.Ni(CA)/MgO	100	800	La^{3+}, CA-assisted imp.	Ref.

3.1.1 Synthesis of Ni catalysts with different Mg-Al supports

Mg-Al mixed oxide supports were prepared from Mg-Al hydrotalcite (Pural MG, Sasol). The default mixed oxide $Mg_{1.3}AlO_x$ was obtained by calcining the corresponding Mg-Al hydrotalcite (MG50) at 550 °C. From this material, the first series of the bare supports was collected from the thermal pre-treatments at different temperatures for 6 h in air.

The most suitable thermal pre-treatment procedure in terms of final catalyst activity was then applied to the investigation focusing on the impact of Mg/Al molar ratio. As the activity test results showed that no further pre-treatment was needed because $Ni/Mg_{1.3}AlO_x$ exposed the best efficiency in stoichiometric DRM, the study moved on with other support candidates: $Mg_{0.5}AlO_x$ (from MG30) and Mg_3AlO_x (from MG70) collected via the same procedure as for $Mg_{1.3}AlO_x$. These support candidates were then also used for Ni catalyst preparation to study the impact of Mg/Al ratio on the catalytic performance.

In order to prepare the catalysts for DRM, these Mg-Al mixed oxide supports were treated with metal precursors in the wet impregnation step. $Ni(NO_3)_2 \cdot 6H_2O$ (Alfa Aesar) was used as the precursor for Ni. The calculated amount of Ni precursor was dissolved in deionized water and the solution was stirred for 4 h. The Mg-Al supports were then put into the solution and the slurry was kept stirring at 60 °C for 15 h. Water was removed by a rotary evaporator and the samples were dried overnight and calcined at 400 °C for 3 h and then at 800 °C for 6 h both in air. The nominal content of Ni in all supported Ni-containing catalyst was 2.5 wt%. Other materials were used as reference. They are MgO (FLUKA) and Al_2O_3 (boehmite calcined at 550 °C, Pural SB, Sasol) as well as their corresponding 2.5 wt% Ni samples (Ni/MgO and Ni/Al_2O_3). Pure NiO was prepared by calcining $Ni(NO_3)_2 \cdot 6H_2O$ (Alfa Aesar) at 800 °C. The study on the samples mentioned in this section will be described in chapter 4.

3.1.2 Synthesis of Ni catalysts pre-treated with La^{3+} and/or citric acid

Mg-Al mixed oxide supported Ni catalysts studied in chapter 5 were prepared by wet (co-)impregnation of $Mg_{1.3}AlO_x$ with an procedure identical to that described in section 3.1.1. Prior to impregnation, the hydrotalcite (MG50) was calcined at 550 °C in air to obtain the bare support $Mg_{1.3}AlO_x$. $Ni(NO_3)_2 \cdot 6H_2O$ and $La(NO_3)_3 \cdot 6H_2O$ (99%, ABCR GmbH) were used as metal precursors for Ni^{2+} and La^{3+}, respectively. Citric acid (> 99%, Alfa Aesar) was added simultaneously (denoted as CA) to such metal precursor solution in some cases. The nominal content of Ni in all supported Ni-containing catalysts was 2.5 wt%. The molar ratio of La and Ni was set to 0.8, and the CA/metal molar ratio was always fixed at 1.5. Other materials were used as references: MgO and the corresponding 2.5 wt% Ni samples (Ni/MgO, La.Ni/MgO) were similarly prepared to Mg-Al supported catalysts. Bare $Mg_{1.3}AlO_x$.800, studied in chapter 4, was also used as reference sample in XRD and TPR. $LaNiO_3$ was prepared by citrate sol-gel method [128] from the same metal precursors in the presence of CA (CA/metal molar ratio = 1.5). The material was then calcined at 800 °C. La.Ni(CA)/Al_2O_3 with same La and Ni concentrations and CA-assisted synthesis as used for La.Ni(CA)/$Mg_{1.3}AlO_x$ was also prepared to study the effectivity of MgO in catalyst stabilization.

3.1.3 Synthesis of Ni catalysts for CH_4-rich DRM

Mg-Al mixed oxide supported Ni catalysts were also prepared by wet (co-) impregnation of calcined Mg-Al hydrotalcite (Mg/Al ratio ~ 1.3). Prior to impregnation, the hydrotalcite precursor (MG50) was calcined at 550 °C to obtain $Mg_{1.3}AlO_x$. Besides, in order to generate $Mg_{1.3}AlO_x$.1000, $Mg_{1.3}AlO_x$ was pre-treated at 1000 °C for 6 h in air. Subsequently, the (co-)impregnation procedures for $Ni(NO_3)_2 \cdot 6H_2O$, $La(NO_3)_3 \cdot 6H_2O$ and/or CA onto these supports were carried out similarly to that described in section 3.1.1. The nominal content of Ni in all supported Ni-containing catalysts was kept at 2.5 wt%. The molar ratio of La and Ni was also set to 0.8, and the CA/metal ratio was fixed at 1.5. The study on the samples mentioned in this section will be described in chapter 6.

3.1.4 Synthesis of Ni catalysts modified with other rare earth elements

Modified Ni catalysts studied in chapter 7 were also prepared by wet (co-) impregnation of $Mg_{1.3}AlO_x$. Prior to impregnation, $Mg_{1.3}AlO_x$ was generated as described in 3.1.2 from corresponding hydrotalcite precursor (MG50). Subsequently, the solutions containing dissolved metal precursors for Ni^{2+}, La^{3+}, Gd^{3+} or Sc^{3+} were prepared. While same $Ni(NO_3)_2 \cdot 6H_2O$, $La(NO_3)_3 \cdot 6H_2O$ metal precursors as before were used for Ni^{2+}, La^{3+} sources, the solution of Gd^{3+} or Sc^{3+} were prepared by following steps: Gd and Sc (metal state, > 99%, smart-elements GmbH) were dissolved in HNO_3 solution (Fisher Scientific) forming the 5% Gd^{3+} or Sc^{3+} solutions. Then the (co-)impregnation procedure similar to that described in section 3.1.1 was implemented. The nominal content of Ni in all supported Ni-containing catalysts was kept at 2.5 wt%. The molar ratio of RE^{3+} and Ni were also set to 0.8.

3.2 DRM activity test

DRM was carried out in a fixed-bed continuous-flow quartz reactor (ambient pressure, GHSV = 85-170 L/(g_{cat}×h); 500–800 °C). All volumetric flow rates given in this study are related to 25 °C and 1 bar. For every experiment, 50 mg of catalyst with the grain size below 315 μm was diluted by 2 g of inert quartz and introduced to the reactor. After in situ pre-reduction with pure H_2 (700 °C, 100% H_2, 50 mL/min) for 1 h (used in all activity experiments in chapter 4 as well as in long-term tests with CH_4:CO_2 = 1 in chapter 5 and 7) or 1.5 h, the temperature was adjusted and maintained for whole time on stream (TOS) from 8 to 160 hours. The feed gas was composed of 80 vol% CH_4 in He (Air Liquide) and admixed pure CO_2 (Linde) with CH_4/CO_2 = 1 or 2. He served as internal standard for volume change estimation in the reaction. The gas compositions were then analysed by an on-line gas chromatograph (Agilent 6890) equipped with flame ionization detector (HP Plot Q capillary, 15 m × 0.53 mm × 40 μm) and thermal conductivity detector (Carboxene packed, 4.572 m × 3.175 mm) for analysis of hydrocarbons and permanent gases, respectively. Pure components were used as the references for peak identification and calibration. Carbon balances were calculated from gas products reaching more than 97% in this work. Conversions (X) and H_2/CO ratio were calculated using the formulas given below:

$$X_{CH_4}\,(\%) = \frac{\text{moles of converted } CH_4}{\text{moles of } CH_4 \text{ in feed}} \times 100\% \qquad \text{(Eq. 15)}$$

$$X_{CO_2}\,(\%) = \frac{\text{moles of } CO_2 \text{ converted}}{\text{moles of } CO_2 \text{ in feed}} \times 100\% \qquad \text{(Eq. 16)}$$

$$H_2/CO \text{ ratio} = \frac{\text{moles of } H_2 \text{ produced}}{\text{moles of CO produced}} \qquad \text{(Eq. 17)}$$

$$H_2 \text{ productivity} = \frac{\text{Flowrate of output } H_2}{\text{mass of catalyst}} \qquad \text{(Eq. 18)}$$

3.3 Catalyst characterization techniques

Catalyst characterization is essentially concerned in any practical catalytic research and industrial activities as it provides important parameters including composition, surface texture, crystalline phases, morphology, reducibility, and metal coordination of the catalysts which are connected with catalytic performance.

In this section, the major principles and experimental details of physicochemical methods employed to characterize the catalysts in this thesis are described.

3.3.1 X-ray diffraction (XRD)

X-ray powder diffraction is a non-destructive technique commonly used to study the atomic structure of crystalline matter [129]. Since the wavelengths of X-ray radiation are in the order of magnitude of atomic distances, X-ray diffraction is an important characterization technique to provide the structural information of a crystalline material [130]. Generally, this diffraction method applies the interference of the radiations scattered by the atoms in the ordered structures [129].

In XRD, the Bragg's law is the fundamental theory describing the relationship of lattice spacing (or interplanar distance) with the angles 2θ between the incident X-ray and the scattered waves generated as the result of the interaction between the radiations and the atoms from a crystalline material [130]. In that law, the conditions for constructive interference (in phase) of the scattered waves at angle θ are given (Eq. 19) where n is an integer, d is the interplanar distance of crystal and λ is the wavelength of the incident X-ray beam.

$$\mathrm{n}\cdot\lambda = 2\mathrm{d}\cdot\sin\theta \qquad \text{(Eq. 19)}$$

According to the equation, when the sample position and the X-rays wavelength are fixed, constructive interference is dependent on the incident angle theta. This interference will occur if the difference between path lengths of the waves from two different parallel lattice planes (2dsinθ) is an integer multiple of the wavelength, resulting in the reflection peaks collected in XRD detectors. At other incident angles, subtractive or destructive interferences (out phase) among the scattered waves occur [131].

As the results, the analysis of the position and intensity of these reelection peaks in the diffraction pattern offers the results to identify the sample crystalline phases as well as quantify their composition.

Experimental description: XRD powder patterns were recorded on a Panalytical X'Pert diffractometer equipped with a Xcelerator detector using automatic divergence slits and Cu Kα1/α2 radiation (40 kV, 40 mA; λ= 0.015406 nm, 0.0154443 nm). Cu beta-radiation was excluded using a nickel filter foil. The samples were mounted on silicon zero background holders. The obtained intensities were converted from automatic to fixed divergence slits (0.25°) for further analysis. Peak positions and profile were fitted with Pseudo-Voigt function using the HighScore Plus software package (Panalytical). Phase identification was done by using the PDF-2 database of the International Center of Diffraction Data (ICDD).

3.3.2 Low-temperature N_2 adsorption

The textural properties of the catalyst (specific surface area, pore volume and pore size distribution) are essential to be measured. These properties of the solid catalysts can be determined by conducting the physical adsorption experiment and applying Brunauer-Emmett-Teller (BET) theory [131, 132]. Nitrogen is commonly used as an adsorbate molecule. The adsorption force in this measurement method is van der Waals force which is a weak interaction between the solid surface and the adsorbent. The measurement is usually carried out at the boiling temperature of liquid nitrogen (-196 °C). Based on the Langmuir theory of monolayer physisorption, the BET theory is extended to multilayer adsorption. Thus, additional layers can be adsorbed on top of the monolayer with heats of adsorption equivalent to heat of liquefaction or heat of vaporisation.

The resulting BET adsorption isotherm equation is

$$\frac{p}{v \cdot (p_0 - p)} = \frac{(C-1)}{v_m \cdot C} \frac{p}{p_0} + \frac{1}{v_m \cdot C} \qquad \text{(Eq. 20)}$$

where v is the volume of gas adsorbed at the relative pressure p/p_0, and v_m is the volume adsorbed at the monolayer, p is the measured pressure of the gas, p_0 is the saturation pressure of the gas at the temperature of adsorption, and the parameter C is exponentially related to the energy of monolayer adsorption [133].

The range of linearity of the BET is always lying between relative pressures (p/p_0) of 0.05 and 0.35. As a result, from the linear (Eq. 20), the values of v_m and C can be determined. Subsequently, the specific surface area (S_{BET}) can be calculated by

$$S_{BET} = \frac{v_m \cdot N \cdot s}{V \cdot m} \qquad \text{(Eq. 21)}$$

in which s is the cross-sectional area of the adsorbate molecule, m is the mass of adsorbent, V the molar volume of the adsorbate gas, and N is the Avogadro constant = $6.023 \cdot 10^{23}$.

Barrett-Joyner-Halenda (BJH) is a method for calculating pore size distribution from experimental isotherms using the Kelvin model of pore filling as follow [134]

$$r_K = \frac{-2\sigma \cdot v_1}{RT \cdot \ln(p/p_0)} \qquad \text{(Eq. 22)}$$

where r_K is the Kelvin radius, v_1 is the molar volume of the liquid condensate, and σ is the surface tension of the liquid condensate. The pore radius of cylindrical pores is given by Kelvin radius and the film thickness of adsorbed multilayer t as given by

$$r_p = r_K + t \qquad \text{(Eq. 23)}$$

in which r_p is pore radius and t is the statistical thickness of adsorbed film which can be derived from standard isotherms.

The BJH method is valid only to the mesopore and small macropore size range. The pore size distribution is usually calculated from the desorption branch of the isotherm.

Experimental description: Nitrogen physisorption method served for calculating the specific surface area and pore volume distribution according to the BET theory, while for pore size distribution BJH method was used for the calculation. The low-temperature N_2 adsorption measurements were performed on a Micromeritics ASAP 2010 apparatus at -196 °C. The samples were degassed at 200 °C in vacuum for 4 h before the analysis.

3.3.3 Inductively-coupled plasma optical emission spectrometry (ICP-OES)

The elemental composition of prepared catalysts is essential to evaluate the accuracy of the experiments and to subsequently conduct the comparative studies regarding other characterisation techniques (e.g. TPR, XPS) or the catalytic performance. The weight percentages of metal elements can be quantified by ICP-OES. This method is a type of emission spectroscopy that uses the inductively coupled plasma to excite atoms and ions that causes electromagnetic radiation emission at the wavelengths which are characteristic for particular elements. The atomic emission emitting from the plasma is displayed in either a radial or axial configuration, collected with a lens or mirror, and then imaged onto the entrance slit of a wavelength selection device.

Experimental description: The metal (Ni, Mg, Al, La, Sc, Gd) contents of the samples were determined by ICP-OES using a 715-ES device (Varian Inc.).

3.3.4 Carbon deposition analysis

Rapid coking deposition is a common issue in DRM. In order to evaluate the stability of the Ni catalysts against this problem, the content of carbon accumulated on the corresponding spent catalysts after DRM tests were determined.

Experimental description: The carbon deposition on spent catalysts was analysed using a TruSpec Micro CHNS analyser (LECO Corporation). Up to 10 mg of the investigated sample are catalytically burned with oxygen in the helium stream at 1100 °C. The resulting gas was analysed with an infrared detector and a thermal conductivity detector.

3.3.5 Temperature-programmed reduction by H_2 (H_2-TPR)

The reducibility of Ni catalysts plays an important role, specifically in the pre-treatment step in which the catalyst is reduced to obtain the metal state of Ni which represents the active sites in DRM. The reducibility of the catalysts can be determined using H_2-TPR method [135]. In the TPR measurement, the Ni catalysts were subjected to a programmed temperature rise, as the reductant gas mixture (H_2 diluted in inert gas) was passed over the sample. Thermal conductivity detector (TCD) is typically used for the effluent gas analysing. This detector measures the changes in the thermal conductivity of the gaseous stream. Based on H_2-TPR profiles, information on the number of the redox species present in the catalyst as well as the reduction temperature of these active species can be obtained.

Experimental description: The H_2-TPR experiments were performed with a Micromeritics Autochem II 2920 instrument. A 300 mg sample was loaded into a U-shaped quartz reactor and heated from room temperature (RT) to 400 °C with 20 K/min in 5%O_2/He (50 mL/min) for 30 min at 400 °C, then cooled to RT while flushing with Ar. The TPR run was carried out from RT to 1000 °C in a 5%H_2/Ar flow (50 ml/min) with a heating rate of 10 K/min and then held at final temperature for 30 min before cooled to room temperature. The H_2 consumption peaks, indicating the reduction, were recorded using a thermal conductivity detector. The amount of H_2 consumed was calculated based on the peak areas.

3.3.6 X-ray photoelectron spectroscopy (XPS)

X-ray photoelectron spectroscopy (XPS) is used to determine the oxidation state of Ni species as the active sites for DRM on the catalyst surface as well as their chemical interaction with surrounding Mg-Al mixed oxide supports [136]. XPS is based on the photoelectric effect arising when high energy photons (usually in the keV range) hit a surface of the materials with the consequent emission of electrons (photoelectrons) [137]. These photoelectrons leaving the (solid) sample are then characterized in order to estimate their kinetic energy (E_K) values which are essential to calculate the corresponding binding energies (BE). This BE depends on the element of its origin. Generally, almost all elements of the periodic table can be detected by different characteristic BE peak positions, except Hydrogen [136]. The surface sensitivity of the XPS technique is determined by the relatively low escape depth (0.5 – 3 nm) of the only elastically scattered electrons. In the XPS experiments, Al $K\alpha$ (1486.6 eV) X-ray sources are often used. With the help of an electron spectrometer, the kinetic energy of the emitted photo electrons is measured. Taking the known energy of the incident X-ray radiation used for excitation ($h \cdot v$), the binding energy can be calculated by the following equation based on the work of Einstein and Rutherford [136]:

$$\mathrm{BE} = \mathrm{h}\cdot\nu - \mathrm{E_k} - \phi \qquad \text{(Eq. 24)}$$

where ϕ is the work function depending on both the spectrometer and the material.

For one element, BE depends on valence charge or oxidation state of the investigated atoms and effective potential of the surrounding atoms [136]. It is known that the decrease in oxidation state leads to higher BE values. However, the impact of surrounding atoms is more complicated but can be simply estimated by considerations of electronegativity differences of these atoms.

Experimental description: XPS measurements were carried out with a VG ESCALAB 220iXL instrument (Thermo Fisher Scientific) with monochromatic AlKα radiation (E = 1486.6 eV). Samples are prepared on a stainless steel holder with conductive double sided adhesive carbon tape. The electron binding energies were obtained with charge compensation using a flood electron source and referenced to the C1s peak of C-C and C-H bonds at 284.8 eV. For quantitative analysis the peaks were deconvoluted with Gaussian-Lorentzian curves, the peak areas were divided by the transmission function of the spectrometer and a sensitivity factor obtained from the element specific Scofield factor.

3.3.7 UV-Vis diffuse reflectance spectroscopy (UV-Vis-DRS)

UV-Vis spectroscopy is useful to study coordination geometries, aggregation or oxidation states of transition metal ions [138]. This characterization technology is suitable for the analysis of Ni species because the intense charge-transfer in octahedral NiO lattice can be observed [139] and the major coordination forms of Ni^{2+} species can be differentiated [140]. Besides, because Ni is the only element that is sensitive to UV-Vis-DRS in all prepared and studied catalysts, the information of Ni^{2+} species are individually revealed.

The application of UV-Vis spectroscopy is related to the excitation and transitions of electrons which are observed when the lights with wavelengths in the UV or visible region (200 – 400 nm or 400 -800 nm, respectively) scatter by the catalyst particles. There are several types of electronic transitions that may be involved in UV-Vis-DRS of inorganic catalytic materials:

- Ligand to metal (LMCT) and metal to ligand (MLCT) charge transfers.

- Metal to metal charge transfers or d → d transitions.

In the diffuse reflection mode of UV-Vis spectroscopy used for catalyst particles, the light is supposed to be irradiated from all directions without transmission by the solid samples. The reflected radiation from a powdered surface involves two components: specular reflection without any interaction with the sample and diffuse reflection which penetrates the sample and is reflected after multiple scattering at sample particles by which electron transitions are excited.

The reflectance is given by $R_\infty = I/I_0$, where I and I_0 are the intensities of the incident and reflected light, respectively. Since reflectance of the sample is compared to that of the standard compound, the relative quantity $R'_\infty = R_\infty(\text{sample})/R_\infty(\text{standard})$ is used. This reflectance is related to both the absorption coefficient (K) and the scattering coefficient (S) in the Kubelka-Munk $F(R'_\infty)$ function as follow [138]:

$$F(R'_\infty) = \frac{(1 - R'_\infty)^2}{2R'_\infty} = \frac{K}{S} \qquad \text{(Eq. 25)}$$

Experimental description: UV-Vis-DR spectra were measured over the wavelength range of 200-800 nm using a Cary 5000 spectrometer (Varian) equipped with a diffuse reflectance accessory (praying mantis, Harrick). $BaSO_4$ was used as a white reference standard and diluted material was used for the measurement with pure NiO because of its high Ni content.

3.3.8 Scanning transmission electron microscopy (STEM)

STEM is a precious tool for the characterization of nanostructures, offering a range of different imaging modes with information of elemental composition and material morphology at the high sensitivity of atom level [141]. In STEM, a highly focused electron probe is scanned across the specimen and several types of scattering from transmitted electrons are collected as a function of the position [131]. Using an aberration corrector in the condenser system, atomic resolution can be achieved. Multiple detectors can be simultaneously operated to gather these electrons for the maximum complementary information [141]. Generally, the bright field detectors include the unscattered beam, the voids of the material then appear bright. In contrast, dark field detectors exclude these unscattered electrons and the holes appear dark.

In bright-field STEM, the angle-adjustable annular detectors collecting the electrons around a direct beam disk are employed to observe the light and heavy atoms in a single STEM image [142]. However, these detectors are preferably applied to give the atomic resolution STEM images of various light elements, such as hydrogen [143], carbon [144] and oxygen [145]. Nevertheless, it is difficult to interpret bright field images as several contrast mechanisms need to be differentiated [142].

High-angle annular dark-field imaging (HAADF) with high accuracy of atomic positions uses incoherently scattered electrons (Rutherford scattering) with a large scattering angle [146]. This technique is highly sensitive to identify atomic species because the intensity per atom depends on the atomic number or Z-contrast [147]. For elements with the higher Z values, more electrons can be scattered at higher angles due to greater electrostatic interactions between the nucleus and emitted electrons [148]. As a result, the HAADF detectors may collect the higher signal proportionally to such values of the atoms, leading their positions appearing brighter in the resulting images. However, usage of this method without bright-field STEM may encounter the lack of light element information because of their invisibility [142].

Besides, the X-rays generated by the samples and collected via an electron dispersive X-ray spectroscopy detector provide accurate elemental analysis with high spatial resolution, generating elemental maps with high resolution [131].

Experimental description: STEM measurements were performed at 200 kV with an aberration-corrected JEM-ARM200F (JEOL, Corrector: CEOS). The microscope is equipped with a JED-2300 (JEOL) energy-dispersive X-ray-spectrometer (EDXS) for chemical analysis. The aberration-corrected STEM imaging (High-Angle Annular Dark Field (HAADF) and Annular Bright Field (ABF)) was performed under the following conditions: HAADF and ABF both were done with a spot size of approximately 0.13 nm, a convergence angle of 30-36° and collecting at semi-angles for HAADF and ABF of 90-170 mrad and 11-22 mrad, respectively. The sample was deposited without any pre-treatment on a holey carbon supported Cu-grid (300 mesh) and transferred to the microscope.

4 Development of low nickel content catalysts for dry reforming of methane

As mentioned in section 2.2.4, applying the low Ni content catalysts in DRM may encounter the problem of low specific activity due to the lack of active sites. In the DRM reaction, these sites are Ni species in the metal state which are produced in the pre-reduction step of Ni catalysts that transform oxides of Ni into Ni^0. The availability of these Ni^0 domains to the reaction influences the performance of catalysts. Therefore, the reducibility and surface exposure of the Ni species play significant roles in catalytic activity.

The Mg-Al mixed oxides were used as the catalyst supports. It was mentioned that Ni can form stable but poorly reducible structures with MgO or Al_2O_3, negatively influencing the catalyst activity.

Remarkably, $Ni/Mg_{1.3}AlO_x$ catalyst with low Ni content in this section was effectively applied for stoichiometric DRM at low temperature and high GHSV [149]. In this chapter, the influence of Mg-Al support composition and pre-treatment temperature on Ni catalyst activity will be discussed. Firstly in section 4.1, the contribution of these two parameters to the structural, surface and redox properties and Ni coordination of the catalysts will be studied. Afterwards, in section 4.2 and 4.3, the correlation between these catalyst attributes and the performance in terms of CH_4 and CO_2 conversions will be clarified. Finally, section 4.4 will describe the performance of the best catalyst in DRM activity test from 500 °C to 780 °C in comparison with calculated thermodynamic balance. Comparatively high GHSV was applied in all experiments within this chapter in order to benchmark with similar investigations from the literature.

4.1 Catalytic characterization

The crystalline structures of all supports and the corresponding Ni catalysts were characterized by X-ray diffraction. Figure 4.1 depicts the XRD patterns of Mg-Al mixed oxides (Mg/Al = 1.3) including $Mg_{1.3}AlO_x$ and thermally pre-treated samples thereof at different temperatures from 700 °C to 1000 °C. Therein are also indicated the reference reflections for suitable materials that contain high degree of γ-Al_2O_3 (ICDD file No. 00-010-0425) [150], periclase (the cubic form of magnesium oxide, ICDD file No. 00-045-0946) [151] and $MgAl_2O_4$ (ICDD file No. 00-021-1152) [152] crystalline phases. When there was no pre-treatment applied to $Mg_{1.3}AlO_x$ or the pre-treated temperatures did not exceed 800 °C, the resulting materials show broad reflections at about $2\theta = 43.5°$ and 63° which have 2θ values higher than those of periclase but lower than that of γ-Al_2O_3. Therefore, these reflections reveal the incorporation of Al_2O_3 with small Al^{3+} cations into the bulk of periclase (MgO) lattice, resulting in a mixed structure between two oxides [153, 154]. This structure could be named as a solid solution according to [154] in order to be distinguished from well-known $MgAl_2O_4$ spinel. Increasing pre-treatment temperature of $Mg_{1.3}AlO_x$ adjusts such Mg-Al incorporation in the solid solution which can be observed via the shifts of XRD reflections to lower 2θ values. At 800 °C, the pattern of such solid solution is still observable but other broad reflections (2θ = 31.3°; 37°; 45°; 55.5°; 59°; 65°) are also seen, which can be assigned to the initial formation of $MgAl_2O_4$ phase. Opposed to these Mg-Al samples, $Mg_{1.3}AlO_x$.1000 discloses no reflection of mentioned solid solution structures while XRD peaks corresponding to periclase (MgO) and $MgAl_2O_4$ phases become sharp and characteristic, reflecting the high crystallinity of these structures. Such transformations from hydrotalcite precursors into several Mg-Al mixed oxide structures were also mentioned in other studies [153, 155, 156] focusing on the thermal decomposition behaviour of these precursor materials, particularly when a low heating rate was applied.

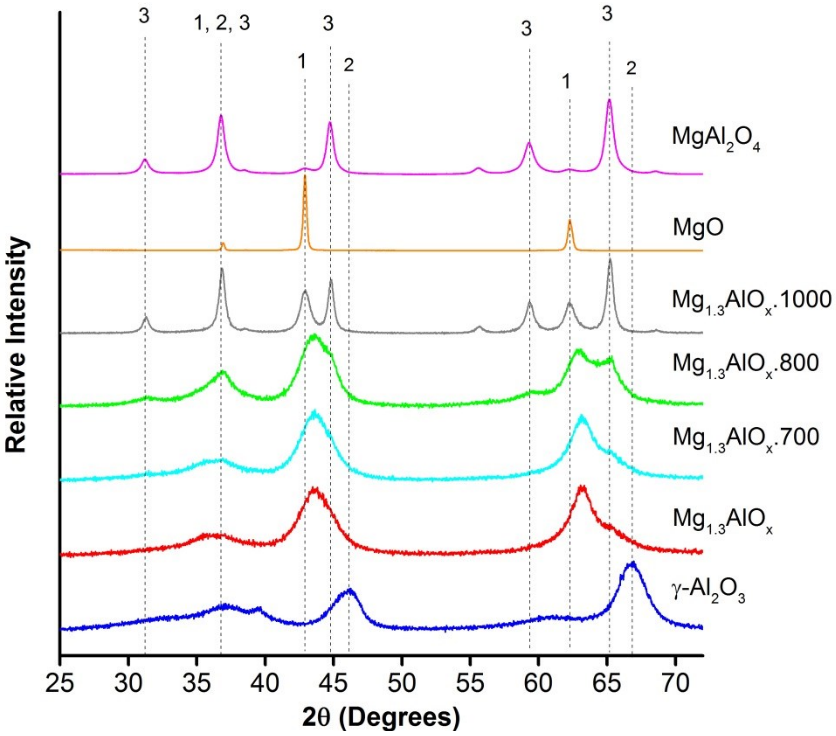

Figure 4.1. XRD patterns of the references (MgO, γ-Al_2O_3, $MgAl_2O_4$) and the Mg-Al bare supports pretreated at different temperatures. Phase symbols: periclase (MgO) (1), γ-Al_2O_3 (2), $MgAl_2O_4$ (3).

The XRD patterns of as-calcined Ni catalysts supported on these Mg-Al supports (Mg/Al = 1.3) were characterized (Figure 4.2). Generally, Ni/$Mg_{1.3}AlO_x$ and Ni/$Mg_{1.3}AlO_x$.700 display XRD patterns similar to that of $Mg_{1.3}AlO_x$.800 due to the phase transformation during the calcination step with the temperature (800 °C) being higher than that in the support thermal treatments. However, compared to XRD pattern of $Mg_{1.3}AlO_x$.800, Ni/$Mg_{1.3}AlO_x$.800 shows additional diffractions at 2θ = 34.8°, 38.9° and 60.5° probably corresponding to $Mg_6Al_2(OH)_{18}\cdot 4.5H_2O$ (ICDD file

No. 00-035-0965) in the rhombohedral structure as the result of the rehydration of calcined hydrotalcite ($Mg_{1.3}AlO_x$.800) during the Ni impregnation step [154]. In contrast, the Ni impregnation onto $Mg_{1.3}AlO_x$.1000 and its subsequent calcination produced the catalyst Ni/$Mg_{1.3}AlO_x$.1000 with an XRD pattern similar to the support.

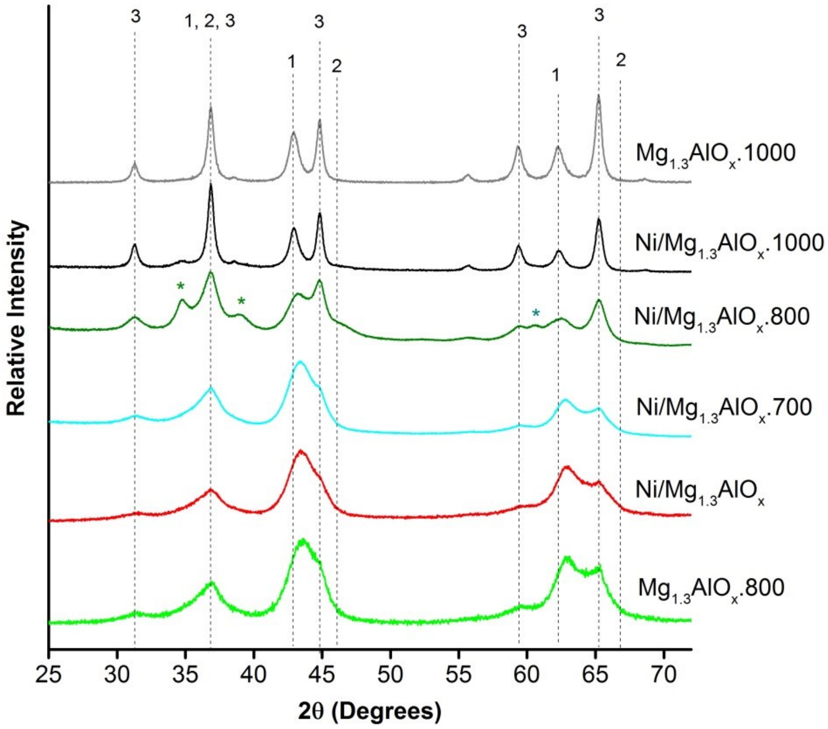

Figure 4.2. XRD patterns of Ni catalysts (all calcined at 800 °C) and two Mg-Al supports (Mg/Al = 1.3) calcined at 800°C or 1000 °C. Phase symbols: periclase (1), γ-Al_2O_3 (2), $MgAl_2O_4$ (3), $Mg_6Al_2(OH)_{18}\cdot 4.5H_2O$ (*).

As $Mg_{1.3}AlO_x$ was chosen for the next study on the effect of Mg-Al support with different Mg/Al molar ratios, the supports $Mg_{0.5}AlO_x$ and Mg_3AlO_x were prepared by hydrotalcite calcination at 550 °C without any further pre-treatment and applied to Ni catalyst preparation. The final catalysts were also subsequently calcined at 800 °C before being tested. XRD patterns of these Ni catalysts are depicted in Figure 4.3. Besides, XRD profiles of Ni/MgO and Ni/Al_2O_3 are also shown as the references. The magnification of XRD patterns in 2θ range from 61.5° to 63° of MgO and Ni/MgO samples is also illustrated. XRD patterns of the Ni catalysts supported on single oxides, MgO or Al_2O_3, depicts the slight shifts compared to the diffractions of periclase or γ-Al_2O_3 phases, respectively, reflecting the formation of NiO-MgO solid solution [157] or $NiAl_2O_4$ spinel structures [158]. The patterns of Mg-Al supported Ni catalysts represent the combination of different structures. Ni/$Mg_{0.5}AlO_x$ discloses main reflections at the positions close to that of $MgAl_2O_4$. On the other hand, such spinel diffractions are less intensive in Ni/$Mg_{1.3}AlO_x$ and Ni/Mg_3AlO_x XRD patterns. In the XRD profiles of both latter samples, the major diffraction peaks nearly locate at 2θ positions belonging to periclase structure. However, among these two samples, Ni/Mg_3AlO_x with lower Al content shows the reflections at 2θ positions being closer to that in Ni/MgO XRD pattern, reflecting the Ni-Mg-Al solid solution structure with less concentration of Al_2O_3 in the periclase parent structure [153].

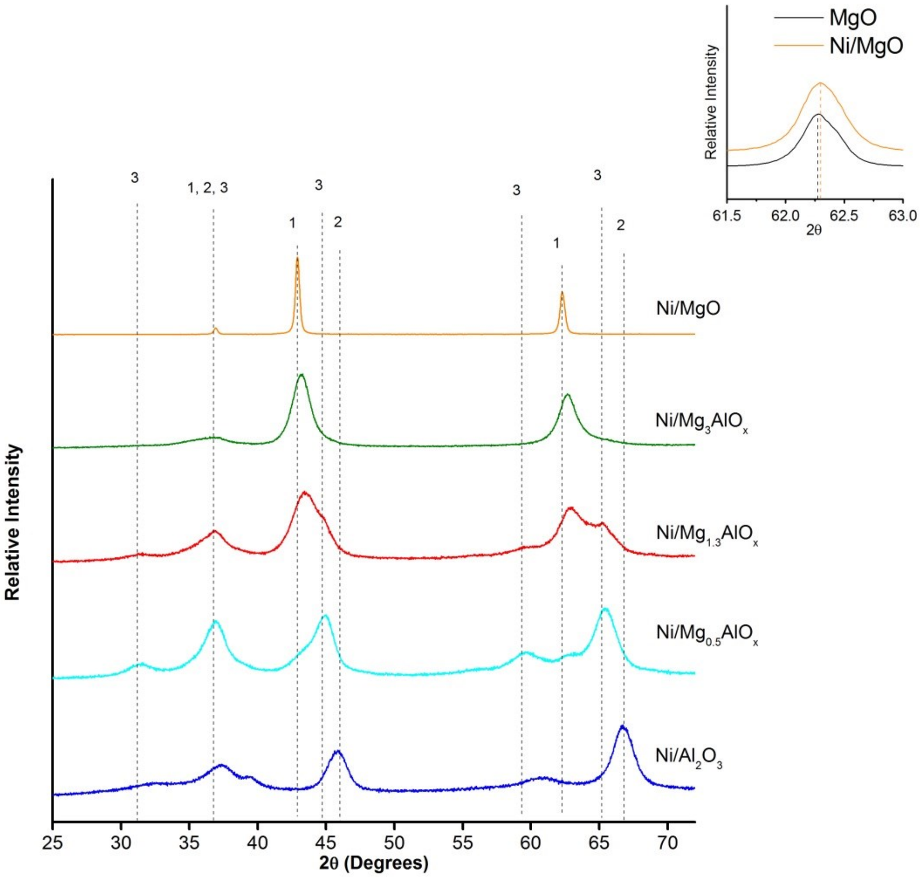

Figure 4.3. XRD patterns of Ni catalysts (all calcined at 800 °C) with different Mg/Al molar ratio with crystalline phases: periclase (MgO) (1), γ-Al_2O_3 (2), $MgAl_2O_4$ (3).

It should be noted that in the XRD results of all Ni catalysts in both series, the absence of specific NiO diffractions may generally reflect the fact that the crystallites of this oxide are smaller than the detection limit of XRD measurements [159, 160]. This absence is probably due to the low content of Ni and high calcination temperature applied for these catalysts, leading to the fine dispersion of Ni species which may diffuse into the bulk of Mg-Al mixed oxides [160].

The XRD measurements of two spent Ni catalysts collected after DRM at 650 °C were conducted and presented in Figure 4.4 in order to determine the effect of Mg in the stabilization of catalysts during the reaction. Ni metal species (Ni^0), which are the result of the pre-reduction process with H_2 before DRM as well as the reduction by CO/H_2 mixture during the reaction, were detected with reflections at 2θ = 44.5° and 51.8° (ICDD file No. 01-071-3740) in spent Ni/Al_2O_3. Compared to the fresh one, this change is assigned to the formation of highly crystalline Ni^0 domains due to agglomeration during reaction. In contrast, the XRD pattern of spent $Ni/Mg_{1.3}AlO_x$ displays a similar profile as the fresh sample without Ni^0 domains, proving the stability of the Ni dispersion during the reaction. This result probably depicts the incorporation of Ni species into the stable structures of solid solution and/or $MgAl_2O_4$ spinel that can prevent the structural transformation and particle migration at the high reaction temperature [40, 44, 45].

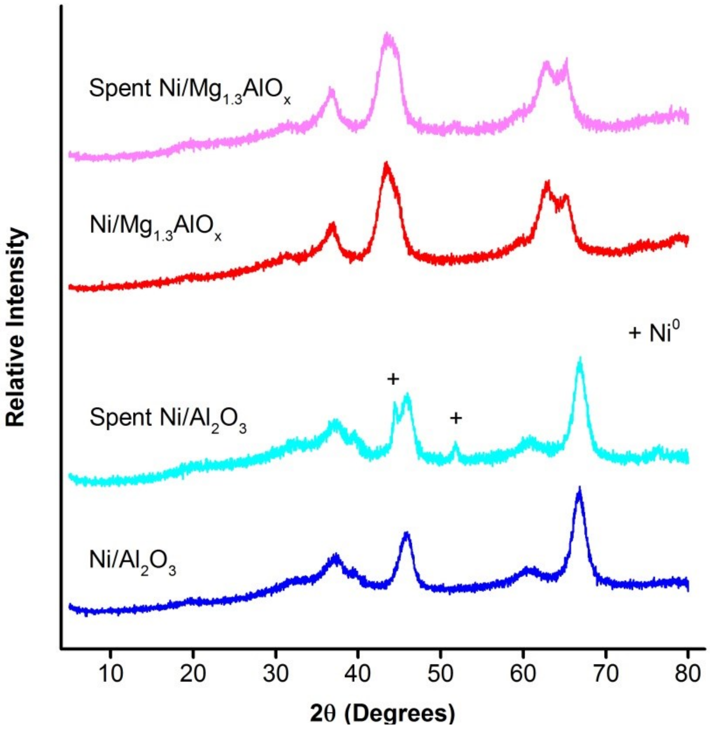

Figure 4.4. XRD patterns of fresh and spent Ni catalysts samples: Ni/Al_2O_3 and $Ni/Mg_{1.3}AlO_x$ after DRM (650 °C, 1 bar, CH_4: CO_2 = 1, GHSV = 85 L/(g_{cat}×h), TOS = 8 h).

The textural parameters of the calcined Ni samples are summarized in Table 4.1. The supported Ni catalysts show comparable surface area and pore volume, except Ni/MgO and $Ni/Mg_{1.3}AlO_x$.1000. $Ni/Mg_{1.3}AlO_x$.1000 possesses quite low surface area probably because its support was calcined at higher temperature (1000 °C) and sintering and collapsing may have occurred. However, in any case, no limitation by internal diffusion was expected for the feed molecules, which have the kinetic diameters [161] being smaller compared to the size of the pores.

Table 4.1. Textural properties of Ni catalysts.

Catalyst	S_{BET} (m^2/g)	Total pore volume (cm^3/g)	Average Pore Diameter (Å)
$Ni/Mg_{1.3}AlO_x$	174	0.40	74
$Ni/Mg_{1.3}AlO_x$.700	167	0.39	71
$Ni/Mg_{1.3}AlO_x$.800	165	0.38	70
$Ni/Mg_{1.3}AlO_x$.1000	82	0.36	126
$Ni/Mg_{0.5}AlO_x$	154	0.43	95
Ni/Mg_3AlO_x	162	0.42	70
Ni/Al_2O_3	178	0.47	81
Ni/MgO	45	0.33	318

The reducibility of supported Ni catalysts after calcination was evaluated by TPR measurements (Table 4.2, Figure 4.5 and Figure 4.6). Ni^{2+} species are the main reducible ones in all catalysts. The TPR measurement of unsupported NiO as the reference for these Ni samples was also conducted (Figure 4.5). In this test, an intense peak at 350 °C was observed, indicating the bulk NiO reduction. In contrast, all supported Ni samples display poorer reducibility with the main reduction peaks appearing first above 600 °C possibly due to several factors: the low Ni loading leading to the formation of highly dispersed Ni species and the stable structure generation between Ni and MgO and/or Al_2O_3 in the supports at high sample calcination temperature as confirmed by XRD (Figure 4.2 and Figure 4.3). These factors probably cause strong interaction of Ni^{2+} and the corresponding supports, suppressing the formation of observed bulk NiO species being reducible at lower temperature [157, 162]. Ni/Al_2O_3 shows high-temperature reduction peaks at 850 °C and the reduction is incomplete up to 1000 °C (Figure 4.6). This poor reducibility is caused by nickel aluminate spinel species in alumina supported samples, especially when low content of Ni and high calcination temperature were used [163]. Ni/MgO exposes apparently poor reducibility with low H_2 consumption (Figure 4.6 and Table 4.2). However, TPR profile of this sample discloses a low-temperature peak at around 400 °C, possibly relating to the reduction of Ni^{2+} species in the outer face or subsurface layers of the MgO lattice. In contrast, the high-temperature shoulder of such profile is assigned to the reduction of the Ni species located in periclase lattice, forming a stable solid solution structure [157].

Table 4.2. The H_2 consumption of Ni catalysts in TPR measurement.

Catalyst	H_2 consumption (μmol/g)
Ni/$Mg_{1.3}AlO_x$	494
Ni/$Mg_{1.3}AlO_x$.700	474
Ni/$Mg_{1.3}AlO_x$.800	450
Ni/$Mg_{1.3}AlO_x$.1000	404
Ni/$Mg_{0.5}AlO_x$	469
Ni/Mg_3AlO_x	487
Ni/Al_2O_3	397
Ni/MgO	181
Theoretical H_2 uptake for $Ni^{2+} \rightarrow Ni^0$ for 2.5 wt% Ni	428

Reducibility of Ni catalysts supported on different Mg-Al supports (Mg/Al = 1.3) was evaluated (Figure 4.5). These samples except Ni/$Mg_{1.3}AlO_x$.1000 expose similar TPR profiles but are different in H_2 consumption (Table 4.2). On the other hand, Ni/$Mg_{1.3}AlO_x$.1000 discloses a shift of reduction peak maximum to higher temperature (900 °C) and lower hydrogen consumption, illustrating the presence of poorly reducible Ni^{2+} species that probably have stronger interaction with the support [46, 164].

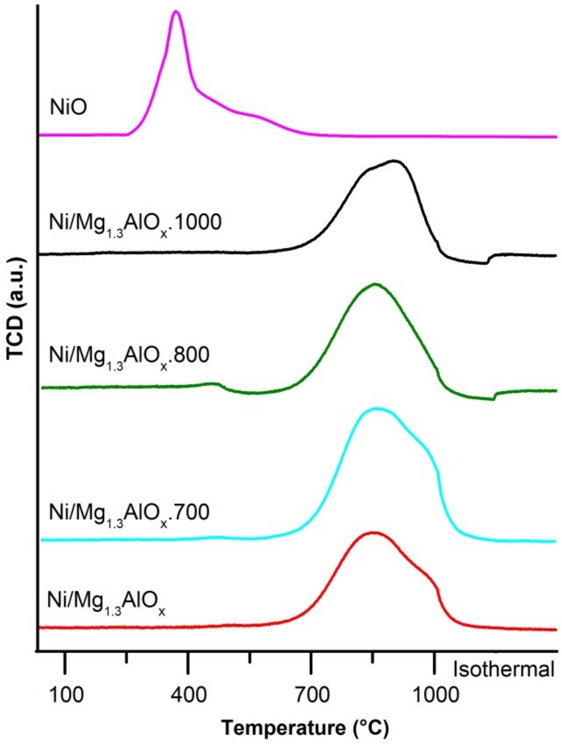

Figure 4.5. TPR profiles of Mg-Al supported Ni catalysts (Mg/Al = 1.3). The profile of NiO was normalised to the relative Ni weight percentage of supported Ni samples (2.5 wt%).

Mg-Al supported Ni catalysts with various Mg/Al molar ratio show a TPR peak starting at 550 °C (Figure 4.6), reflecting the reduction of mainly recalcitrant Ni^{2+} species in the solid solution [164] and/or in the spinel structure [165]. These catalysts demonstrate higher H_2 consumption compared to Ni/Al_2O_3 or Ni/MgO, probably showing the benefit of availability of both Al_2O_3 and MgO at the same time in the support that lead to the formation of more stable $MgO-Al_2O_3$ mixed structures instead of other poorly reducible Ni species, such as $NiAl_2O_4$ spinel or NiO-MgO solid solution [47, 166]. Among the Mg-Al mixed oxides with different Mg/Al ratios, Ni^{2+} species supported on either MgO- or Al_2O_3-rich materials show poorer reducibility compared to those in $Ni/Mg_{1.3}AlO_x$. Indeed, this catalyst discloses the highest H_2 uptake (Table 4.2) and a reduction peak starting at the lowest temperature (550 °C). However, the broader peak of reduction found in such sample suggests less homogeneous dispersion of Ni^{2+} in the bulk of the catalyst.

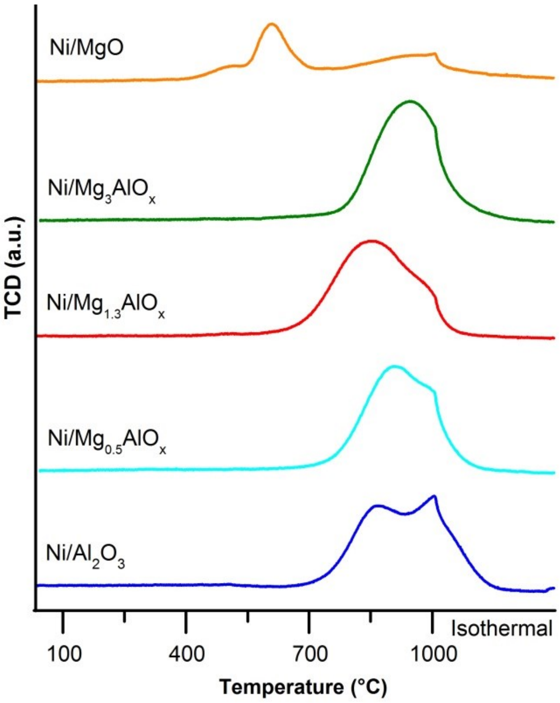

Figure 4.6. TPR profiles of Mg-Al supported Ni catalysts with different Mg/Al ratio.

XPS measurements were implemented to characterize the surface nature of the materials. The binding energy (BE) values were also evaluated to indicate the oxidation states of the atoms as well as their chemical and physical environment. All the samples show the binding energy around 854-857 eV (Table 4.3) corresponding to the Ni $2p_{3/2}$ region [124, 167]. These are close to the BE values that were observed for free NiO (854 eV) [168], Ni_2O_3 (856 eV) [164, 167], $NiAl_2O_4$ (856 eV) [164, 167], NiO-MgO solution (855.7 eV [169] or 856 eV [170]) and solid solution Mg(Ni,Al)O (855.5 eV) [164].

In any case except Ni/$Mg_{0.5}AlO_x$, the BEs of Ni $2p_{3/2}$ have values higher than that of free NiO, suggesting the transfer of electrons from nickel to electron-poor Mg^{2+} and/or Al^{3+} species in the structure [164, 170]. These results generally indicate strong interaction of Ni with supports, as seen in TPR results, lowering its reducibility compared to pure NiO (Figure 4.5 and Figure 4.6).

Table 4.3. XPS and ICP results for the catalysts.

Sample	**BE (eV)**	**Surface molar ratio** [1]		**Bulk molar ratio** [2]	
	Ni $2p_{3/2}$	Ni/(Mg+Al)	Mg/Al	Ni/(Mg+Al)	Mg/Al
Ni/Al_2O_3	855.5	0.029	-	0.022	0
Ni/MgO	- [3]	- [3]	-	0.017	-
Ni/$Mg_{0.5}AlO_x$	853.7	0.036	0.3	0.021	0.5
Ni/Mg_3AlO_x	856.5	0.024	0.6	0.018	3.0
Ni/$Mg_{1.3}AlO_x$	856.9	0.063	0.4	0.019	1.3
Ni/$Mg_{1.3}AlO_x$.700	856.9	0.027	0.6	0.019	1.3
Ni/$Mg_{1.3}AlO_x$.800	861.7	0.043	1.0	0.019	1.3
Ni/$Mg_{1.3}AlO_x$.1000	856.1	0.057	0.3	0.019	1.3
$Mg_{1.3}AlO_x$	-	-	1.2	-	1.3
$Mg_{1.3}AlO_x$.800	-	-	1.1	-	1.3
$Mg_{1.3}AlO_x$.1000	-	-	1.5	-	1.3

(1) XPS results; (2) ICP results; (3) Ni content is below the XPS detection limit.

Regarding the Mg/Al surface ratio, the Ni catalysts show remarkable differences from their corresponding supports, suggesting the dissolution and re-dispersion of the Mg^{2+} and Al^{3+} of the supports during the impregnation step. It is not yet fully understood but the surface Ni concentrations of those samples are still comparable.

Comparison of the surface Ni/(Mg+Al) ratio (from XPS) and bulk composition (from ICP) (Table 4.3) highlights the preferred location of Ni in different supports. Regarding the reference samples, Ni/MgO exposes almost no Ni on the surface and Ni/Al_2O_3 shows slightly higher surface Ni/(Mg+Al) ratio (0.029) compared to the corresponding bulk values (0.022). On the other hand, Ni catalysts supported on Mg-Al mixed oxides reveal that Ni is preferably located on the surface indicated by higher atom ratios (0.024-0.063) compared to their bulk values (0.018-0.021). These data reflect the Mg-Al coexistence in the supports that can avoid the Ni diffusion into the pure MgO or Al_2O_3 lattices, subsequently augmenting the active Ni species on the outer shell of materials [47]. Among such Ni catalysts, Ni/$Mg_{1.3}AlO_x$ discloses highest surface Ni/(Mg+Al) ratio, which may correlate with its best reducibility (Figure 4.5 and Figure 4.6). Applying the thermal pre-treatment to $Mg_{1.3}AlO_x$ support before final catalyst preparation and calcination or varying the Mg/Al molar ratio to 0.5 or 3 resulted in less Ni^{2+} domains on the surface available for reduction.

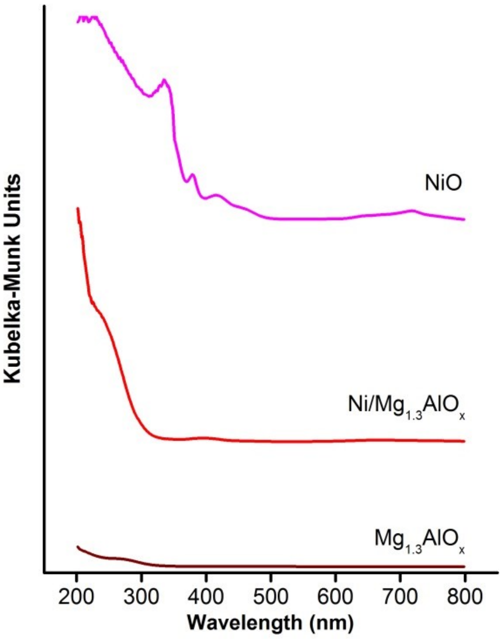

Figure 4.7. UV-Vis-DR spectra of NiO, $Ni/Mg_{1.3}AlO_x$ and the corresponding support.

The coordination of the nickel species (mostly Ni^{2+}) in the samples was examined by UV−Vis-DRS. Almost no absorption can be seen for the support sample (Figure 4.7). On the other hand, the UV-Vis-DR spectra of the Ni impregnated samples show light absorption bands, suggesting that only Ni species are sensitive at the chosen analysis conditions. As a reference, UV−Vis-DR spectrum of NiO calcined at 800 °C was also measured. The sample reveals strong absorption over the whole range of 200–800 nm which can be assigned to nonstoichiometric NiO containing some Ni^{3+} domains [139].

The UV-Vis-DR spectra of the Ni-impregnated samples expose intense signals in the UV region of 250–350 nm (Figure 4.8a), which relate to the $O^{2-} \rightarrow Ni^{2+}$ ligand to metal charge transfer (LMCT) in octahedral NiO lattice [139]. Mg-Al supported Ni catalysts show shoulders in the range of 250-350 nm which cannot be found in the spectra of Ni/MgO or Ni/Al_2O_3, suggesting weaker metal support interaction (MSI) in Ni samples with Mg-Al mixed oxides [159]. Among these Mg-Al supported Ni catalysts, $Ni/Mg_{1.3}AlO_x$ induces the strongest red-shift of LMCT band of NiO, which points to the weakest interaction of Ni species and support. This result together with data from XPS (Table 4.3) can be used to explain the excellent reducibility of $Ni/Mg_{1.3}AlO_x$ among Ni catalysts (Figure 4.5 and Figure 4.6). Indeed, as

$Ni/Mg_{1.3}AlO_x$ contains Ni^{2+} species preferably locating on the surface and having lower MSI with the support, it is more easily reduced than other Mg-Al supported catalysts.

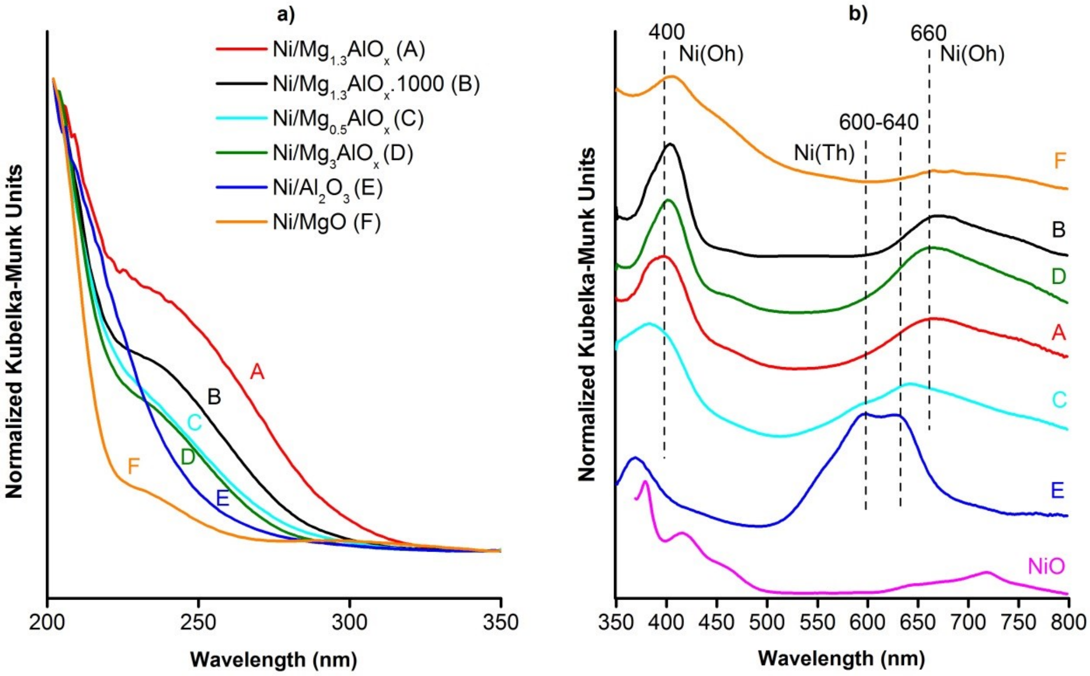

Figure 4.8. UV-Vis-DR spectra in the region a) 200-350 nm and b) 350-800 nm of Ni catalysts and the references Ni/MgO, Ni/Al_2O_3 and bulk NiO. Ni(Oh): Ni species in octahedral coordination; Ni(Th): Ni species in tetrahedral coordination.

The UV-Vis-DR spectra in the visible region (350–800 nm) of Ni catalysts can be seen in Figure 4.8b. The signals in this visible region represent d → d transitions of Ni^{2+} ions mainly in octahedral (Oh) and tetrahedral coordination (Th) [171]. As a reference, NiO displays intense signals at 380, 420 and 720 nm which illustrate the Ni^{2+} (Oh) in the cubic (rock-salt) NiO lattice [172]. Ni/MgO displays a spectrum similar to that of NiO sample. It presents an intense signal at 410 nm and a wide band at 600−800 nm which suggests a majority of Ni^{2+} (Oh) species. These bands belong to the solid solution of NiO and MgO as Ni species migrate into the MgO lattice, which has cubic rock-salt structure as well [173]. The absence of intense signals at 380 nm and 720 nm is probably due to the lack of bulk NiO formation in Ni/MgO [174]. This formation of the solid solution instead of bulk NiO is supported by the XRD pattern of Ni/MgO (Figure 4.3), in which no crystalline structure of NiO was found but shifts of main diffractions compared to those in the pattern of MgO. Indeed, the low content of Ni in the sample and strong interaction between NiO and MgO result in the high dispersion of Ni species, thus suppressing the agglomeration of NiO during the calcination. Ni/Al_2O_3, on the other hand, shows a doublet signal at 600−640 nm which is related to the Ni^{2+} (Th) species in the nickel aluminate spinel lattice [158, 172, 175]. Besides, a small absorption band at 380 nm can be assigned to Ni^{2+} (Oh) in the $NiAl_2O_4$ spinel [174].

By comparing to such references, the Mg-Al supported Ni samples in this study show the combination of different types of coordination when Mg/Al ratios and support pre-treatments are varied. Ni/$Mg_{0.5}AlO_x$ presents the doublet signal at 600−640 nm relating to the Ni^{2+} (Th) species in the spinel structures ($Mg_{1-x}Ni_xAl_2O_4$) of the support framework which were evidenced by XRD (Figure 4.3). These Ni^{2+}(Th) species probably are responsible for the lower reducibility in case of Ni/Al_2O_3 and Ni/$Mg_{0.5}AlO_x$ compared to that of Ni/$Mg_{1.3}AlO_x$ with higher contribution of Ni^{2+}(Oh) (Figure 4.6) [84, 176]. This comparison predicts the ability of Mg^{2+} to preferably react with Al^{3+} ions which subsequently lowers the tendency towards Ni^{2+}(Th) and $NiAl_2O_4$ formation [75, 84].

Ni/Mg_3AlO_x with MgO-rich support predominantly exposed the formation of Ni^{2+}(Oh) with the intense signal at 410 nm close to that of Ni/MgO and a broad band at 600−800 nm. As suggested by XRD (Figure 4.3), Ni/Mg_3AlO_x comprises mostly the MgO-rich solid solution with the cooperation of Al^{3+} in a periclase structure where both Mg^{2+} and Al^{3+} have octahedral coordination [173]. By combing these XRD and UV-Vis observations, it can be suggested that Ni^{2+} species in Ni/Mg_3AlO_x expose the same coordination when diffusing into such solid solutions and predominantly interacting with MgO. Ni/$Mg_{1.3}AlO_x$ also depicts a majority of Ni^{2+} (Oh) although the catalyst comprises solid solution and spinel structures of Mg-Al mixed oxides (Figure 4.1 and Figure 4.2). However, compared to Ni/Mg_3AlO_x, this catalyst shows the blue-shift of the band at around 400 nm toward the position of Ni^{2+} (Oh) in Ni/Al_2O_3 (Figure 4.8b). This shift depicts the change in solid solution environment, where more Al^{3+} ions interact with Ni^{2+}. Such difference between Ni/$Mg_{1.3}AlO_x$ and Ni/Mg_3AlO_x probably points out less NiO-MgO interaction in Ni/$Mg_{1.3}AlO_x$, probably resulting in higher reducibility of Ni^{2+} in this sample (Figure 4.6) [177].

Likewise, compared to Ni/$Mg_{1.3}AlO_x$.1000, Ni/$Mg_{1.3}AlO_x$ shows similar band blue-shift being assigned to less NiO-MgO interaction which possibly also results in the weaker MSI (Figure 4.8a) and better reducible Ni species in the latter sample (Figure 4.5).

4.2 Effect of support pre-treatment on the catalytic activity

Blank tests at the reaction conditions applied for Ni catalysts were implemented with the diluting material (SiC) or only with the supports (not shown). No activity was observed at the favoured conditions. Figure 4.9 exposes the CH_4 and CO_2 conversions in DRM during 8 h on stream over Ni catalysts at 650 °C with various Mg-Al mixed oxides supports (Mg/Al = 1.3) with or without the thermal pre-treatment. The comparatively mild reaction conditions (650 °C, 1 bar, CH_4: CO_2 = 1, GHSV = 85 L/(g_{cat}×h)) were chosen to operate the catalysts in a kinetically controlled regime so that their performance can be differentiated. Ni/$Mg_{1.3}AlO_x$ presents the highest conversion of both CH_4 and CO_2 while supporting Ni^{2+} on $Mg_{1.3}AlO_x$.1000 resulted in a catalyst with lowest conversions. These activity results are corresponding to the reducibility (Figure 4.5 and Table 4.2), surface Ni concentration (Table 4.3), and surface area (Table 4.1) of the Ni catalysts. Indeed, Ni/$Mg_{1.3}AlO_x$ reveals most suitable properties, especially high Ni surface exposure and reducibility with lowest reduction temperature and highest H_2 consumption in TPR measurements. By that, it can be suggested that more active Ni sites were formed on the surface in the pre-reduction step, and thus higher DRM activity was obtained. Ni/$Mg_{1.3}AlO_x$ was then chosen for the next study due to its excellent activity.

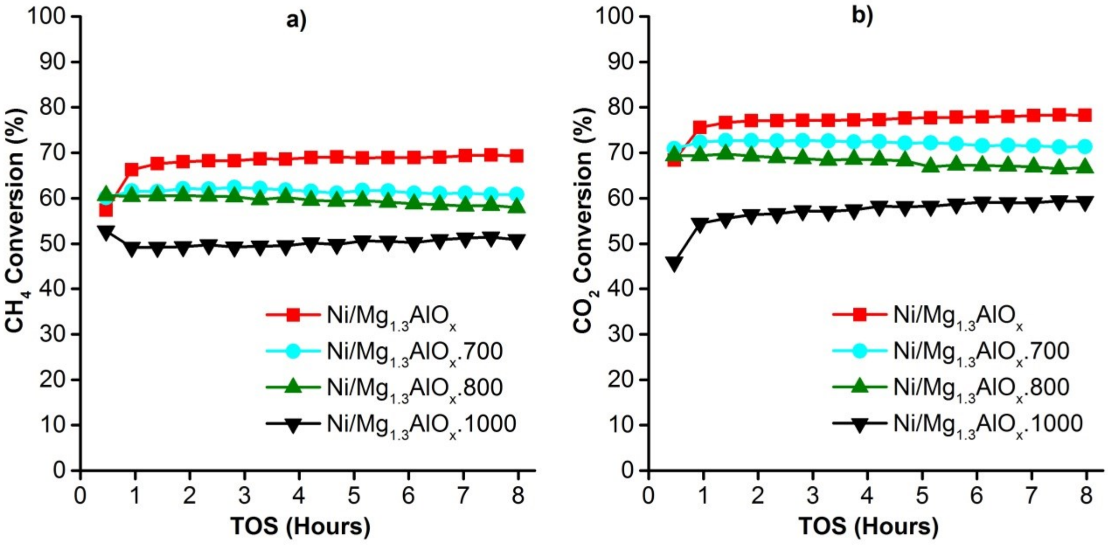

Figure 4.9. Conversions of a) CH_4 and b) CO_2 in DRM on different Mg-Al supported Ni catalysts(Mg/Al = 1.3) (DRM conditions: 650 °C, 1 bar, CH_4/CO_2 = 1, GHSV = 85 L/(g_{cat}×h)). All the catalysts were pre-reduced in situ at 700 °C for 1 hour prior to the reaction.

4.3 Effect of Mg/Al ratio on the catalytic activity

The Ni catalysts in this series of DRM tests are supported on Mg-Al supports with different Mg/Al ratio from 0.5 to 3 (Figure 4.10). These are Ni/$Mg_{0.5}AlO_x$, Ni/$Mg_{1.3}AlO_x$ and Ni/Mg_3AlO_x prepared from the corresponding supports calcined at 550 °C and without any further thermal-pre-treatment. The performances of Ni/Al_2O_3 and Ni/MgO were also presented as the references. The higher and more stable activity can be attained with Mg-Al supported Ni catalysts compared to Ni/Al_2O_3 or Ni/MgO. The deactivation found in Ni/Al_2O_3 could be explained by the serious agglomeration of Ni species during the reaction which was observed via XRD results (Figure 4.4) of the corresponding spent sample recovered after 8 h on stream. Among the Mg-Al supported Ni catalysts, highest conversions of CH_4 and CO_2 are obtained on Ni/$Mg_{1.3}AlO_x$. This result can be also explained by the TPR and XPS results in which Ni/$Mg_{1.3}AlO_x$ exposed excellent reducibility (Figure 4.6 and Table 4.2) and highest availability of surface Ni species (Table 4.3). These attributes of Ni/$Mg_{1.3}AlO_x$ are probably related to its lowest MSI (Figure 4.8a), as the solid solution of Ni^{2+}, Mg^{2+} and Al^{3+} was formed with proper amounts of MgO and Al_2O_3 that can suppress both strong NiO-MgO interaction and the formation of $NiAl_2O_4$ spinel (Figure 4.8b) [166].

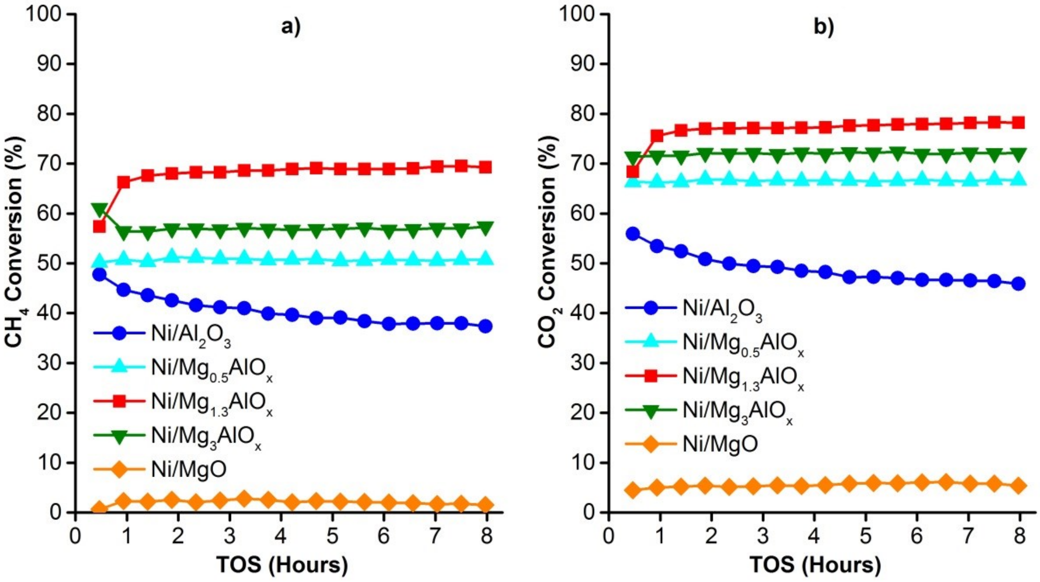

Figure 4.10. Conversions of a) CH_4 and b) CO_2 on Ni catalysts with different Mg/Al ratio in DRM (650 °C, 1 bar, $CH_4/CO_2 = 1$, GHSV = 85 L/(g_{cat}×h)). All the catalysts were pre-reduced in situ at 700 °C for 1 hour prior to the reaction.

4.4 Catalytic performance of Ni/$Mg_{1.3}AlO_x$ at 500 °C–780 °C

In order to benchmark such high activity of Ni/$Mg_{1.3}AlO_x$, additional DRM tests at lower temperature but same GHSV were investigated. Figure 4.11 exposes the excellent performance of Ni/$Mg_{1.3}AlO_x$ at 500–780 °C in comparison with the thermodynamic limit [50]. CH_4 and CO_2 can be converted already around 500 °C. It should be noted that DRM is highly endothermic and the reaction demands high temperatures to convert the CH_4 and CO_2 to syngas. According to the thermodynamic calculations in the literature [50, 178], the reaction starts at 350 °C. However, remarkable conversions were observed only above 500 °C [38]. Some studies claimed catalysts to be active in DRM at very low temperature (400 °C [10] or 450 °C [178]). However, therein extremely beneficial conditions for catalyst efficiency were applied (high content of active sites or usage of noble metals). In this study, the activity of Ni/$Mg_{1.3}AlO_x$ is outstanding considering its low Ni content because it performs with CH_4 and CO_2 conversions close to the calculated limit even at low temperature and high GHSV (85 L/(g_{cat}×h)) in comparison with other investigations [2, 179, 180]. Figure 4.11 also displays the effect of reaction temperature on the H_2/CO ratio. This ratio is always lower than 1 at any set reaction temperature, which points out the contribution of reverse water gas shift reaction (Eq. 5), lowering H_2 selectivity through reaction with CO_2 to form CO and H_2O [1]. RWGS plays a more important role at lower temperature due to the thermodynamic equilibrium [1].

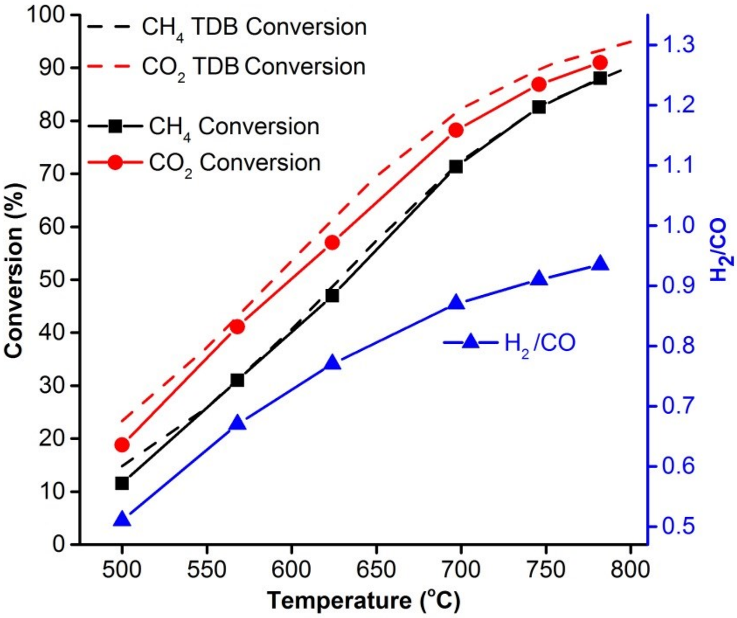

Figure 4.11. Performance of $Ni/Mg_{1.3}AlO_x$ in comparison with the thermodynamic balance (TDB) (1 bar, $CH_4/CO_2 = 1$, GHSV = 85 L/(g_{cat}·h)). Data were collected after 2 hours stabilization at each temperature set point.

4.5 Intermediate conclusion from chapter 4

$Ni/Mg_{1.3}AlO_x$ shows highest DRM activity due to its high specific surface area, weak interaction of the Ni species with corresponding support, high amount of surface Ni species and excellent reducibility. These properties, especially the last attribute, were found to correlate with particular coordination of Ni^{2+}species in the catalyst. Indeed, among the Ni catalysts with Mg-Al supports and various composition and thermal pre-treatment, $Ni/Mg_{1.3}AlO_x$ lacks tetrahedrally coordinated Ni^{2+} species and suppresses NiO-MgO interaction which are both beneficial for its high reducibility.

This sample can activate the reaction at temperature as low as 500 °C with the conversions approaching the thermodynamic limitation even at a considerably high space velocity (85 L/(g_{cat}·h). However, the weak MSI found in $Ni/Mg_{1.3}AlO_x$ possibly leads to the fast agglomeration of Ni during the reaction. This metal agglomeration may both cause deactivation and govern the carbon deposition (6 wt%) from side reactions which will be carefully discussed in the next chapter. As a result, a suitable modification is necessary to reduce both effects but maintain the high catalyst activity.

5 Stabilization of Ni/$Mg_{1.3}AlO_x$ by La and CA-assisted preparation

The previous chapter showed that applying Mg-Al support with a suitable composition and pre-treatment produces a catalyst with low Ni content but active for DRM even at low temperature and high GHSV. However, it encountered the carbon deposition problem after few hours on stream of DRM.

Motivated by this result, some catalyst modification was implemented for low Ni content catalysts with the CA- and La-based procedures being expected to reduce the coking rate and stabilize the performance in DRM with even higher GHSV over longer time [181]. These modifications, using complexing agents in impregnation step or adding rare earth metal elements, have been recognised as being promising in recent papers. However, it is rare to observe these trials carried out together on low Ni catalyst system.

Thus, various modified Ni catalysts were prepared, characterized and analysed in DRM tests with different conditions. The influences of mentioned modifications on Ni coordination, dispersion, MSI and redox properties were evaluated (section 5.1) with respect to the catalytic behaviour in DRM (section 5.2) that revealed catalyst properties and performance relationships. Finally, the long-term DRM tests were conducted in order to study the efficiency of the catalyst modification on the catalyst stability against different deactivation pathways which will be indicated and discussed.

5.1 Catalyst characterization

XRD patterns of $Mg_{1.3}AlO_x$ and $Mg_{1.3}AlO_x$.800 were presented together with the Ni catalysts in Figure 5.1. Both Mg-Al mixed oxides expose complicated structures with solid solution and/or spinel which were previously discussed in section 4.1. However, after impregnation and calcination, the final supported Ni catalysts generally display XRD patterns similar to that of $Mg_{1.3}AlO_x$.800 rather than of $Mg_{1.3}AlO_x$, reflecting the structural change of $Mg_{1.3}AlO_x$ during the catalyst calcination step. The missing reflections of Ni species may suppose finely dispersed Ni^{2+} species in the sample; however, it has to be considered that Ni content is near the detection limit. Additional information is provided by STEM (see below).

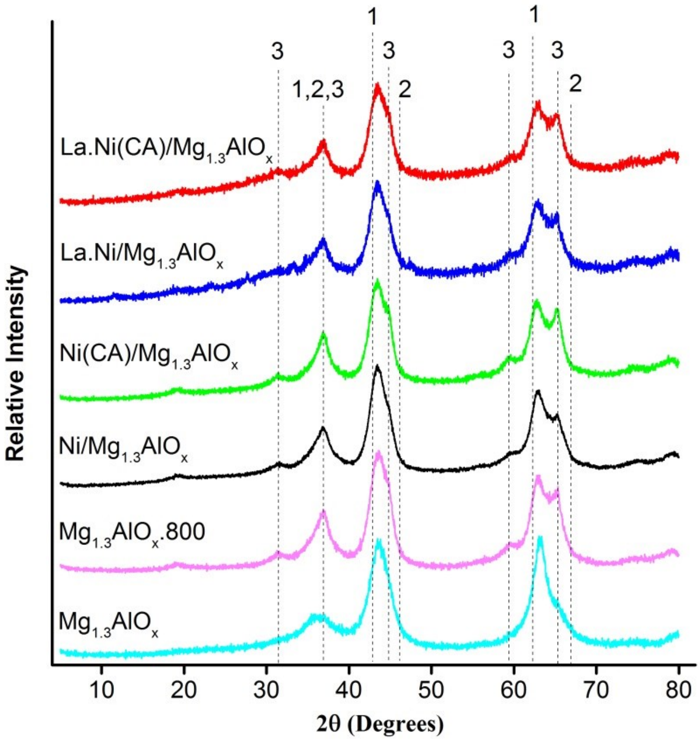

Figure 5.1. XRD patterns of $Mg_{1.3}AlO_x$, $Mg_{1.3}AlO_x$.800 and $Mg_{1.3}AlO_x$ supported Ni catalysts. Phase symbols: periclase (MgO) (1), γ-Al_2O_3 (2), $MgAl_2O_4$ (3).

The textural parameters of Mg-Al mixed oxides and Ni and/or La-containing samples are summarized in Table 5.1.

Table 5.1. Textural properties of calcined catalysts and their supports.

Catalyst	S_{BET} (m^2/g)	Total pore volume (cm^3/g)	Average Pore Diameter (Å)
$Mg_{1.3}AlO_x$	180	0.24	45
$Mg_{1.3}AlO_x$.800	153	0.25	46
Ni/$Mg_{1.3}AlO_x$	174	0.40	74
Ni(CA)/$Mg_{1.3}AlO_x$	156	0.27	53
La.Ni/$Mg_{1.3}AlO_x$	118	0.26	66
La.Ni(CA)/$Mg_{1.3}AlO_x$	144	0.23	53

Both Ni catalysts without La show high specific BET surface corresponding to that of $Mg_{1.3}AlO_x$, which was the material used in impregnation. However, although these catalysts were calcined at 800 °C, their BET surface values are higher than that of $Mg_{1.3}AlO_x$.800, possibly reflecting the restructuring of the surface of such mixed oxides in the low pH impregnation solution (containing Ni^{2+} and/or citric acid) [159]. La-containing Ni catalysts show lower specific surface area and pore volume values than corresponding Ni catalysts due to the surface coverage by La species. However, La.Ni(CA)/$Mg_{1.3}AlO_x$ possesses higher BET surface area than the corresponding La.Ni/$Mg_{1.3}AlO_x$. The pore size values of these $Mg_{1.3}AlO_x$ supported catalysts are comparable and bigger than the feed molecules. By that, the internal diffusion limitation of reactants is probably suppressed.

The reducibility of Ni^{2+} species, which rules the formation of Ni^0 as active sites for DRM, was measured through TPR. TPR profiles and H_2 consumptions of Mg-Al support and Ni catalysts can be observed in Figure 5.2 and Table 5.2, respectively. The Ni elemental contents measured by ICP (Table 5.2) are shown in order to study the fraction of reducible Ni species in each sample. TPR profiles of bulk NiO and $LaNiO_3$ serve as the references and were rescaled due to the differences in Ni^{2+} content compared to the Ni catalysts. While NiO possesses its main TPR peak at 400 °C, representing bulk NiO reduction, there are several additional reduction steps of $Ni^{3+} \rightarrow Ni^0$ from 200 °C to 750 °C [128] observed in $LaNiO_3$. $Mg_{1.3}AlO_x$.800 also exposes a minor reduction peak with the maximum at 920 °C, probably stemming from impurities.

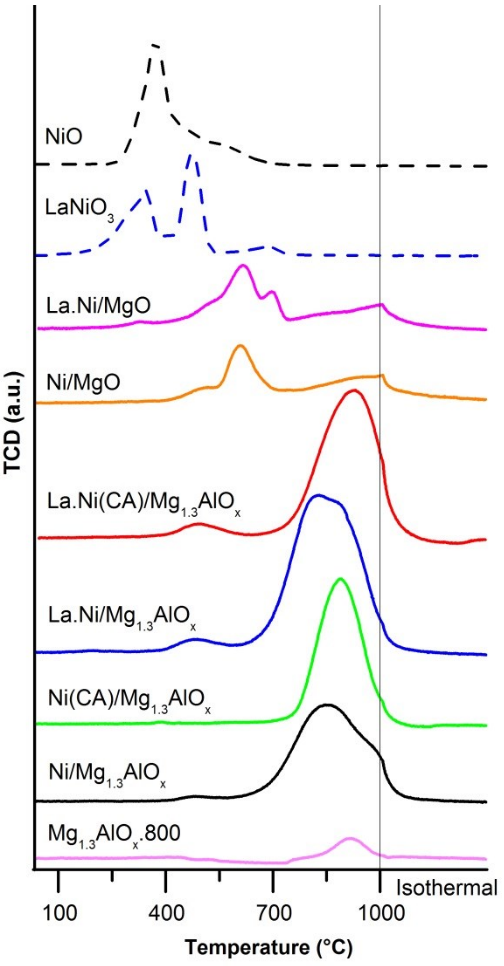

Figure 5.2. TPR profiles of supported Ni catalysts and reference samples. The profiles of NiO and $LaNiO_3$ are normalised to the relative Ni weight percentage in supported Ni catalysts (2.5 wt%).

Reducibility of the Ni catalysts can be discussed in terms of different parameters: the temperature where reduction peaks occur in TPR profile and the related H_2 uptake. Except for Ni/MgO, all supported Ni samples display main peaks of reduction at temperatures above 550 °C, exhibiting the formation of dispersed Ni^{2+} species interacting strongly with the support [157, 162]. Modifying the samples with La and/or CA remarkably affected their reducibility in different ways. Generally, the presence of La enhances the reducibility of samples. For instance, the addition of La to $Ni/Mg_{1.3}AlO_x$ resulted in the shift of the Ni^{2+} main reduction peak from 850 °C to 825 °C and the increase of H_2 consumption (from 494 µmol/g to 550 µmol/g). Similar results were also found in the literature where La was claimed to enhance Ni^{2+} reduction by weakening Ni-support interaction [43, 82-84]. In contrast, the presence of CA in the impregnation step of $Ni(CA)/Mg_{1.3}AlO_x$ and $La.Ni(CA)/Mg_{1.3}AlO_x$ leads to lower reducibility of these Ni species compared to $Ni/Mg_{1.3}AlO_x$ and $La.Ni/Mg_{1.3}AlO_x$, respectively, most likely by increasing the interaction between Ni^{2+} and the support [95, 182].

Table 5.2. H_2 consumption (TPR) and La, Ni contents (ICP) of Ni catalysts, $Mg_{1.3}AlO_x$.800 and the reference samples.

Sample	**H_2 consumption (µmol/g)**	**Ni and La content (wt%)**	
Catalysts and support		**Ni content**	**La content**
$Ni/Mg_{1.3}AlO_x$	494	2.41	-
$Ni(CA)/Mg_{1.3}AlO_x$	450	2.47	-
$La.Ni/Mg_{1.3}AlO_x$	550	2.36	4.38
$La.Ni(CA)/Mg_{1.3}AlO_x$	521	2.49	4.54
$Mg_{1.3}AlO_x$.800	64	-	-
Reference samples			
Ni/MgO	181	2.03	-
La.Ni/MgO	339	2.35	not measured
Theoretical H_2 consumption for $Ni^{2+} \rightarrow Ni^0$ for 2.5 wt% Ni	428	-	-

Besides, the two La-containing samples possess additional low-temperature reduction peaks below 550 °C, appearing close to one of those in $LaNiO_3$. It should be noted that the H_2 consumptions of these La-containing Ni catalysts even exceed the sum of the theoretical value for complete Ni^{2+} reduction to metal (428 µmol/g) and $Mg_{1.3}AlO_x$.800 background value (64 µmol/g). Such high consumption suggests the presence of some Ni^{m+} species (m > 2) in structures with La (e.g., perovskite) [183]. This behaviour was also reported elsewhere [128, 184] with confined $LaNiO_3$

structures supported on solid material which was prepared via a similar impregnation route. However, dissimilar to these publications, the XRD patterns of $LaNiO_3$ are not clearly observed in La containing samples prepared in this study, probably due to the low contents of both La and Ni. Moreover, mentioned low-temperature peaks are spotted clearly in case of Ni/MgO and especially La.Ni/MgO, which also disclose higher reducibility observed in La-containing sample. It should be noted that such peaks are not seen in the case of Ni/Al_2O_3 and La.Ni/Al_2O_3 (not shown here). Therefore, it can be proposed that the presence of La in the MgO-containing catalysts promotes the formation of Ni species with unusual oxidation states and/or structures that contribute to the better sample reducibility.

The surface compositions of the two Ni catalysts without La were measured by XPS (Table 5.3). This method is not suitable for complete sample characterization due to the overlaps of La $3d_{3/2}$ and Ni $2p_{3/2}$ peaks, making the accurate determination of the Ni 2p BE difficult [185]. Both samples show high surface Ni content compared to the ICP bulk values (Table 5.3), indicating the preferred surface locating of Ni species when $Mg_{1.3}AlO_x$ is used as the support. Introduction of CA during preparation further increases the fraction of surface Ni^{2+} species. However, the reducibility of Ni(CA)/$Mg_{1.3}AlO_x$ as previously seen is not as high as that of Ni/$Mg_{1.3}AlO_x$ (Figure 5.2 and Table 5.2). TPR profile of Ni(CA)/$Mg_{1.3}AlO_x$ also shows a sharp and symmetric reduction peak with maximum temperature around 900 °C. These observations suggest that the lower reducibility of Ni(CA)/$Mg_{1.3}AlO_x$ is essentially the result of higher dispersion of Ni species on the catalyst surface [87] having strong interactions with Mg-Al support. Similarly, La.Ni(CA)/$Mg_{1.3}AlO_x$ can be suggested to have better Ni dispersion than La.Ni/$Mg_{1.3}AlO_x$.

Table 5.3. XPS (1) and ICP (2) results for the Ni catalysts without La.

Catalyst	Ni/(Mg+Al)	
	Surface molar ratio 1	**Bulk molar ratio** 2
Ni/$Mg_{1.3}AlO_x$	0.063	0.019
Ni(CA)/$Mg_{1.3}AlO_x$	0.071	0.019

UV-Vis-DRS data of supported Ni catalysts and references are shown in Figure 5.3. In the UV region of 200-350 nm (Figure 5.3a), all samples disclose strong LMCT bands, which appear depending on the Ni^{2+} coordination and aggregation state or dispersion degree [186]. The samples prepared with CA show blue-shifts/lower intensity of the NiO LMCT bands compared to that in Ni/$Mg_{1.3}AlO_x$ and La.Ni/$Mg_{1.3}AlO_x$, pointing out the higher dispersity of Ni species in former samples. This result confirms the effect of CA on Ni dispersity which was seen in XPS results of the two representative samples (Table 5.3). Additionally, these modified Ni catalysts with CA-assisted preparation expose TPR data with main reduction steps at higher temperatures compared to that of CA-free analogues (Figure 5.2). These observations point out the formation of highly disperse Ni species that have higher MSI in cases of La.Ni(CA)/$Mg_{1.3}AlO_x$ and Ni(CA)/$Mg_{1.3}AlO_x$.

The coordination of Ni ions in the samples was examined by UV-Vis-DR spectra in the visible region (350-800 nm). All samples show bands at 400 nm and a wide band at 600-800 nm (Figure 5.3b), exposing the nature of Ni^{2+} (Oh) species mainly located in the solid solution with $Mg_{1.3}AlO_x$ [158, 172, 173]. Indeed, the intense absorption bands or shoulders at 380, 420, 450 and 720 nm found in the reference UV-Vis spectrum of NiO are less pronounced in the spectra of Mg-Al supported Ni catalysts, especially in La.Ni(CA)/$Mg_{1.3}AlO_x$ and Ni(CA)/$Mg_{1.3}AlO_x$. This behaviour indicates the lack of octahedrally coordinated Ni^{2+} in NiO lattices [158, 159, 174] in the catalysts which suggests the effect of CA in the impregnation step and the benefit of low Ni content that both eliminate the formation of accumulated NiO domains during calcination.

Remarkably, the UV-Vis spectrum of La.Ni/$Mg_{1.3}AlO_x$ exposes an additional shoulder at 450-600 nm, which is very similar to that of Ni/MgO and can be assigned to surface Ni^{2+} domains in trigonal bipyramidal or square pyramidal configuration (fivefold coordination). The band for such surface domains was previously reported in the literature [173, 187, 188] where MgO was doped with Ni^{2+} and local defect/distorted structures were formed because the ionic radius of Ni^{2+} (0.069 nm) is slightly smaller than that of Mg^{2+} (0.072 nm) [76]. Such defect structures (shoulders in Figure 5.3b) were seen in the outermost and subsurface layers of the MgO lattice [157] or at face edges (steps) and corners of MgO sites [189, 190]. Such locations were suggested to cause the unusual coordination and oxidation states of Ni species that could be reducible at low temperatures of 400-500 °C or 400-700 °C [191, 192]. Therefore, it can be proposed that La causes the formation of such defective species in La.Ni/$Mg_{1.3}AlO_x$ and more clearly in La.Ni/MgO, contributing to the higher reducibility of these samples compared to Ni/$Mg_{1.3}AlO_x$ and Ni/MgO, respectively (Figure 5.2 and Table 5.2). However, the shoulder at 450-600 nm is not clearly observed in the UV-Vis spectrum of La.Ni(CA)/$Mg_{1.3}AlO_x$, probably relating to the effect of CA-based preparation that increases both La and Ni dispersion and in turn reduces the amount of defective species. This explains also the lower reducibility of this sample compared to La.Ni/$Mg_{1.3}AlO_x$ (Figure 5.2 and Table 5.2).

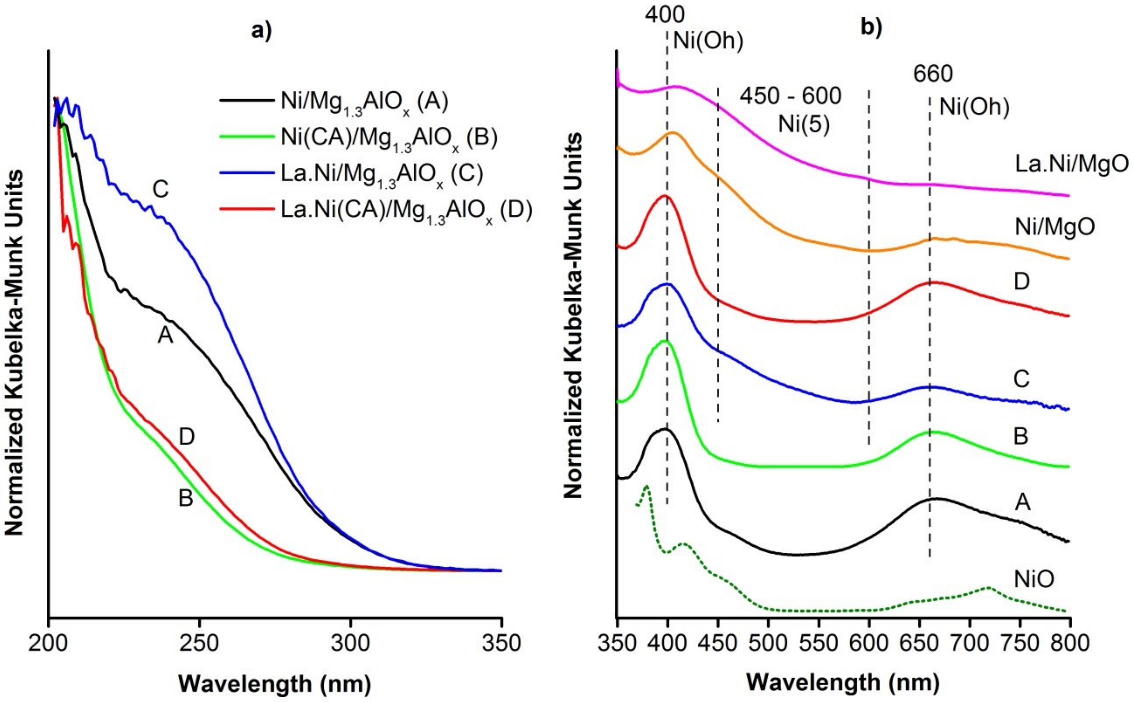

Figure 5.3. UV-Vis-DR spectra in the region a) 200-350 nm and b) 350-800 nm of $Mg_{1.3}AlO_x$ supported catalysts. Ni(Oh): Ni species in octahedral coordination; Ni(5): Ni species in surface fivefold coordination.

The dispersion of Ni after catalyst calcination was visually disclosed by STEM high-angle annular dark field (HAADF) images. Figure 5.4 shows representative images of the various $Mg_{1.3}AlO_x$ supported Ni catalysts with no Ni particles observed. These STEM images may point out, in accordance with the XRD (Figure 5.1) and UV-Vis results (Figure 5.3b), that Ni species are finely dispersed on the surface and/or embedded in the solid structures of the support [193]. For La- containing samples (Figure 5.4c and d), the regions with brighter dot patterns represent La-enriched phases attached to the lattice of the support, which can be seen well due to the element's high atom weight which can create high STEM-HAADF contrast.

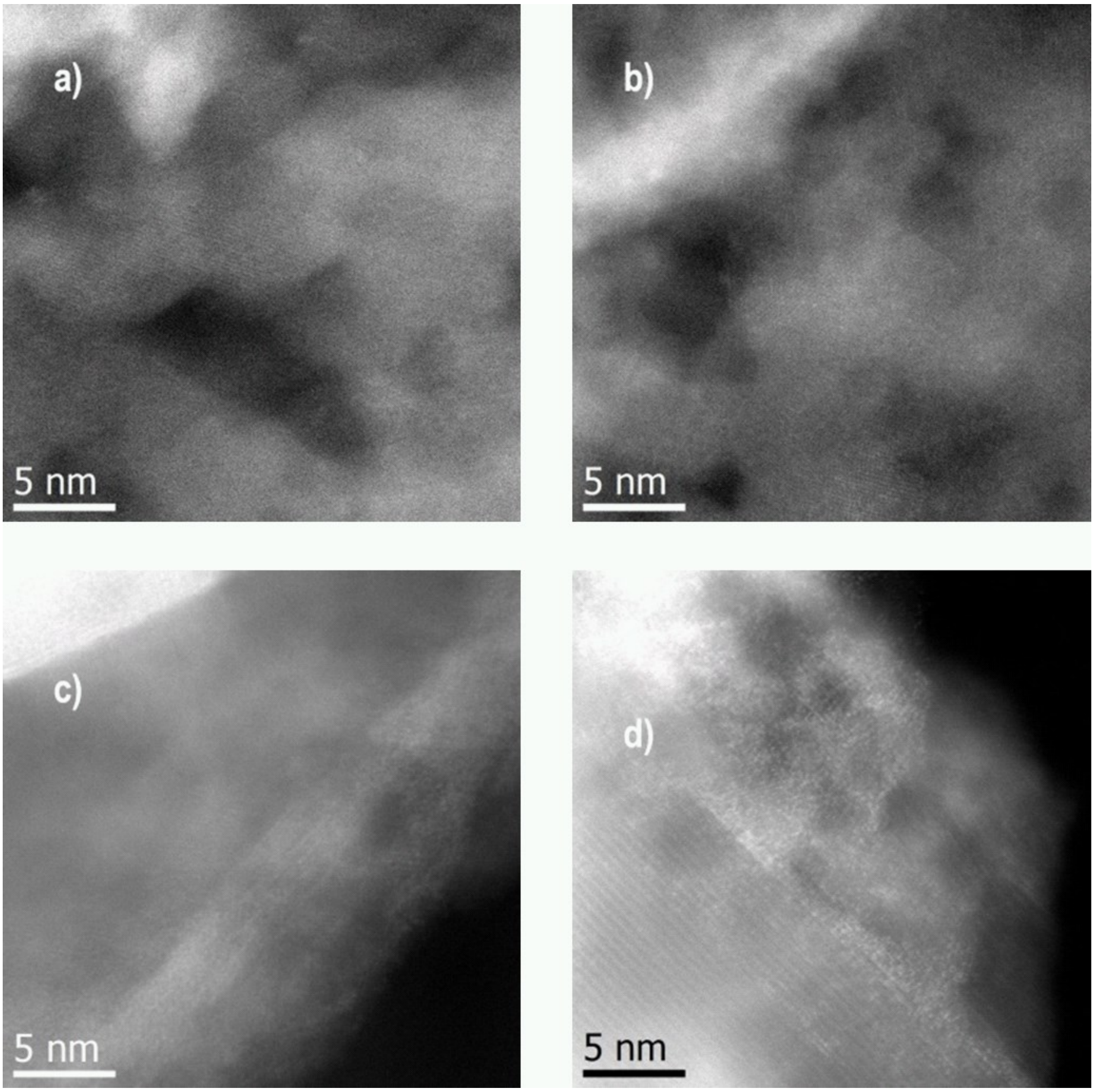

Figure 5.4. STEM images of fresh calcined Ni catalysts: a) Ni/$Mg_{1.3}AlO_x$, b) Ni(CA)/$Mg_{1.3}AlO_x$, c) La.Ni/$Mg_{1.3}AlO_x$ and d) La.Ni(CA)/$Mg_{1.3}AlO_x$.

The elemental mapping of the spent Ni catalysts was also implemented in order to examine the dispersion of Ni species after DRM. Figure 5.5 shows EDX elemental maps overlaid on their corresponding HAADF images of the various spent Ni catalysts on $Mg_{1.3}AlO_x$ after 8 hours on stream in DRM at 630 °C.

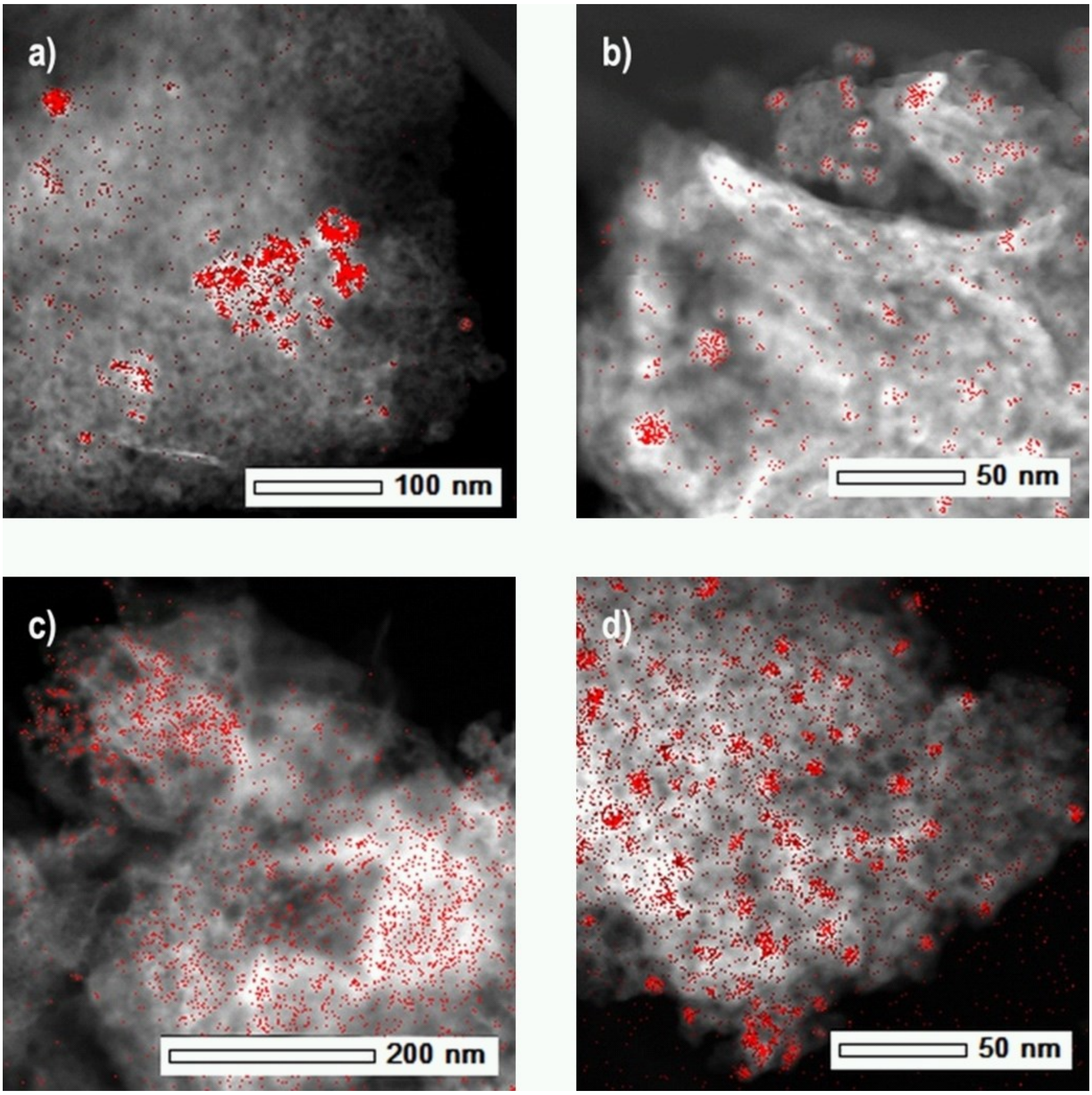

Figure 5.5. EDX elemental maps overlaid on STEM-HAADF images of spent Ni catalysts supported on $Mg_{1.3}AlO_x$: a) Ni/$Mg_{1.3}AlO_x$, b) Ni(CA)/$Mg_{1.3}AlO_x$, c) La.Ni/$Mg_{1.3}AlO_x$, d) La.Ni(CA)/$Mg_{1.3}AlO_x$. DRM conditions: 630 °C, 1 bar, 8 h, CH_4: CO_2 = 1, GHSV = 170 L/(g_{cat}×h). All the catalysts were in situ pre-reduced at 700 °C for 1.5 hours prior to the reaction.

Compared to the fresh calcined Ni/$Mg_{1.3}AlO_x$, the spent sample still shows dispersed Ni particles but also big Ni particles up to 30 nm have been generated by agglomeration (Figure 5.5a). This is a result of the thermal migration of smaller clusters moving across the support surface, resulting in the growth of active phase crystallites as well as the metal particle size [194]. Such agglomeration then reduces surface active site quantity, causing catalyst deactivation and coking in high-temperature reactions (> 500 °C). However, the Ni catalysts modified with La and/or CA during synthesis reveal a remarkable restriction of such Ni migration, proving a stabilizing effect preserving the dispersion of Ni particles during the reaction. This stabilization happens on Ni(CA)/$Mg_{1.3}AlO_x$ and La.Ni(CA)/$Mg_{1.3}AlO_x$ probably due to their high MSI (Figure 5.2) and better dispersion of Ni species in the fresh catalysts (Table 5.3 and Figure 5.3).

In order to understand the deactivation of such catalysts in DRM, two examples of agglomerated Ni particles in spent Ni/$Mg_{1.3}AlO_x$ (from the same test) were studied by STEM-EDX (Figure 5.6). Figure 5.6a shows the STEM annular bright field (ABF) image of a Ni particle of 20 nm size covered by a 10 nm thick graphitic carbon layer. This carbon accumulation was evidenced by EDX spectra at regions 025 and 022, showing different Ni/C ratios. The formation of carbon during DRM preferably on big metal particles was reported previously [3, 195]. Further carbon species then chemisorb or adsorb on the particle surfaces, grow and encapsulate the active sites, subsequently deactivating the catalyst [194].

In contrast, Figure 5.6b shows another Ni particle which is relatively smaller (approximately 5 nm) and covered by a thin and well-ordered layer. According to EDX spectra of region 001 and 002 in the same figure and also pointed out by lattice layer distance changes (from 0.20 nm in the core, indicating Ni (101), to 0.24 nm in the shell which denotes NiO (222)), the layer contains mostly nickel oxide (denoted as $NiO_{1-\delta}$), reflecting the partial re-oxidation of the metal. Similar behaviour was seen in Ni catalysts in other studies [50, 196-199]. They suggested that the presence of basic oxides, such as MgO, promotes the dissociative adsorption of CO_2 which benefits with the intent to oxidize the surface carbon formed from CH_4 decomposition (Eq. 7) and/or Boudouard reaction (Eq. 9). However, such basic components may also improve the oxygen affinity of Ni which then is more prone to be oxidized during the reaction [200]. It should be noted that CO_2 is a weak oxidant compared to H_2O or O_2 (as found in steam reforming or partial oxidation reactions), respectively. However, CO_2 could also partially oxidize Ni metal species into oxide containing mixtures (denoted as Ni/$NiO_{1-\delta}$) because such transformation is assisted by the subsequent favoured formation of certain stable structures of such Ni oxides and the support [201]. As a result, such transformation may cause gradual deactivation of Ni catalysts in DRM due to the lower activity of Ni/$NiO_{1-\delta}$ [200].

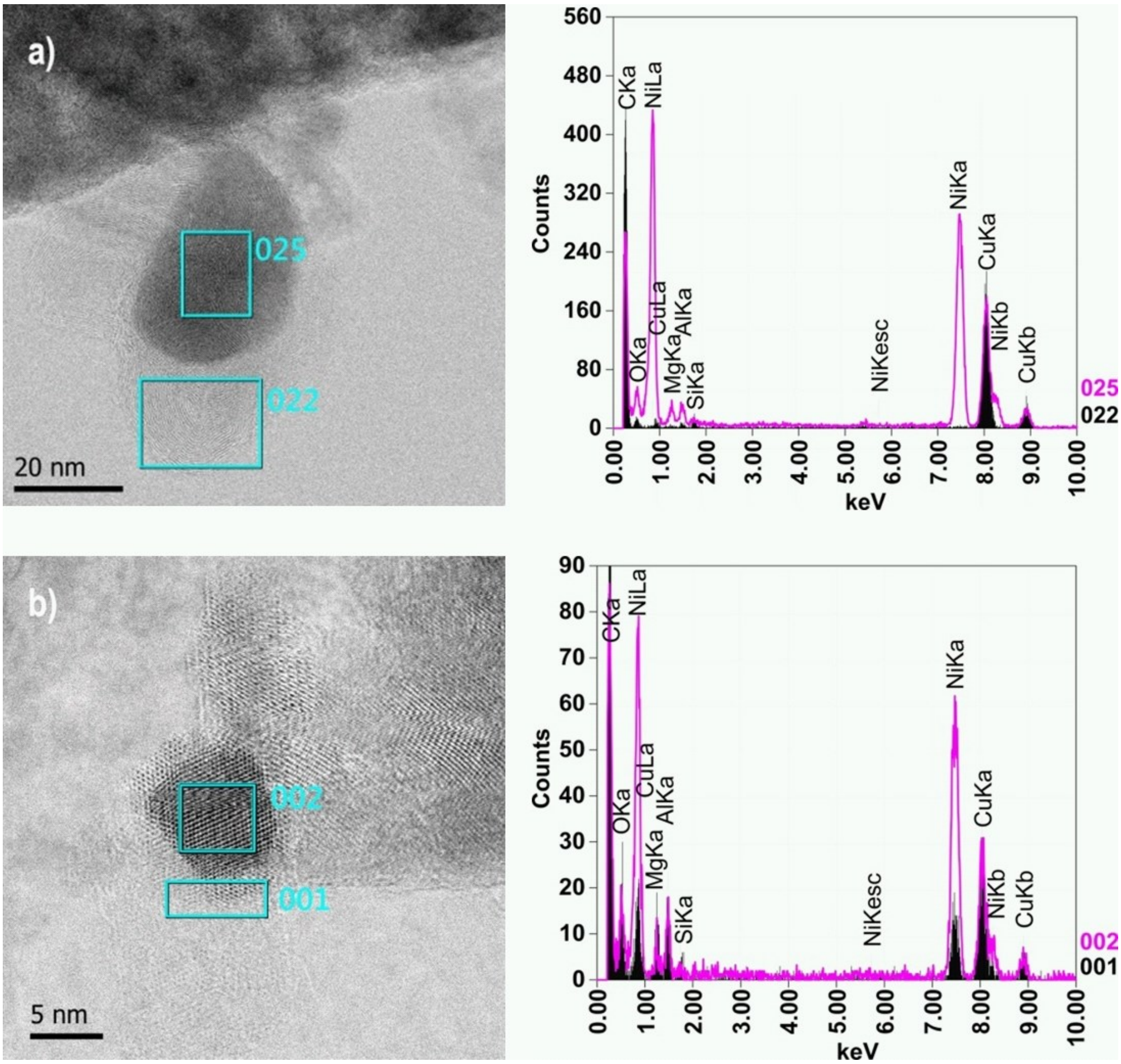

Figure 5.6. STEM-ABF images and their EDXS analyses of individual particles on spent Ni/$Mg_{1.3}AlO_x$ mainly covered by a) carbon and b) $NiO_{1-\delta}$.

Mentioned Ni/$NiO_{1-\delta}$ clusters were commonly found in STEM-HAADF images of all spent samples (Figure 5.7) with the particle sizes typically below 10 nm. Besides, while the Ni particle covered with carbon, as found in spent Ni/$Mg_{1.3}AlO_x$, is larger and loosely attached to the rest of the sample (Figure 5.6a), the Ni/$NiO_{1-\delta}$ clusters in all samples are merged partially to the bulk MgO-Al_2O_3. For fresh catalysts, UV-Vis measurement (Figure 5.3b) and STEM-EDX (Figure 5.4) confirmed that Ni species (in oxides) were confined by solution with the support via strong MSI. Ni particles agglomerated during DRM but partially re-oxidized at high partial pressure of oxidizing CO_2 would be limited in size due to such MSI with the stable support. This behaviour was also reported for other Ni catalyst systems [200, 202] that contain MgO in the support. Therefore, in this study all CA- or La-treated Ni catalysts with an apparent strong promotion of dissociative CO_2 adsorption [52, 56] might contribute to the stable dispersion of Ni species (Figure 5.5) and lower carbon deposition during DRM compared to that of Ni/Mg$_{1.3}$AlO$_x$ which will be illustrated below.

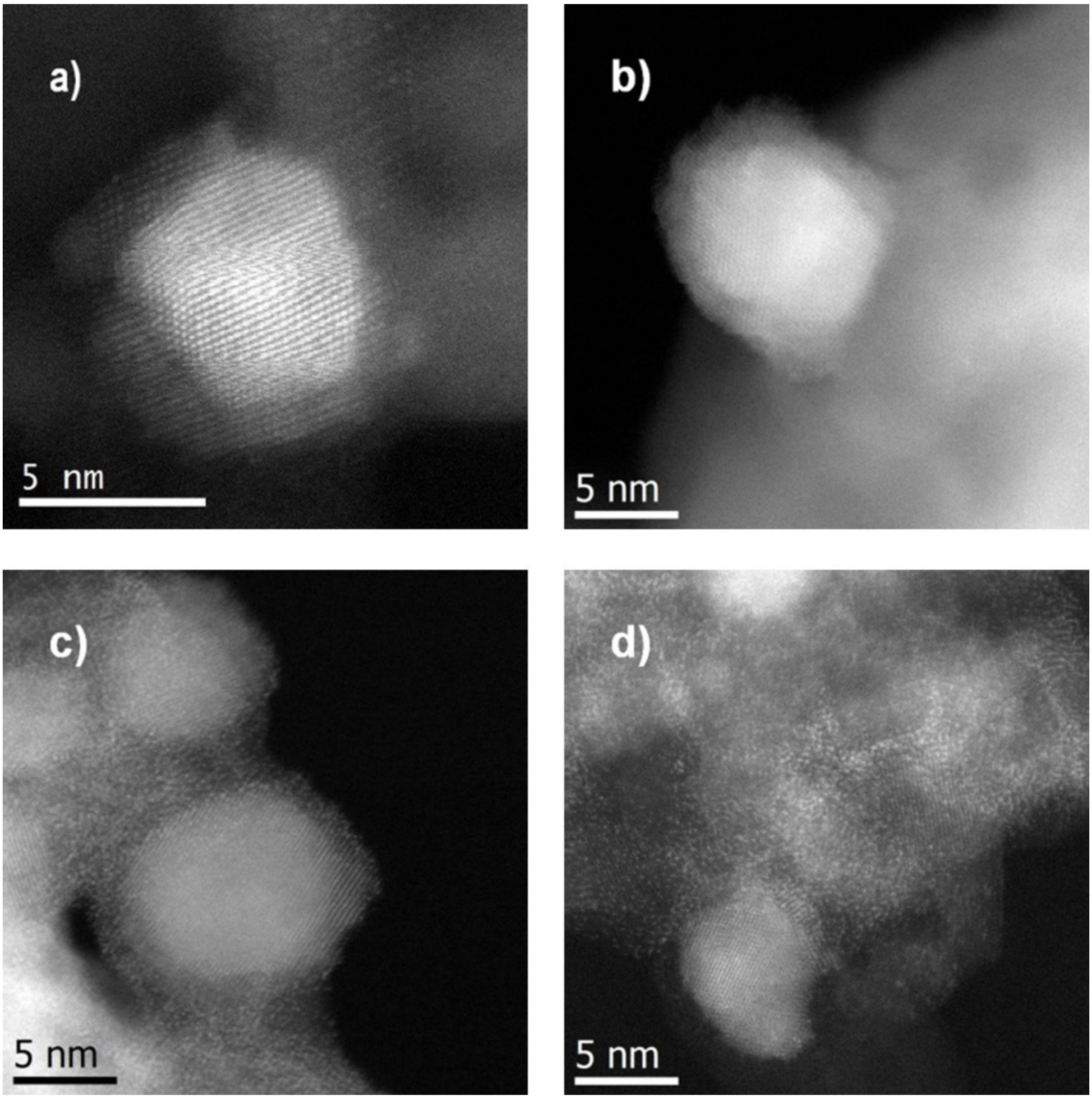

Figure 5.7. STEM-HAADF images of Ni particles covered by NiO in spent samples: a) Ni/Mg$_{1.3}$AlO$_x$, b) Ni(CA)/Mg$_{1.3}$AlO$_x$, c) La.Ni/Mg$_{1.3}$AlO$_x$, d) La.Ni(CA)/Mg$_{1.3}$AlO$_x$.

Remarkably, the La-containing samples still show the dispersion of La on the support (Figure 5.7c-d). Nevertheless, in the sample prepared without CA (Figure 5.7c), the heavier elements seem to locally migrate onto the surface of the Ni particles while the sample prepared with CA (Figure 5.7d) negligibly shows such behaviour. This is also in line with the elemental mapping of these two samples after catalyst calcination (Figure 5.8), wherein more homogeneous dispersion of both La and Ni atoms was obtained in La.Ni(CA)/Mg$_{1.3}$AlO$_x$. This difference again confirms the effect of CA in dispersion and stabilization of both La and Ni species during the reactions.

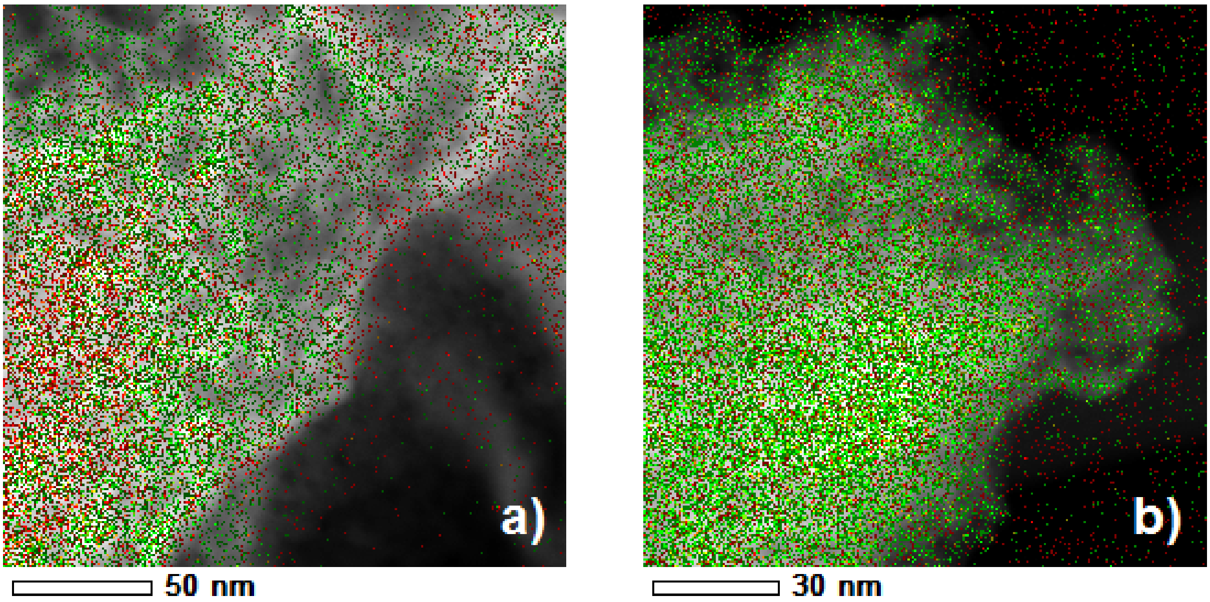

Figure 5.8. EDX elemental map overlaid on STEM-HAADF images of a) La.Ni/$Mg_{1.3}AlO_x$, b) La.Ni(CA)/$Mg_{1.3}AlO_x$. Green dots: La, Red dots: Ni.

An additional DRM test at 630 °C was conducted on La.Ni(CA)/Al_2O_3 (Figure 5.9) to study the stability of MgO-free catalyst prepared via this beneficial modification route as applied to Ni/$Mg_{1.3}AlO_x$. Similar to other $Mg_{1.3}AlO_x$ supported samples, La.Ni(CA)/Al_2O_3 after catalyst calcination exposes high dispersion of La and Ni. However, the spent sample of this catalyst recovered after 8 hours on stream shows a severe agglomeration of Ni atoms, leading to the formation of big Ni particles with the size up to 20 nm. This behaviour is seen in contrast with the result obtained from the same test with La.Ni(CA)/$Mg_{1.3}AlO_x$, which preserved the Ni distribution during the reaction (Figure 5.5d). In chapter 4, a similar comparison was also implemented between Ni/$Mg_{1.3}AlO_x$ and Ni/Al_2O_3, which pointed out the effect of MgO in catalyst stabilization. Therefore, it is suggested that the enhancement in catalyst stabilization by La and CA-based synthesis was not achievable with La.Ni(CA)/Al_2O_3. This observation may relate to the mentioned formation of solid solutions of re-oxidized Ni species with the supports in MgO-containing catalysts during the reaction. This formation was seen enhanced for the catalyst with both modifications during preparation, thus limiting the size of Ni particles in DRM (Figure 5.7).

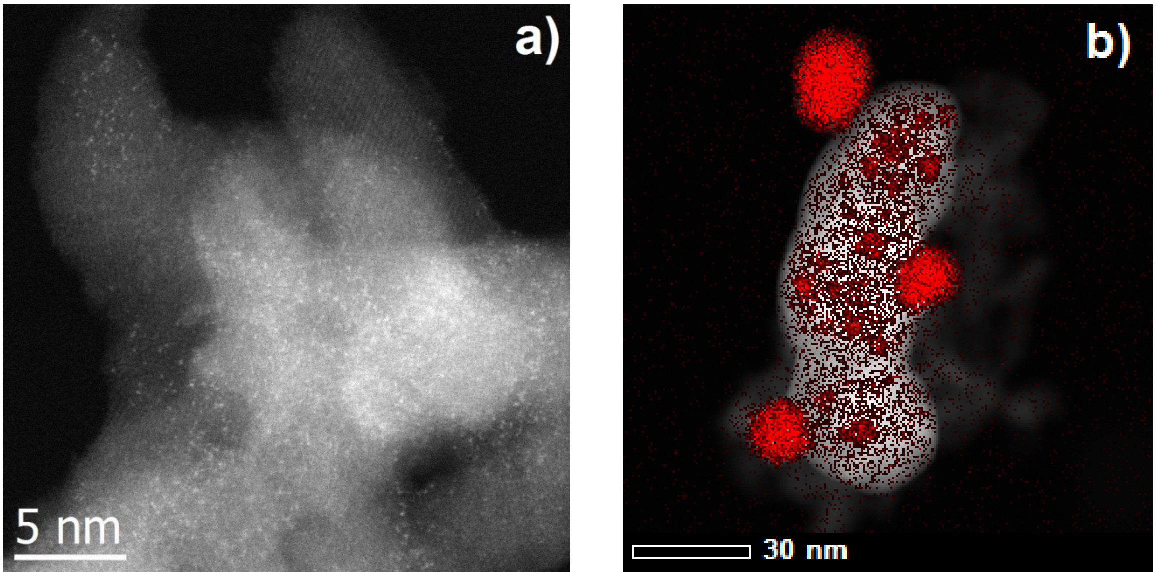

Figure 5.9. a) STEM images of fresh and b) EDX elemental map overlaid on STEM-HAADF images of spent La.Ni(CA)/Al_2O_3. DRM conditions: 630 °C, 1 bar, 8 h, CH_4: CO_2 = 1, GHSV = 170 L/(g_{cat}×h). Catalyst was in situ pre-reduced at 700 °C for 1.5 hours prior to the reaction.

5.2 Performance of La and/or CA treated Ni catalysts in DRM at 630 °C

The DRM tests were conducted at low temperature (630 °C) and high space velocity (170 L/(g_{cat}×h)) on Ni catalysts in order to differentiate the catalyst activities and to observe the carbon formation from both side reactions, methane cracking (Eq. 7) and Boudouard reaction (Eq. 9) [50]. The CH_4 and CO_2 conversions are presented in Figure 5.10 and are all stable after a short equilibration stage during 8 h on stream. Among the catalysts, Ni/$Mg_{1.3}AlO_x$ exhibits the highest activity with the conversions of CH_4 and CO_2 reaching 50% and 60%, respectively, close to the thermodynamic limits at set reaction temperature [50]. The Ni catalysts with CA-based synthesis show slightly lower conversions which are probably due to their higher MSI, as confirmed by TPR (Figure 5.2), lessening the Ni^{2+} reducibility in H_2 atmosphere.

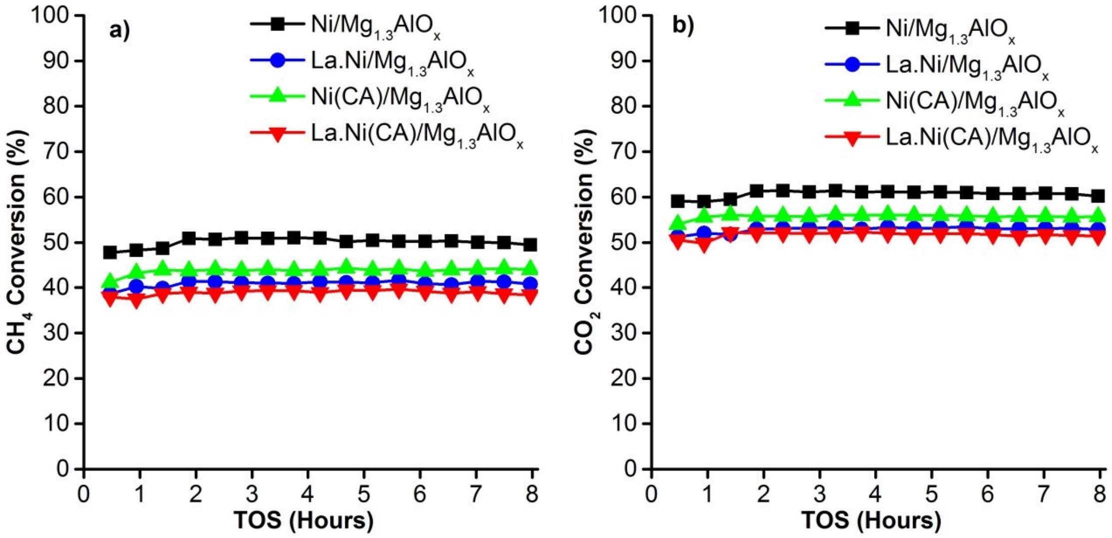

Figure 5.10. Conversions of a) CH_4 and b) CO_2 in DRM on $Mg_{1.3}AlO_x$ supported Ni catalysts (630 °C, 1 bar, $CH_4/CO_2 = 1$, GHSV = 170 L/(g_{cat}×h)). All the catalysts were pre-reduced in situ at 700 °C for 1.5 hours prior to the reaction.

The H_2/CO ratios in DRM with all samples are lower than 1 (Figure 5.11a), revealing the strong influence of reverse water gas shift reaction (Eq. 5) at low reaction temperature, decreasing H_2 selectivity and forming H_2O as a side product. Besides, while all catalysts disclose comparable activity in DRM, the coking rates are significantly different. Indeed, CH elemental analyses of the spent samples of La and/or CA-assisted synthesis modified catalysts, collected after 8 hours on stream, demonstrate the remarkable suppression of carbon formation compared to that of Ni/$Mg_{1.3}AlO_x$ (Figure 5.11b). The reactions with CH_4/Ar (without CO_2) and same GHSV on these Ni catalysts were also conducted to study the source of deposited carbon (Figure 5.11b). Therein, all catalysts expose low coking rate, reflecting the slow methane cracking reaction at the chosen temperature, probably due to the small size of Ni particles attributing to low Ni content (Figure 5.4) and/or thermodynamic limit. However, lower carbon deposition has been achieved on Ni(CA)/$Mg_{1.3}AlO_x$ and La.Ni(CA)/$Mg_{1.3}AlO_x$, which also present better coking resistance in DRM ($CH_4/CO_2 = 1$). These excellent results confirm the positive influence of the stable dispersion of Ni atoms obtained in both Ni(CA)/$Mg_{1.3}AlO_x$ and La.Ni(CA)/$Mg_{1.3}AlO_x$ during DRM, as observed in EDX elemental maps of their corresponding spent catalysts (Figure 5.5). Therefore, it can be suggested that the CA-assisted preparation generated finely dispersed Ni species which strongly interact with the Mg-Al supports, as proven by TPR (Figure 5.2) and UV-Vis (Figure 5.3), and are less prone to the agglomeration during the reaction. Interestingly, although La.Ni/$Mg_{1.3}AlO_x$ shows less homogeneous Ni dispersion (Figure 5.8), weak MSI and does not enhance coking resistance in methane cracking reaction (Figure 5.11b), it still exhibits the lowest carbon deposition (Figure 5.11b) and limited agglomeration (Figure 5.5) during DRM. That result points out the potential of CO_2 in surface carbon removal and $Ni/NiO_{1-\delta}$ formation that might limit both coking rate and the size of Ni particles.

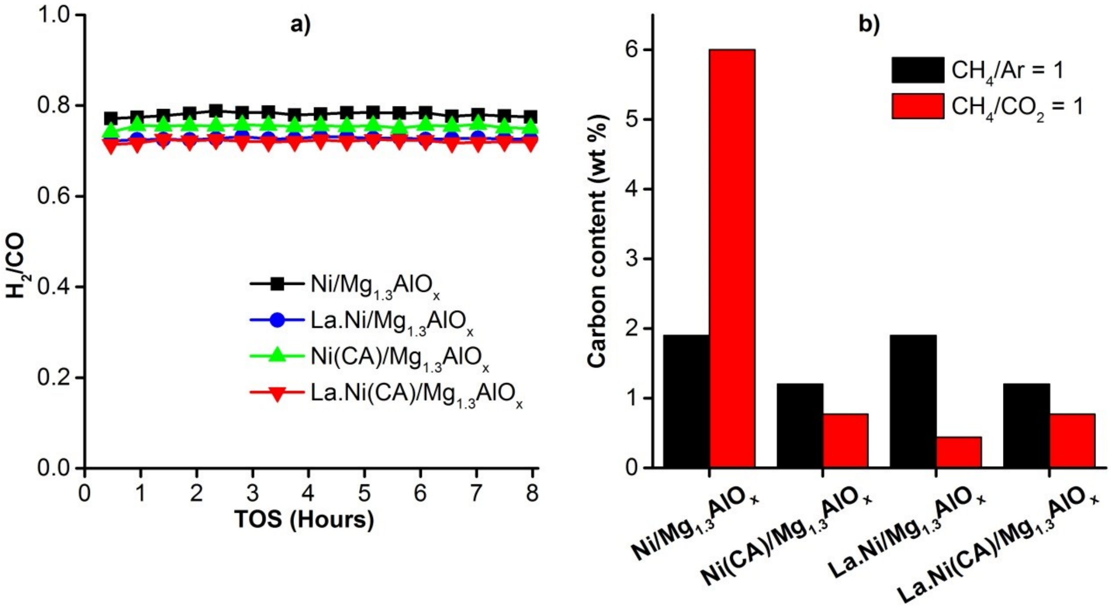

Figure 5.11. DRM performance of $Mg_{1.3}AlO_x$ supported Ni catalysts with a) H_2/CO ratio and b) fraction of carbon deposits on spent catalysts after DRM (630 °C, 1 bar, CH_4/CO_2 or $CH_4/Ar = 1$, GHSV = 170 L/(g_{cat}×h), TOS = 8 hours). All the catalysts were pre-reduced in situ at 700 °C for 1.5 hours prior to the reaction.

5.3 Long-term stability testing and benchmarking

Long-term stability tests were implemented at severe conditions, i.e., high temperature (750 °C) and high space velocity (170 L/(g_{cat}×h)) in order to study the deactivation of the catalysts. Such reaction conditions were also chosen to target a higher specific production of syngas that could meet industry needs. Figure 5.12 shows CH_4 and CO_2 conversions with all Ni catalysts in DRM over 160 hours on stream. Although carbon amount was negligible (< 1.5 wt%) in all spent samples, deactivation was observed for all samples with different degrees. Therefore, together with the Ni agglomeration most likely happening to $Ni/Mg_{1.3}AlO_x$, the partial re-oxidation of the active atoms during DRM can be suggested as another deactivation pathway. Indeed, at the chosen reaction temperature (750 °C), the gasification by dissociatively adsorbed CO_2 (reverse Boudouard reaction) is thermodynamically favoured [2, 50]. This oxidation reaction not only affects the carbon species but also Ni metal sites, forming $Ni/NiO_{1-\delta}$, as observed in STEM characterization (Figure 5.6b and Figure 5.7). Among the catalysts, $La.Ni(CA)/Mg_{1.3}AlO_x$ is likely least affected by such oxidation and excellently maintains high and stable reactivity during 160 h on stream. Although both $La.Ni(CA)/Mg_{1.3}AlO_x$ and $Ni(CA)/Mg_{1.3}AlO_x$ disclose stable dispersion of Ni during

DRM (Figure 5.5d and b), the former sample benefits from its good reducibility, evidenced by a low-temperature reduction peak (Figure 5.2) and remarkably higher H_2 consumption in TPR (Table 5.2). That advantage might make the Ni species in La.Ni(CA)/$Mg_{1.3}AlO_x$ more reactive with not only H_2 in pre-reduction step but also CO/H_2 during the reaction and thus more stable against re-oxidation. Additionally, compared to La.Ni(CA)/$Mg_{1.3}AlO_x$, La.Ni/$Mg_{1.3}AlO_x$ shows a higher amount of defective species (Figure 5.3) containing oxygen vacancies, which affect the electron density and oxygen affinity of the Ni atoms [200, 203]. Therefore, Ni species in La.Ni/$Mg_{1.3}AlO_x$ are more sensitive to oxidation by dissociative CO_2 adsorption, leading to faster catalyst deactivation.

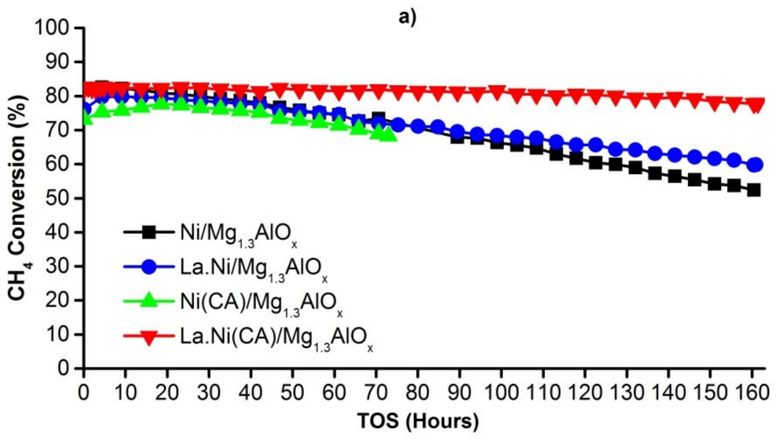

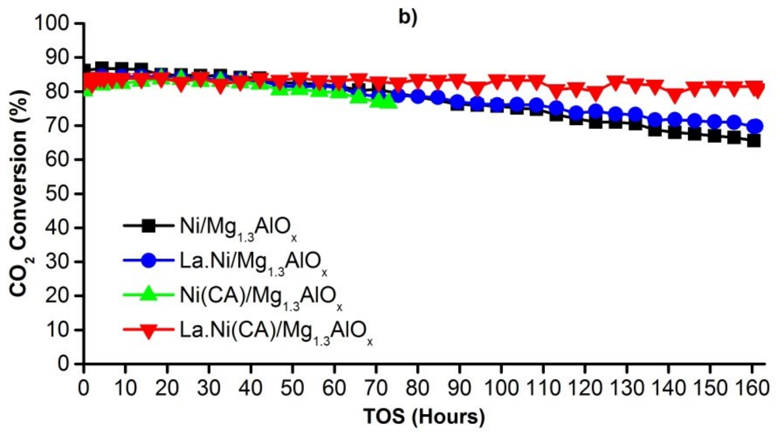

Figure 5.12. Conversions of a) CH_4 and b) CO_2 in long-term DRM on $Mg_{1.3}AlO_x$ supported Ni catalysts (750 °C, 1 bar, $CH_4/CO_2 = 1$, GHSV = 170 L/(g_{cat}×h)). All the catalysts were in situ pre-reduced at 700 °C for 1 hour prior to the reaction.

The performance of the best catalyst described in this chapter, La.Ni(CA)/$Mg_{1.3}AlO_x$, was outstanding compared to Ni-based catalysts from recent studies [66, 71]. According to the database, very few studies applied Ni contents below 5 wt%. Among those investigations with low Ni content, only a few employed comparable high space velocity [101, 113, 120, 204]. However, most of these studies show low

H_2 productivities due to the low conversion of reactants or diluted CH_4/CO_2 in the feedstock. There is reported a catalyst system with high Ni content (15 wt%) [120] that demonstrated highest H_2 productivity (178 L/(g_{cat}×h)) at 800 °C, which is slightly higher than that in this study (118 L/(g_{cat}×h)). However, considering the fraction of cost-driving Ni and reaction temperature, the catalyst productivity in the present study is superior. Other studies [112, 120, 205] also exposed remarkably stable DRM up to 200 hours on stream without significant catalyst deactivation. Outstandingly, Fan et al. [112] were successful with 1000 hours of DRM with only 13% loss of activity compared to 3% after 160 hours in the present study. However, the higher Ni content (16.4 wt%) and lower GHSV (60 L/(g_{cat}×h)) indicate that stability was preserved at the cost of productivity per Ni atom.

5.4 Intermediate conclusion from chapter 5

Applying La and/or CA-based modification during the preparation of Ni catalysts results in improved coking resistance while still maintaining the high activity comparable to $Ni/Mg_{1.3}AlO_x$. Such modifications lead to significantly lower coking rate in DRM, especially at low temperature due to enhanced MSI and/or CO_2 activation which help to stabilize the Ni species and remove surface carbon during the reactions. However, CO_2 activation could show negative impact at high temperature by causing Ni re-oxidation resulting in gradual loss of conversion. Such behaviour causes catalyst deactivation, but in contrast, it may offer benefit in governing the Ni particles size by partially stabilizing the as-formed oxides on the support during the DRM with high CO_2 partial pressure.

$La.Ni(CA)/Mg_{1.3}AlO_x$ exposes not only less coking at low reaction temperature (630 °C) but also high and stable activity at high temperature (750 °C) and high space velocity (170 L/(g_{cat}×h)). This best performance is the result of the balance between Ni dispersion and reducibility that brings strong MSI, preventing Ni agglomeration and carbon deposition but still making this catalyst less sensitive to oxidation by CO_2. Remarkably, such low Ni content catalyst presents high and stable DRM activity at same condition over 160 h on stream.

The effect of Ni re-oxidation and carbon gasification, both induced by CO_2 activation during DRM, presumably depends on the partial pressure of CO_2 in the reactant mixture. Therefore, DRM of the mixture of CH_4 and CO_2 with different ratios should be studied to indicate different coking resistance pathways. Besides, such investigation would be useful because there are particular CH_4/CO_2 ratios that imitate biogas and natural gas sources mentioned in section 1.1.

6 Performance of low Ni content catalysts in CH_4-rich DRM

As mentioned above in section 1.1, DRM can be considered to directly process CH_4 gas sources containing a significant but under-stoichiometric concentration of CO_2. In this chapter, the feedstock with CH_4:CO_2 molar ratio of 2 (CH_4-rich DRM) was used in order to imitate the natural gas and biogas sources that contain up to 30 vol% of CO_2. As a result, such CH_4-rich DRM offers the opportunity to obtain a higher H_2 selectivity but encounters high coking rate due to lack of CO_2 which is the oxidant for the surface carbon removal via gasification during the reaction.

In chapter 5, La.Ni(CA)/$Mg_{1.3}AlO_x$ was described to be the most active and stable catalyst in stoichiometric DRM. Compared to other catalysts in the same chapter, this material was suggested to be less affected by Ni re-oxidation occurring at higher reaction temperature and partial pressure of CO_2. In this chapter, the performance of these Ni catalysts in CH_4-rich DRM will be evaluated in order to determine their potential in conversion of mentioned gases and verify the contribution of CO_2 in metal re-oxidation during the reaction [181].

Also for the purpose of determining the stable Ni catalysts in CH_4-rich DRM, further catalyst modifications and $Mg_{1.3}AlO_x$ pre-treatments were applied.

By applying various feed compositions and reaction temperatures, the coking mechanism was studied. As a result, different catalyst modification effects were indicated and evaluated with regard to coking resistance.

6.1 Catalyst characterization

Figure 6.1 represents the XRD patterns of $Mg_{1.3}AlO_x$.1000 and the corresponding catalysts. The magnification of XRD patterns in the 2θ range from 61° to 64° of these samples is also illustrated. The support $Mg_{1.3}AlO_x$.1000, prepared by thermally pre-treating $Mg_{1.3}AlO_x$ at 1000 °C, shows the sharp and characteristic reflections of periclase MgO and $MgAl_2O_4$ crystalline phases. XRD results of Ni/$Mg_{1.3}AlO_x$.1000 and La.Ni(CA)/$Mg_{1.3}AlO_x$.1000 display patterns similar to the $Mg_{1.3}AlO_x$.1000 as their support material, suggesting the formation of finely dispersed La^{3+} and Ni^{2+} species heading to very small particles that were not noticed by the XRD measurements [160]. However, these Ni catalysts also expose a slight shift at 62.2° to higher 2θ values compared to that of their corresponding support, suggesting the NiO-MgO solid solution structure formation (Figure 6.1).

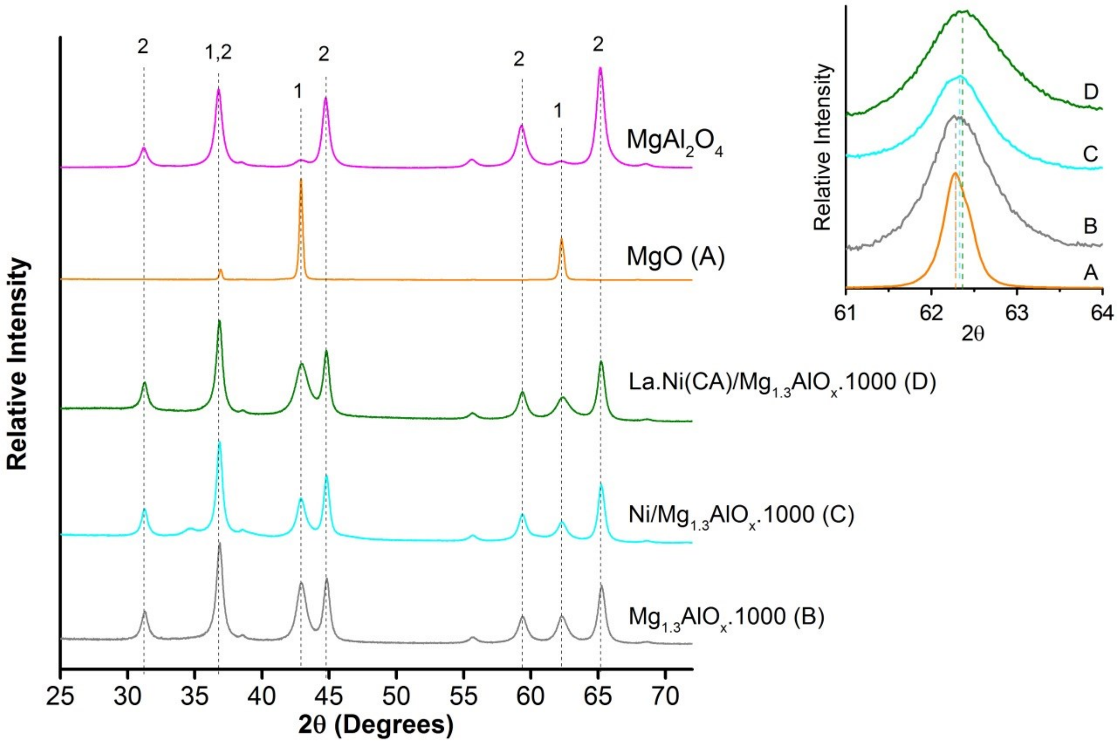

Figure 6.1. XRD patterns of references ($MgAl_2O_4$, MgO), $Mg_{1.3}AlO_x$.1000 and the corresponding supported Ni catalysts. Crystalline phases: periclase (MgO) (1), $MgAl_2O_4$ (2).

The textural parameters of $Mg_{1.3}AlO_x$.1000 and the corresponding catalysts are summarized in Table 6.1. Compared to $Mg_{1.3}AlO_x$.1000, Ni/$Mg_{1.3}AlO_x$.1000 shows similar values whereas La.Ni(CA)/$Mg_{1.3}AlO_x$.1000 has lower BET surface area and pore volume due to the increased surface coverage by La species. Besides, it should be noted that these $Mg_{1.3}AlO_x$.1000 supported catalysts expose significantly lower values of the textural parameters compared to those of $Mg_{1.3}AlO_x$-derived materials. Compared to the molecule size of the reactants, the catalysts pore sizes are significantly larger, probably increasing internal diffusion during DRM.

Table 6.1. Textural properties of $Mg_{1.3}AlO_x$.1000 and its catalysts

Catalyst	S_{BET} (m^2/g)	Total pore volume (cm^3/g)	Average Pore Diameter (Å)
$Mg_{1.3}AlO_x$.1000	85	0.37	118
Ni/$Mg_{1.3}AlO_x$.1000	82	0.36	126
La.Ni(CA)/$Mg_{1.3}AlO_x$.1000	80	0.25	97

TPR measurements with Ni catalysts supported on different supports were conducted and data are shown in Figure 6.2 and Table 6.2. Ni/$Mg_{1.3}AlO_x$.1000 discloses poorer reducibility compared to Ni/$Mg_{1.3}AlO_x$ which was discussed before in chapter 4. Compared to the H_2 consumption of La.Ni(CA)/$Mg_{1.3}AlO_x$ (521 µmol/g), La.Ni(CA)/$Mg_{1.3}AlO_x$.1000 exhibits lower value (493 µmol/g) but higher than that of Ni/$Mg_{1.3}AlO_x$.1000 (404 µmol/g) and also higher than the theoretical value for complete Ni^{2+} reduction to metal. TPR profile of La.Ni(CA)/$Mg_{1.3}AlO_x$.1000 reveals different reduction peak maxima at various temperatures.

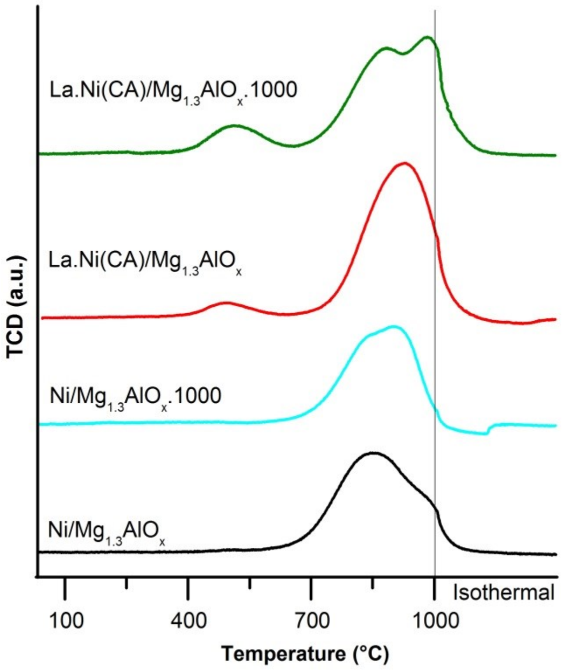

Figure 6.2. TPR profiles of Ni catalysts supported on $Mg_{1.3}AlO_x$.1000 and $Mg_{1.3}AlO_x$.

Similar to La.Ni(CA)/$Mg_{1.3}AlO_x$, La.Ni(CA)/$Mg_{1.3}AlO_x$.1000 exposes a low-temperature reduction peak below 550 °C but with higher intensity. On the other side, La.Ni(CA)/$Mg_{1.3}AlO_x$.1000 shows a splitted main reduction peak with a first maximum at 885 °C which is seen at a somewhat lower temperature than the maxima of La.Ni(CA)/$Mg_{1.3}AlO_x$ (930 °C) and Ni/$Mg_{1.3}AlO_x$.1000 (900 °C). These features of La.Ni(CA)/$Mg_{1.3}AlO_x$.1000 again confirm the benefit of La incorporation on Ni catalysts' reducibility. The second reduction peak at 980 °C found in La.Ni(CA)/$Mg_{1.3}AlO_x$.1000 probably can be assigned to highly dispersed Ni species that have a stronger MSI.

Table 6.2. H_2 consumption (TPR) and La, Ni contents (ICP) of Ni catalysts and their support.

Sample	H_2 consumption (µmol/g)	Ni content (wt%)	La content (wt%)
Catalysts and support			
Ni/$Mg_{1.3}AlO_x$.1000	404	2.40	-
La.Ni(CA)/$Mg_{1.3}AlO_x$.1000	493	2.13	4.10
$Mg_{1.3}AlO_x$.1000	32	-	-
Theoretical H_2 uptake for $Ni^{2+} \rightarrow Ni^0$ of 2.5 wt% Ni sample	428	-	-

The UV-Vis DR spectra in the region of 200-350 nm for these catalysts (Figure 6.3a) give some hints on the Ni dispersity via the appearance of their Ni^{2+} LMCT bands. La.Ni(CA)/$Mg_{1.3}AlO_x$.1000 displays the LMCT band with weaker intensity and/or blue shift compared to that of Ni/$Mg_{1.3}AlO_x$.1000, indicating a higher degree of Ni dispersion which is most likely due to the CA-based synthesis. This behaviour confirms the formation of poorly reducible species in La.Ni(CA)/$Mg_{1.3}AlO_x$.1000 (Figure 6.2). However, this catalyst still has benefits in reducibility, especially in terms of higher H_2 consumption than that of Ni/$Mg_{1.3}AlO_x$.1000 (Table 6.2). This relation might depict the existence of certain unusual oxidation states and structures of Ni^{m+} ($m > 2$) which can be confirmed by studying the UV-Vis spectrum of the sample in the visible region.

The UV-Vis spectrum of La.Ni(CA)/$Mg_{1.3}AlO_x$.1000 in the region 350-800 nm is compared with that of Ni/$Mg_{1.3}AlO_x$.1000 and the corresponding $Mg_{1.3}AlO_x$ supported Ni catalysts (Figure 6.3b). No Ni^{2+} (Th) species mainly in $NiAl_2O_4$ spinel were found in all four samples. The absence of such Ni^{2+} (Th) species in $Mg_{1.3}AlO_x$.1000 supported samples reflects the lack of Al^{3+} ions which were already in the stable $MgAl_2O_4$ structure with surplus Mg^{2+} [166], confirmed by XRD (Figure 6.1), leaving Ni^{2+} in the octahedral coordination in the solid solution with MgO.

In the UV-Vis spectrum of Ni/$Mg_{1.3}AlO_x$ there are two absorption bands at 400 nm and 660 nm (Figure 6.3b) which were also found for La.Ni(CA)/$Mg_{1.3}AlO_x$ with a similar appearance. Ni/$Mg_{1.3}AlO_x$.1000 also reveals the bands at these two regions. However, La.Ni(CA)/$Mg_{1.3}AlO_x$.1000 shows only a strong band at 400 nm with a broad absorption range ending at 600 nm, which is quite similar to that of La.Ni(CA)/MgO. Additionally, XRD patterns of La.Ni(CA)/$Mg_{1.3}AlO_x$.1000 reveals the crystalline structure of periclase (MgO) (Figure 6.1). Therefore, similar to La.Ni(CA)/MgO, La.Ni(CA)/$Mg_{1.3}AlO_x$.1000 can be suggested to be influenced by unusual structures of MgO in periclase support doped with Ni^{2+} which are responsible for the benefits in the reducibility of the sample compared to that of

$Ni/Mg_{1.3}AlO_x$.1000 (Figure 6.2 and Table 6.2). However, the shoulder at 450-600 nm, as seen in Ni/MgO, correlated with Ni^{2+} species in the local defect/distorted structures (chapter 5), was less intensive/blue shifted in the UV-Vis plot of La.Ni(CA)/$Mg_{1.3}AlO_x$.1000.

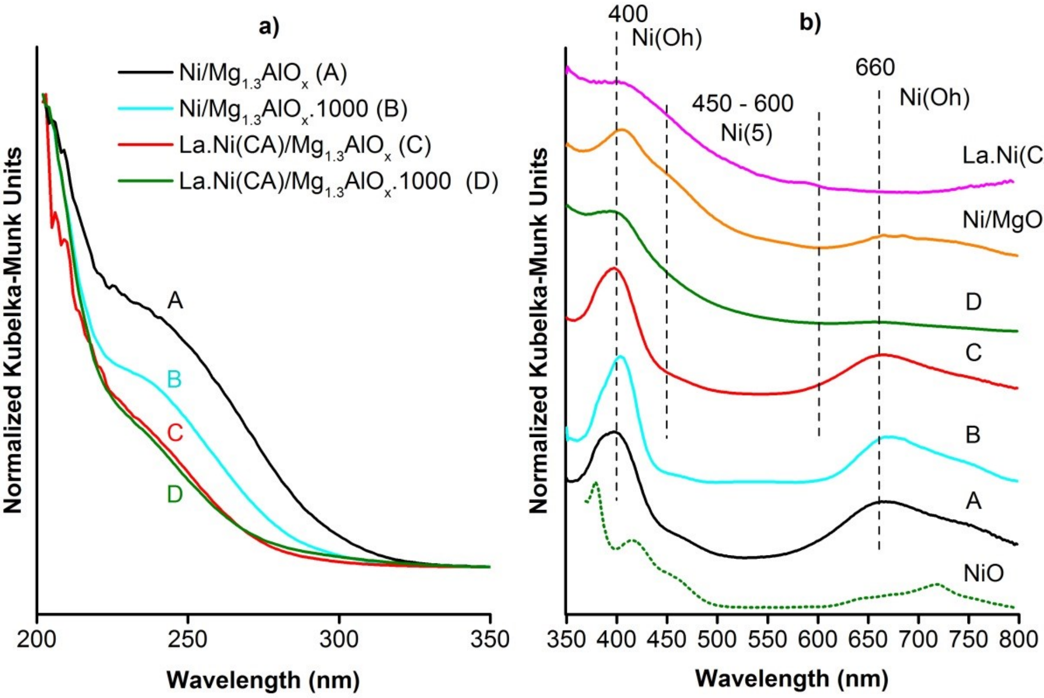

Figure 6.3. UV-Vis-DR spectra in the region a) 200-350 nm and b) 350-800 nm of $Mg_{1.3}AlO_x$.1000 supported Ni catalysts and $Ni/Mg_{1.3}AlO_x$ and La.Ni(CA)/$Mg_{1.3}AlO_x$. Ni(Oh): Ni species in octahedral coordination; Ni(5): Ni species in surface fivefold coordination.

6.2 Carbon formation pathways in DRM

The coking mechanism was studied by determining the amount of carbon deposits on $Ni/Mg_{1.3}AlO_x$ after 8 hours on stream in DRM at different reaction temperatures (500-750 °C) at same GHSV of 170L/(g_{cat}×h) using feeds composed of CH_4/Ar = 1 or 2 (both without CO_2) as well as CH_4/CO_2 = 1 or 2 (Figure 6.4). Generally, carbon formation in DRM is the result of two reactions: methane decomposition (Eq. 7) above 550 °C and Boudouard reaction (Eq. 9) below 700 °C [50].

At 500 °C, the carbon contents on all the spent catalysts are negligible. The higher reaction temperature and concentration of CH_4 cause higher carbon deposition in all tests with CH_4/Ar, reflecting the impact of MD reaction and/or intensive metal agglomeration which are both enhanced at high temperature [60, 194]. At both reaction temperatures of 630 °C and 750 °C, the carbon deposition negligibly changed when CH_4/Ar ratio was varied. However, when CO_2 was converted in DRM at 630 °C with CH_4 at any portion, such deposition was significantly higher, reflecting the main contribution of BD via CO formed during reaction outnumbering that of MD. However, at 750 °C, the contribution of BD is decreased. Indeed, when Ar is replaced with CO_2, the carbon amount insignificantly changes in case of $CH_4/CO_2 = 2$ and dramatically decreases in case of $CH_4/CO_2 = 1$, adapting to the fact that the BD is thermodynamically unfavorable at high temperature [60]. In these two cases with different CH_4/CO_2 ratios, carbon deposition in DRM with stoichiometric CH_4/CO_2 ratio is low, reflecting the carbon gasification by CO_2 (reversed reaction of BD) which is favorable at higher temperature (750 °C) and concentration of CO_2 (50 vol%). This behavior probably is attributed to the presence of MgO as basic element in the catalyst that promotes the gasification of carbon species originating from MD reaction [60].

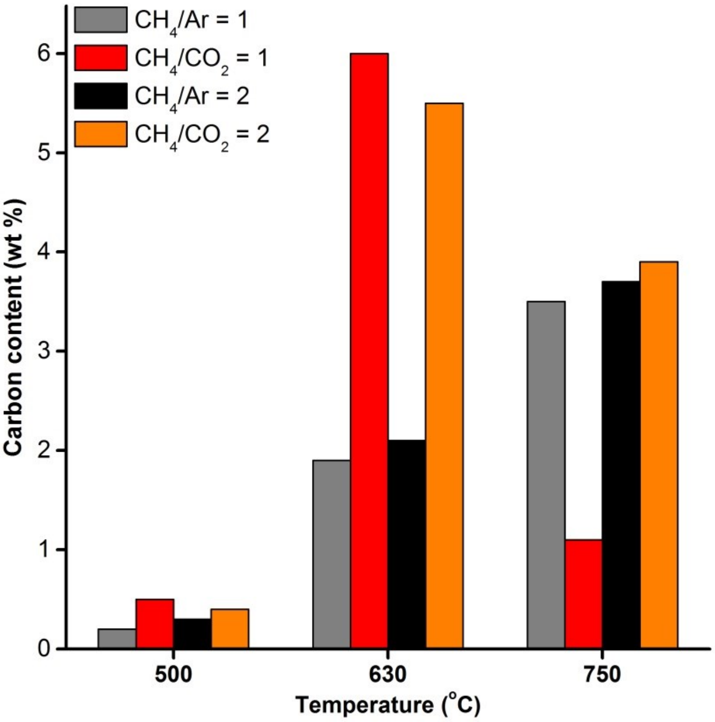

Figure 6.4. Carbon deposition on spent $Ni/Mg_{1.3}AlO_x$ after reactions with CH_4/CO_2 or CH_4/Ar with molar ratio of 1 or 2 (fixed GHSV = 170 L/(g_{cat}·h)) at different reaction temperatures. The catalysts were pre-reduced in situ at 700 °C for 1.5 hours prior to the reaction.

The predominant contribution of BD reaction in coke formation in DRM at 630 °C on $Ni/Mg_{1.3}AlO_x$ was further clarified with additional runs at other CH_4/CO_2 ratios (Figure 6.5). It can be seen that the carbon formation proportionally varied to the amount of CO formation during the reactions. These observations indicate that the carbon deposition on $Ni/Mg_{1.3}AlO_x$ in DRM at 630 °C is mainly initiated from BD reaction, in which CO is transformed into C. Indeed, regarding the thermodynamics of these two reactions [60], the Boudouard reaction is favorable at the chosen temperature (630 °C) over the CH_4 decomposition. In contrast, when DRM with $CH_4/CO_2 = 0.5$ was carried out (Figure 6.5), the carbon content had significantly lowered, reflecting the contribution of the gasification in response to the high partial pressure of CO_2.

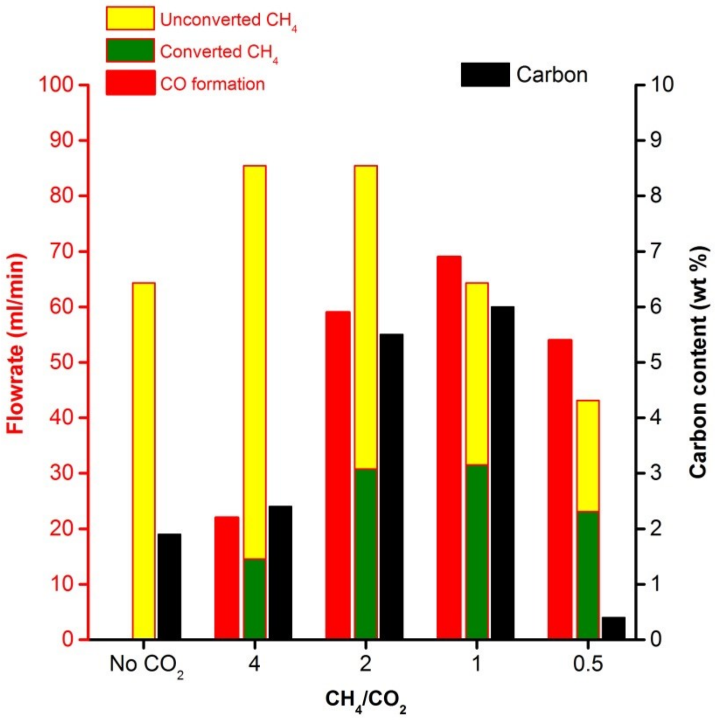

Figure 6.5. Performance of Ni/$Mg_{1.3}AlO_x$ with different feed compositions (fixed T = 630 °C). The catalysts were pre-reduced in situ at 700 °C for 1.5 hours prior to the reaction.

6.3 $Mg_{1.3}AlO_x$ supported catalysts in CH_4-rich DRM

Figure 6.6 and Figure 6.7 present the performances of $Mg_{1.3}AlO_x$ supported Ni catalysts in DRM with CH_4/CO_2 = 2 at different temperatures (630 °C and 750 °C) and high space velocity (170 L/(g_{cat}×h)). Such CH_4-rich DRM is favourable to avoid H_2O formation from RWGS reaction but faces the obstacle of low CO_2 content that leads to rapid carbon deposition on unmodified catalyst Ni/$Mg_{1.3}AlO_x$ [2]. In other words, the gasification of carbon stemming from MD and BD reactions is limited, which was indicated by higher carbon amount analysed after DRM at 750 °C with CH_4/CO_2 = 2 compared to that with CH_4/CO_2 = 1 (Figure 6.4). Therefore, by applying CH_4-rich DRM, the benefits of the catalyst modifications for successful carbon suppression at such severe conditions were clarified.

In Figure 6.6, the conversions of CH_4 and CO_2 increase with temperature because of the endothermic nature of the reaction. The CO_2 conversion was remarkably higher than that of CH_4 because the latter was present in surplus. Among the $Mg_{1.3}AlO_x$ supported catalysts, Ni/$Mg_{1.3}AlO_x$ exposes lowest conversions and fastest deactivation at both temperatures while the three other catalysts have similar conversions and maintain their activity for at least 8 hours on stream. This observation can be suggested as another proof for the Ni re-oxidation by CO_2 proposed in the previous chapter. Indeed, in DRM with CH_4/CO_2 ratio = 1, partial Ni re-oxidation by CO_2 could occur with all La and/or CA modified catalysts, subsequently decreasing conversions below those with Ni/$Mg_{1.3}AlO_x$ (Figure 5.10). Such undesired Ni transformation in DRM is expected to be reduced by the lower concentration of CO_2 (CH_4/CO_2 = 2), taking advantage of the higher activities of modified catalysts. Compared to Ni/$Mg_{1.3}AlO_x$, CA-modified catalysts, La.Ni(CA)/$Mg_{1.3}AlO_x$ and Ni(CA)/$Mg_{1.3}AlO_x$ reveal more stable activity which can be assigned to their stronger MSI (Figure 5.2 and Figure 5.3a), probably leading to preserved dispersion of Ni atoms during CH_4-rich DRM, similar to the results in last chapter with CH_4/CO_2 = 1 (Figure 5.5b and d).

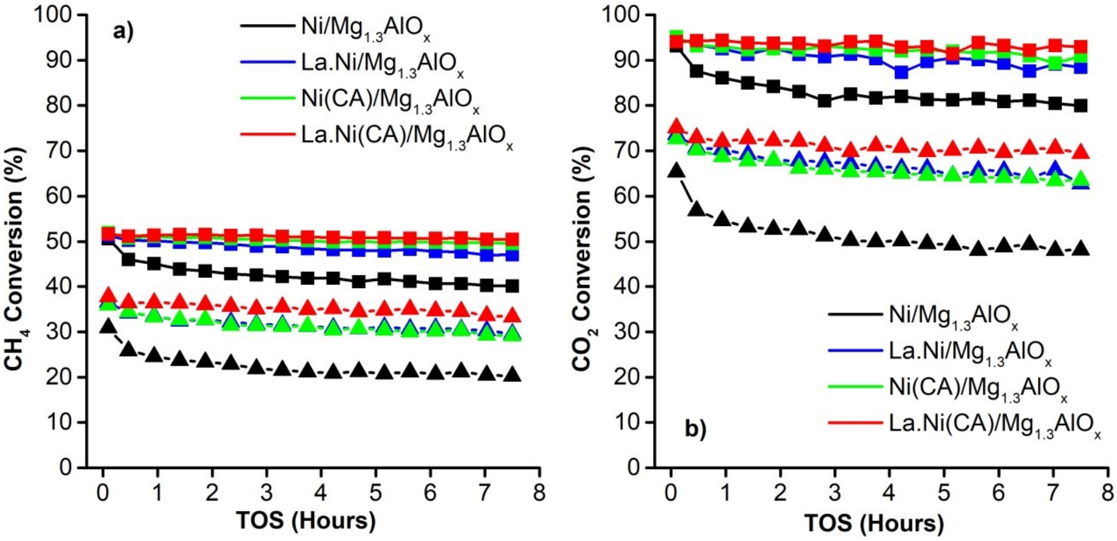

Figure 6.6. a) CH_4 conversions and b) CO_2 conversions of $Mg_{1.3}AlO_x$ supported Ni catalysts in CH_4-rich DRM at different temperatures (Triangles = 630 °C; squares = 750 °C, 1 bar, CH_4/CO_2 = 2, GHSV = 170 L/(g_{cat}×h),). All the catalysts were in situ pre-reduced at 700 °C for 1.5 hours prior to the reaction.

Almost unity H_2/CO ratio is attained with the modified catalysts at 750 °C (Figure 6.7a), reflecting the high H_2 selectivity and limited contribution of reverse water-gas shift reaction (Eq. 5). The coking behaviour in CH_4-rich DRM was characterized by the amount of carbon deposits analysed on spent catalysts after 8 hours on stream (Figure 6.7b). In contrast to the results in chapter 5 (Figure 5.11b), the enhanced coking resistance of La.Ni/$Mg_{1.3}AlO_x$ is not observed in CH_4-rich DRM compared to that of Ni/$Mg_{1.3}AlO_x$, probably because the carbon gasification effect by CO_2 becomes less advantageous in DRM with lower CO_2 partial pressure. It can be suggested that La.Ni/$Mg_{1.3}AlO_x$ promotes carbon removal mainly by gasification with CO_2 rather than by stabilizing a strong MSI as observed in the cases of La.Ni(CA)/$Mg_{1.3}AlO_x$ and Ni(CA)/$Mg_{1.3}AlO_x$. However, La.Ni/$Mg_{1.3}AlO_x$ leads to more stable conversions of CH_4 and CO_2 than Ni/$Mg_{1.3}AlO_x$ in DRM of CH_4-rich feed. This result is possibly due to the presence of La^{3+}, similarly to a study in which a Ni catalyst promoted with Na^+, another basic element, displayed stable activity even though serious coking was observed [206]. It should be noted that La.Ni/$Mg_{1.3}AlO_x$ displays higher carbon deposition at lower temperature (630 °C), indicating the significant contribution of BD similar to Ni/$Mg_{1.3}AlO_x$ (Figure 6.5). This issue is probably due to local defects or less dispersed Ni atoms in these two materials (Figure 5.3, Figure 5.8, Table 5.3), similar to what was proposed elsewhere [207, 208]. In contrast, when La.Ni(CA)/$Mg_{1.3}AlO_x$ or Ni(CA)/$Mg_{1.3}AlO_x$ with more finely dispersed Ni species were applied, better coking resistance was achieved in DRM with CH_4/CO_2 ratio = 2, especially at 630 °C (Figure 6.7b).

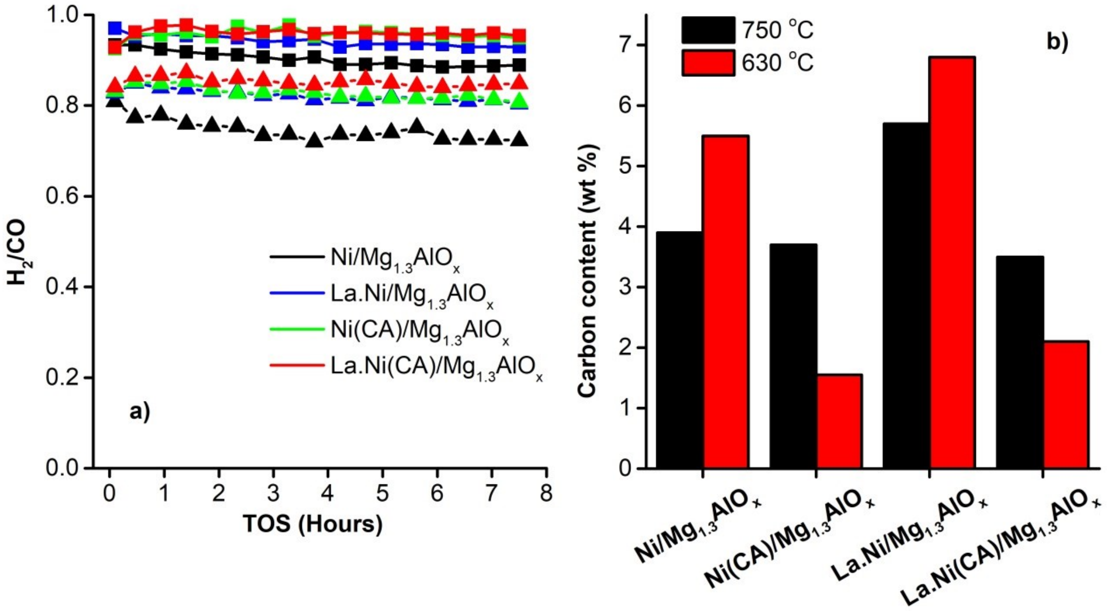

Figure 6.7. DRM performance of $Mg_{1.3}AlO_x$ supported Ni catalysts with CH_4-rich feed with a) H_2/CO ratio (triangles = 630 °C, squares = 750 °C) and b) fraction of carbon deposits after 8 hours on stream (1 bar, CH_4/CO_2 = 2, GHSV = 170 L/(g_{cat}×h)). All the catalysts were in situ pre-reduced at 700 °C for 1.5 hours prior to the reaction.

6.4 $Mg_{1.3}AlO_x$.1000 supported catalysts in CH_4-rich DRM

The modification of $Mg_{1.3}AlO_x$ supported Ni catalysts obviously offers benefits for CH_4-rich DRM at 630 °C (Figure 6.6 and Figure 6.7). However, there is a limitation to reduce the carbon formation at 750 °C which preferably runs via MD reaction. That challenge requires further enhancement of the catalyst properties. According to chapter 4, applying the thermal pre-treatment at 1000 °C to $Mg_{1.3}AlO_x$ before impregnation remarkably improved the interaction of Ni^{2+} species with the support ($Mg_{1.3}AlO_x$.1000) in the final catalyst. Therefore, Ni/$Mg_{1.3}AlO_x$.1000 and La.Ni(CA)/$Mg_{1.3}AlO_x$.1000 were evaluated in the same CH_4-rich DRM experiments in order to be compared with their corresponding $Mg_{1.3}AlO_x$ supported Ni catalysts.

Similar to Ni/$Mg_{1.3}AlO_x$, Ni/$Mg_{1.3}AlO_x$.1000 deactivates within 8 hours on stream at both reaction temperatures but with the lower rate (Figure 6.8). This difference depicts the expected higher MSI occurring in Ni/$Mg_{1.3}AlO_x$.1000 (Figure 4.5 and Figure 4.8a) that stabilizes the dispersion of Ni species during the reaction. Further modifying Ni/$Mg_{1.3}AlO_x$.1000 by La incorporation and CA-assisted synthesis led to better performance and stabilization improvement in CH_4-rich DRM. The conversions are even comparable with La.Ni(CA)/$Mg_{1.3}AlO_x$, the best performing catalyst in CH_4-rich DRM (previous section), especially at 750 °C. Compared to Ni/$Mg_{1.3}AlO_x$.1000, this better performance of La.Ni(CA)/$Mg_{1.3}AlO_x$.1000 can be assigned to the enhanced reducibility of Ni species in the presence of La (Figure 6.2, Table 6.2).

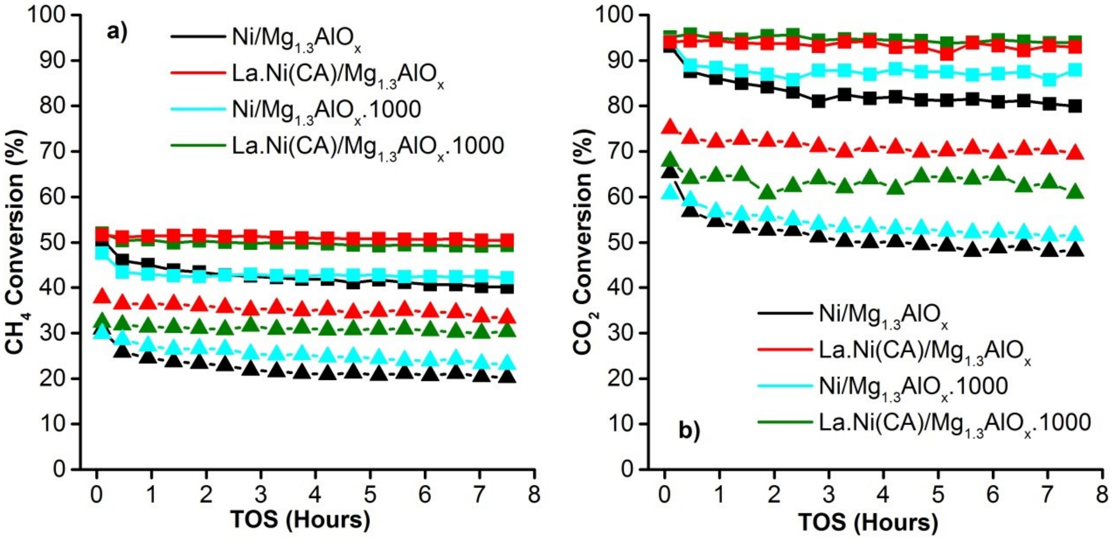

Figure 6.8. a) CH_4 conversions and b) CO_2 conversions of Ni catalysts supported on $Mg_{1.3}AlO_x$ or $Mg_{1.3}AlO_x$.1000 in CH_4-rich DRM at different temperatures (triangles = 630 °C or squares = 750 °C, 1 bar, $CH_4/CO_2 = 2$, GHSV = 170 L/(g_{cat}×h)). All the catalysts were in situ pre-reduced at 700 °C for 1.5 hours prior to the reaction.

La.Ni(CA)/$Mg_{1.3}AlO_x$.1000 also attains a stable H_2/CO ratio near unity at 750 °C (Figure 6.9a), exposing the high H_2 selectivity. The amounts of carbon deposits on spent catalysts after 8 hours on stream were also measured (Figure 6.9b). Among the presented samples, catalysts with $Mg_{1.3}AlO_x$.1000 support expose lower coking rate at both reaction temperatures. The carbon deposition in CH_4-rich DRM at high temperature (750 °C) is mainly formed by MD reaction and it was a problem with all studied $Mg_{1.3}AlO_x$ supported Ni catalysts (Figure 6.7b), but can be remarkably suppressed on La.Ni(CA)/$Mg_{1.3}AlO_x$.1000.

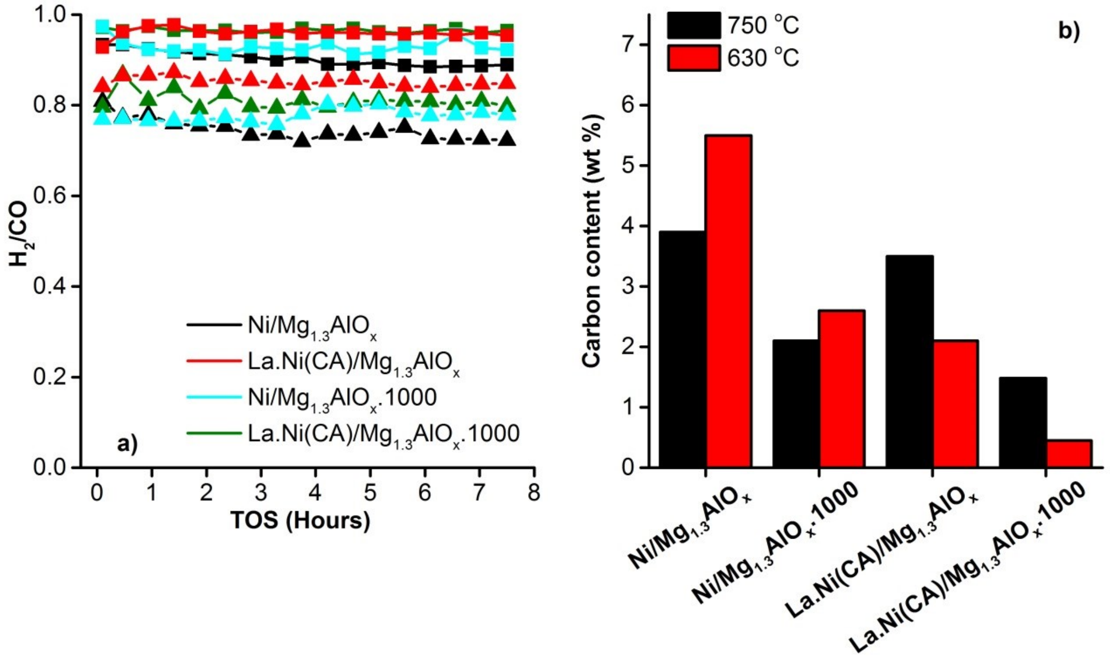

Figure 6.9. DRM performance of Ni catalysts on different supports with CH_4-rich feed with a) H_2/CO ratio (triangles = 630 °C, squares = 750 °C) and b) fraction of carbon deposits after 8 hours on stream (1 bar, $CH_4/CO_2 = 2$, GHSV = 170 L/(g_{cat}×h)). All the catalysts were in situ pre-reduced at 700 °C for 1.5 hours prior to the reaction.

In order to clarify this exceptional result, additional stoichiometric DRM experiments (Figure 6.10) and coking tests (Figure 6.11) were carried out. The significant low CH_4 and CO_2 conversions on both $Mg_{1.3}AlO_x$.1000 supported catalysts and also a gradual decline on La.Ni(CA)/$Mg_{1.3}AlO_x$.1000 are observed in stoichiometric DRM at 630 °C (Figure 6.10), probably reflecting the high contribution of Ni re-oxidation by CO_2. This effect may cause both low initial catalytic activity and gradual deactivation as seen in section 5.2 and 5.3. Compared to other $Mg_{1.3}AlO_x$ supported Ni catalysts and even Ni/$Mg_{1.3}AlO_x$.1000, this deactivation on La.Ni(CA)/$Mg_{1.3}AlO_x$.1000 happened even at low reaction temperature, reflecting the high impact of CO_2 oxidation potential toward this sample. However, this high CO_2 activation offered the advantage in CH_4-rich DRM.

On the other side, $Mg_{1.3}AlO_x$ supported Ni catalysts show almost similar or higher carbon contents in CH_4-rich DRM ($CH_4/CO_2 = 2$) compared to runs with $CH_4/Ar = 2$ (Figure 6.11). Therefore, as the coking tests with $CH_4/Ar = 2$ (no CO_2) elucidated the specific influence of MD on carbon deposition, these catalysts disclose low potential of CO_2 activation for carbon removal via gasification in CH_4-rich DRM. In contrast, Ni/$Mg_{1.3}AlO_x$.1000 and especially La.Ni(CA)/$Mg_{1.3}AlO_x$.1000 form lower amounts of carbon in CH_4-rich DRM compared to reaction with $CH_4/Ar = 2$. This difference reflects the high potential of these catalysts in CO_2 activation, even at low partial pressure, which cannot be seen with other Ni catalysts supported on

$Mg_{1.3}AlO_x$. The CO_2 activation, in this case, reduces the coking rate in CH_4-rich DRM due to MD reaction via the gasification reaction.

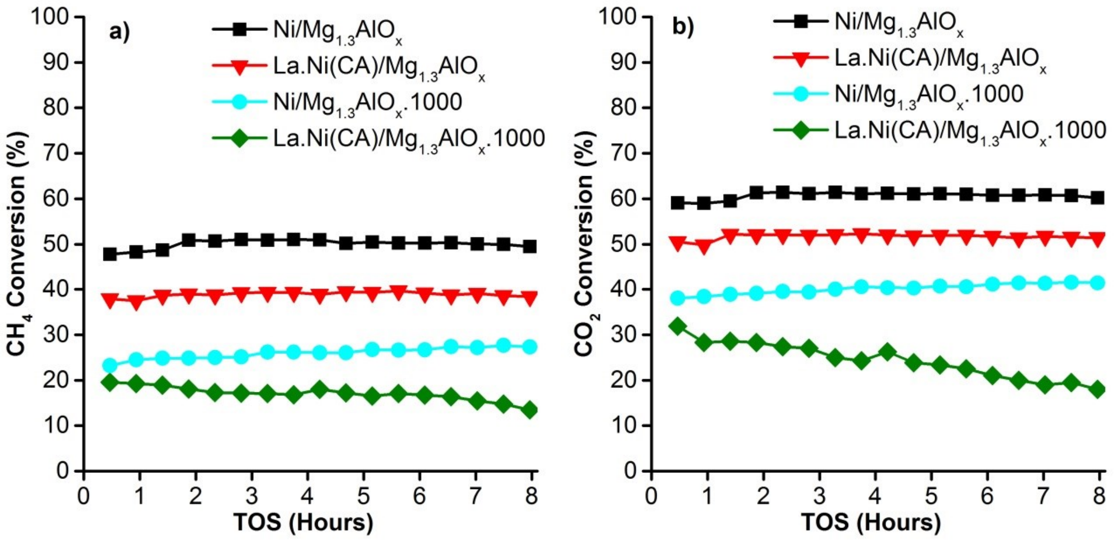

Figure 6.10. Conversions of a) CH_4 and b) CO_2 in DRM on La.Ni(CA)/$Mg_{1.3}AlO_x$.1000 in comparison with $Mg_{1.3}AlO_x$ supported catalysts (630 °C, 1 bar, $CH_4/CO_2 = 1$, GHSV = 170 L/(g_{cat}×h)). All the catalysts were pre-reduced in situ at 700 °C for 1.5 hours prior to the reaction.

This enhanced CO_2 activation is attributed to preferred NiO-MgO interaction in $Mg_{1.3}AlO_x$.1000 supported Ni catalysts. Indeed, this interaction in a catalyst with NiO-MgO solid solution structure was also previously claimed to be responsible for the improvement of CO_2 dissociation at the metal–support interface [77]. By that, the surface oxygen species would be effectively provided to react with intermediate CH_x intermediates adsorbed on Ni, surface Ni carbide, and bulk Ni carbide, thereby strengthening the resistance to carbon formation. In this study, the preferred NiO-MgO interaction in both Ni catalysts supported on $Mg_{1.3}AlO_x$.1000 can also be observed via their structures. The bare support $Mg_{1.3}AlO_x$.1000 exposes sharp and characteristic peaks assigned to periclase MgO which were not observed in any $Mg_{1.3}AlO_x$ supported Ni catalyst (Figure 6.1 and Figure 5.1). Compared to $Mg_{1.3}AlO_x$.1000, the two corresponding catalysts disclose XRD diffraction shifts assigned to the NiO-MgO solid solution formation (Figure 6.1). Besides, the UV-Vis spectra in the visible range of these two $Mg_{1.3}AlO_x$.1000 supported samples also show a stronger influence of MgO on doped Ni^{2+} than Ni/$Mg_{1.3}AlO_x$ or La.Ni(CA)/$Mg_{1.3}AlO_x$ (Figure 6.3b).

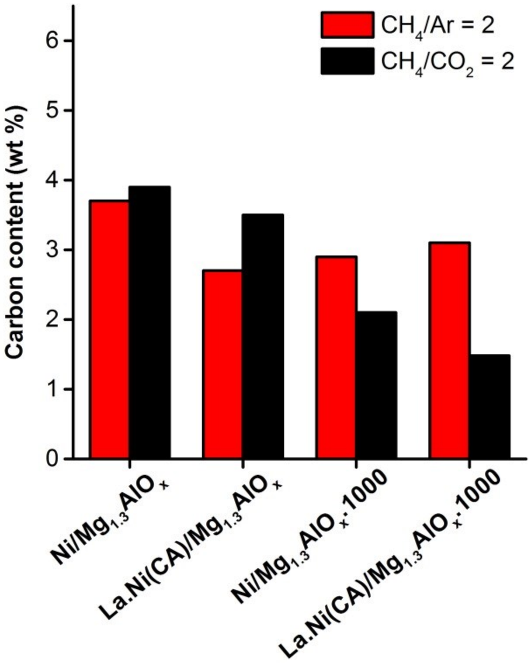

Figure 6.11. Carbon deposition on spent $La.Ni(CA)/Mg_{1.3}AlO_x.1000$ and $Ni/Mg_{1.3}AlO_x.1000$ after reaction with $CH_4/CO_2 = 2$ or $CH_4/Ar = 2$, in comparison with corresponding $Mg_{1.3}AlO_x$ supported Ni catalysts (750 °C, 1 bar, GHSV = 170 L/(g_{cat}×h)). The catalysts were pre-reduced in situ at 700 °C for 1.5 hours prior to the reaction.

Regarding the surface composition, the Ni $3p_{3/2}$ binding energy (Table 4.3) from XPS measurement of $Ni/Mg_{1.3}AlO_x$ (856.9 eV) shows the contribution of Ni^{2+} ions located in the surface $NiAl_2O_4$ spinel species (856.8 eV) [158]. The respective BE value of $Ni/Mg_{1.3}AlO_x.1000$ (856.1 eV) is close to that of Ni-containing surface species within NiO-MgO solutions (855.7 eV) [169, 170] (Figure 6.12). Thus, it can be indirectly inferred by this result that $La.Ni(CA)/Mg_{1.3}AlO_x.1000$ reveals a similar Ni surface behaviour. Among both Ni catalysts supported on $Mg_{1.3}AlO_x.1000$, $La.Ni(CA)/Mg_{1.3}AlO_x.1000$ has better coking resistance and more stable activity in CH_4-rich DRM due to the higher dispersity of Ni (Figure 6.2 and Figure 6.3a) and/or the presence of La^{3+}.

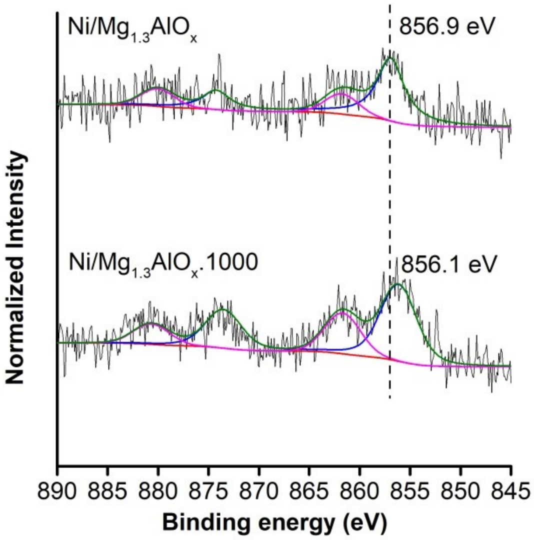

Figure 6.12. Ni 2p XPS plots of Ni/$Mg_{1.3}AlO_x$ and Ni/$Mg_{1.3}AlO_x$.1000 (colored lines: deconvoluted signals; blue = Ni $2p_{3/2}$ and Ni $2p_{1/2}$, magenta = corresponding satellite signals, green = averaged raw data).

6.5 Intermediate conclusion from chapter 6

No rapid carbon formation was observed during DRM with high content of CH_4 for all catalysts. La.Ni(CA)/$Mg_{1.3}AlO_x$ and Ni(CA)/$Mg_{1.3}AlO_x$ are able to maintain their activity over 8 hours in DRM at a high space velocity of CH_4-rich feedstock but they still suffer from carbon deposition at high temperature mainly due to the contribution of MD reaction.

Alternatively, the catalysts supported on $Mg_{1.3}AlO_x$.1000 show significantly improved coking resistance. La.Ni(CA)/$Mg_{1.3}AlO_x$.1000 appeares to be the best catalyst at high feed rate (170 L/(g_{cat}×h)) in CH_4-rich DRM as it presents high and stable activity over at least 8 hours on stream and coking rate is lowest at both temperatures (630 °C and 750 °C). Such best performance occurs most likely based on fine dispersion of Ni species, presence of La^{3+} and the preferable NiO-MgO interaction which excellently enhance CO_2 activation, thereby reducing the coking rate in CH_4-rich DRM.

However, this catalyst La.Ni(CA)/$Mg_{1.3}AlO_x$.1000, in turn, shows fast deactivation in stoichiometric DRM even at low reaction temperature due to high sensitivity to Ni re-oxidation at high partial pressure of CO_2. That drawback will limit the application of such catalyst in regular DRM. Therefore, the alternative ways to modify Ni catalysts offering better balanced performance between stoichiometric and CH_4-rich DRM should be investigated.

7 Modification of Ni catalysts with other rare earth elements

As illustrated in Figure 6.10, La.Ni(CA)/$Mg_{1.3}AlO_x$.1000 disclosed less stable conversions of CH_4 and CO_2 compared to other $Mg_{1.3}AlO_x$ supported Ni catalysts in stoichiometric DRM. In order to obtain a catalyst that is relatively stable at different DRM conditions (CH_4/CO_2 ratio), the modification of $Mg_{1.3}AlO_x$ supported Ni catalysts was considered.

La.Ni/$Mg_{1.3}AlO_x$ revealed a poor Ni dispersity and MSI leading to limited applicability in CH_4-rich DRM (section 6.3). The replacement of La^{3+} by Sc^{3+} and Gd^{3+} was implemented in development of catalysts for such severe DRM conditions. In the past, these rare earth elements (RE) were merely applied to DRM, especially for CH_4-rich DRM. According to our recent study [209], Ni catalyst with Sc^{3+} modified SiO_2 support provided better performance due to higher MSI. Addition of Gd^{3+} was also conducted to prevent the agglomeration of the Ni nanoparticles when embedding them into stable structures [210, 211].

In this chapter, the Ni/$Mg_{1.3}AlO_x$ was modified with Gd^{3+} and Sc^{3+} with molar ratio of RE:Ni = 0.8. On the best RE-doped Ni catalyst, a long-term stability test in CH_4-rich DRM was carried out in comparison with that on La.Ni(CA)/$Mg_{1.3}AlO_x$.1000. This is the first time that long-term CH_4-rich DRM experiments were studied, showing the potential for direct processing of CH_4-based gases with approximately 30% CO_2 into more valuable intermediate mixtures or products in industrial scale.

7.1 Catalyst characterization

The crystalline structures of Ni/$Mg_{1.3}AlO_x$ and samples thereof modified with different rare earth metal oxides (La^{3+}, Sc^{3+} and Gd^{3+}) are revealed by XRD measurements (Figure 7.1). They all show similar patterns comprising main diffractions assigned to several solid solution and/or spinel structures of the Mg-Al mixed oxides, similar to those Ni catalysts discussed in chapter 4 and 5. Rather than that, almost no clear pattern is observed for the impregnated compounds, probably due to the high dispersion.

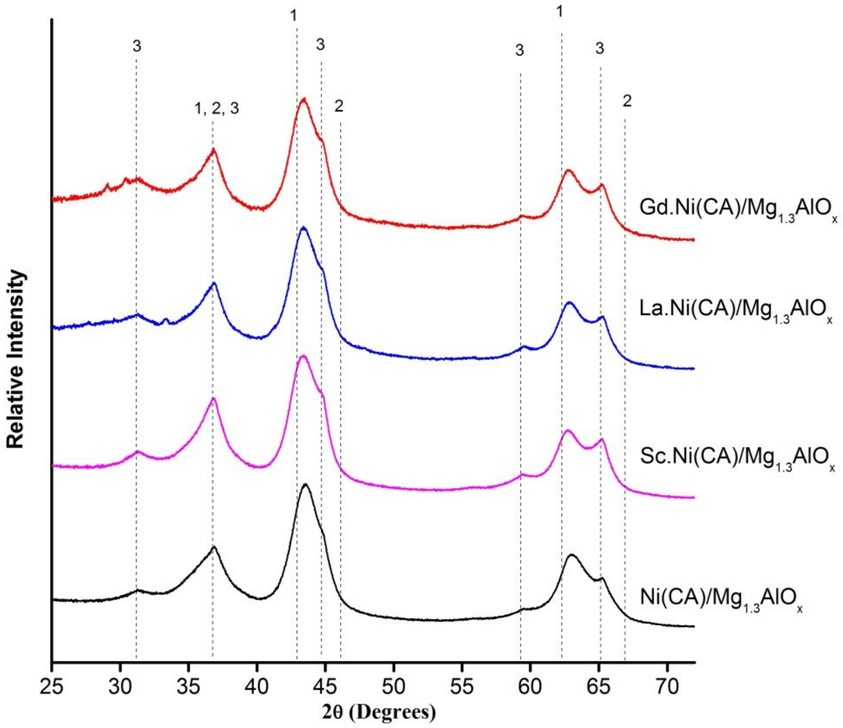

Figure 7.1. XRD patterns of $Mg_{1.3}AlO_x$ supported Ni catalysts modified with different rare earth metal oxides. Crystalline phases: periclase (MgO) (1), γ-Al_2O_3 (2), $MgAl_2O_4$ (3).

The textural parameter values of $Mg_{1.3}AlO_x$ supported catalysts are listed in Table 7.1. Compared to Ni/$Mg_{1.3}AlO_x$, the modified samples show lower BET surface area and pore volume values due to the increased surface coverage by RE^{3+} species. Besides, these values of modified samples are also varied, reflecting the impact of such parameters on the rare earth ion sizes. However, all catalysts show larger pore diameter compared to the sizes of the reactant molecules, indicating the less likely limitation of internal diffusion during the reaction.

Table 7.1. Textural properties of different $Mg_{1.3}AlO_x$ supported catalysts

Catalyst	S_{BET} (m^2/g)	Total pore volume (cm^3/g)	Average Pore Diameter (Å)
Ni/$Mg_{1.3}AlO_x$	174	0.40	74
La.Ni/$Mg_{1.3}AlO_x$	118	0.26	66
Sc.Ni/$Mg_{1.3}AlO_x$	150	0.33	64
Gd.Ni/$Mg_{1.3}AlO_x$	160	0.27	50

UV-Vis-DR plots in the region of 200-350 nm of Ni/$Mg_{1.3}AlO_x$ and RE modified samples are exposed in Figure 7.2, indicating the differences in aggregation state of the Ni species due to the corresponding LMCT bands. According to the literature [144, 211-214], the addition of oxides of La, Gd and Sc as lanthanide or rare earth modifiers to Ni catalysts was reported to influence the dispersion of active metal and to tune the MSI depending on nature of support and loading of these modifiers. In this study, the bands in UV region are weaker/blue shifted in case of Sc.Ni/$Mg_{1.3}AlO_x$ and Gd.Ni/$Mg_{1.3}AlO_x$ compared to those of Ni/$Mg_{1.3}AlO_x$ and La.Ni/$Mg_{1.3}AlO_x$, suggesting that better Ni dispersion is achieved in the two former samples. These Ni catalysts modified with Gd and Sc oxides with more finely dispersed Ni were expected to have stronger MSI with the applied $Mg_{1.3}AlO_x$.

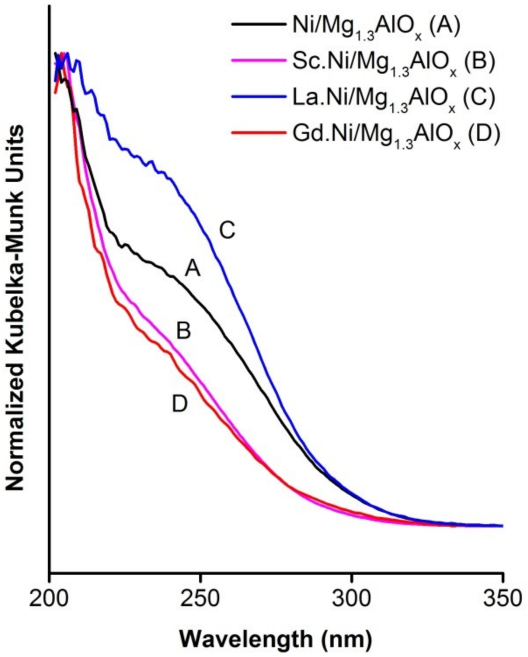

Figure 7.2. UV-Vis-DR spectra in the region 200-350 nm of $Mg_{1.3}AlO_x$ supported Ni catalysts modified with different rare earth metal oxides.

Reducibility of the catalysts was studied in order to determine their ability to form Ni in reductive atmospheres used before and during DRM. TPR profiles, consumed H_2 amounts and the molar ratio of RE/Ni of $Mg_{1.3}AlO_x$ supported Ni catalysts are presented in Figure 7.3 and Table 7.2.

Table 7.2. The H_2 consumption in TPR measurement and ICP results of the $Mg_{1.3}AlO_x$ supported Ni catalysts

Catalyst	H_2 consumption (µmol/g) [1]	Bulk molar ratio of RE/Ni [2]
Ni/$Mg_{1.3}AlO_x$	494	0
La.Ni/$Mg_{1.3}AlO_x$	550	0.78
Sc.Ni/$Mg_{1.3}AlO_x$	480	0.68
Gd.Ni/$Mg_{1.3}AlO_x$	482	0.80

(1) TPR results; (2) ICP results

Among these modified samples with quite comparable RE/Ni ratios, La.Ni/$Mg_{1.3}AlO_x$ is exceptional with an additional low-temperature peak and remarkably higher H_2 consumption (550 μmol/g) assigned to the above discussed distorted structures respective unusual oxidation states of Ni species (Ni^{3+}). Other samples show mainly reduction above 550 °C and comparable H_2 consumption of 480-494 μmol/g. However, shifts of main peak maxima to higher temperatures were observed in Gd (870 °C) and Sc (900 °C) modified catalyst samples compared to that of Ni/$Mg_{1.3}AlO_x$ (850 °C). Besides, these peaks in the first two samples are narrower and more symmetric, especially in the case of Ga.Ni/$Mg_{1.3}AlO_x$, probably pointing to better dispersed Ni species. These properties confirm the stronger interaction of Ni species and support when promoted with Sc and Gd oxides [214]. This interaction would be beneficial because it can prevent the mobility of the Ni particles on the support surface at high temperatures, possibly maintaining the catalyst performance and resisting the carbon accumulation.

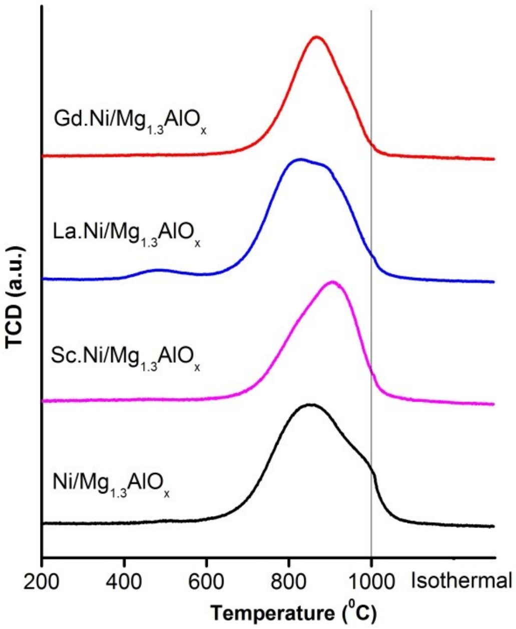

Figure 7.3. TPR profiles of supported Ni catalysts with different RE modifiers.

7.2 Performance of RE modified catalysts with $CH_4/CO_2 = 1$

7.2.1 Low temperature DRM

The DRM tests on $Mg_{1.3}AlO_x$ supported Ni catalysts were firstly carried out at 630 °C and GHSV = 170 L/(g_{cat}×h)) to distinguish the catalyst activities and the carbon accumulation stemming mainly from Boudouard reaction (as suggested in chapter 5 and 6).

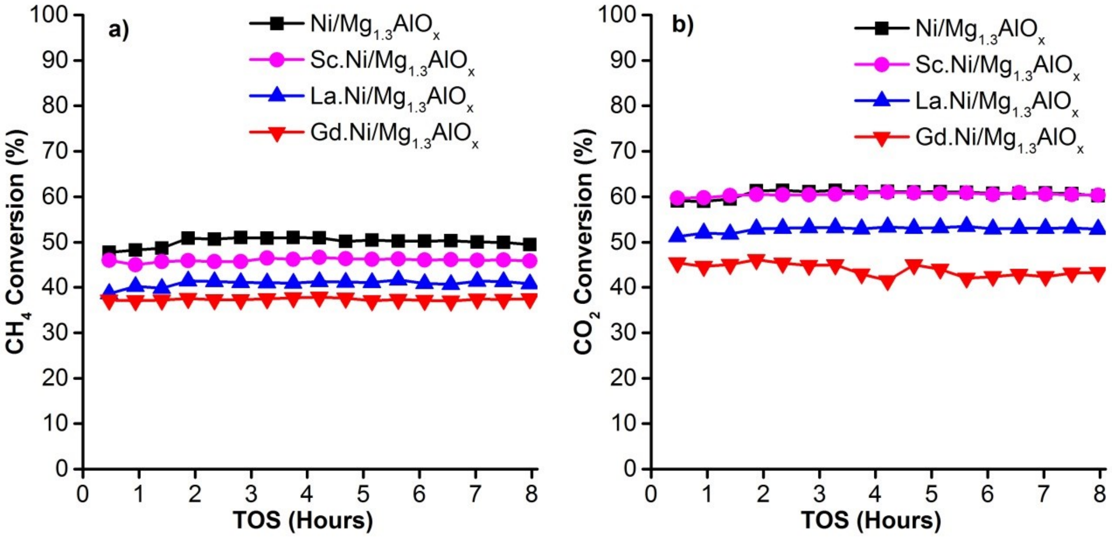

Figure 7.4. Conversions of a) CH_4 and b) CO_2 in DRM on RE-modified Ni catalysts (630 °C, 1 bar, $CH_4/CO_2 = 1$, GHSV = 170 L/(g_{cat}×h)). All the catalysts were pre-reduced in situ at 700 °C for 1.5 hours prior to the reaction.

All catalysts generally expose stable conversions of both CH_4 and CO_2 (Figure 7.4). Compared to $Ni/Mg_{1.3}AlO_x$, it should be noted that both $Sc.Ni/Mg_{1.3}AlO_x$ and $Gd.Ni/Mg_{1.3}AlO_x$ disclose stronger MSI and poorer reducibility (Figure 7.2, Figure 7.3). The Sc-containing catalyst has activity comparable with that of $Ni/Mg_{1.3}AlO_x$, whereas the Gd-modified sample shows a relative decline. However, compared to the performance of $La.Ni/Mg_{1.3}AlO_x$.1000 at the same DRM conditions (Figure 6.10), this Gd-modified sample still has higher and more stable activity.

The H_2/CO ratios in DRM obtained with all samples are clearly lower than unity (Figure 7.5a), revealing the low H_2 selectivity due to the H_2O formation via RWGS (Eq. 5). However, compared to $Ni/Mg_{1.3}AlO_x$, the coking rate is significantly reduced but diverged when different RE modifiers were applied (Figure 7.5b). While $Sc.Ni/Mg_{1.3}AlO_x$ only presents a moderate carbon formation (2.6 wt% after 8 hours of DRM), much less carbon is found on spent $Gd.Ni/Mg_{1.3}AlO_x$ and $La.Ni/Mg_{1.3}AlO_x$. According to the results in chapter 6, BD reaction plays an important role in carbon deposition at 630 °C. Therefore, similar to $La.Ni/Mg_{1.3}AlO_x$, it could be suggested that $Gd.Ni/Mg_{1.3}AlO_x$ more effectively promotes the surface carbon gasification via dissociative CO_2 adsorption. Consequently, although both $Sc.Ni/Mg_{1.3}AlO_x$ and $Gd.Ni/Mg_{1.3}AlO_x$ show stable activity and strong MSI being good for coking resistance (chapter 5), the latter may reveal higher carbon oxidation potential that can effectively remove carbon.

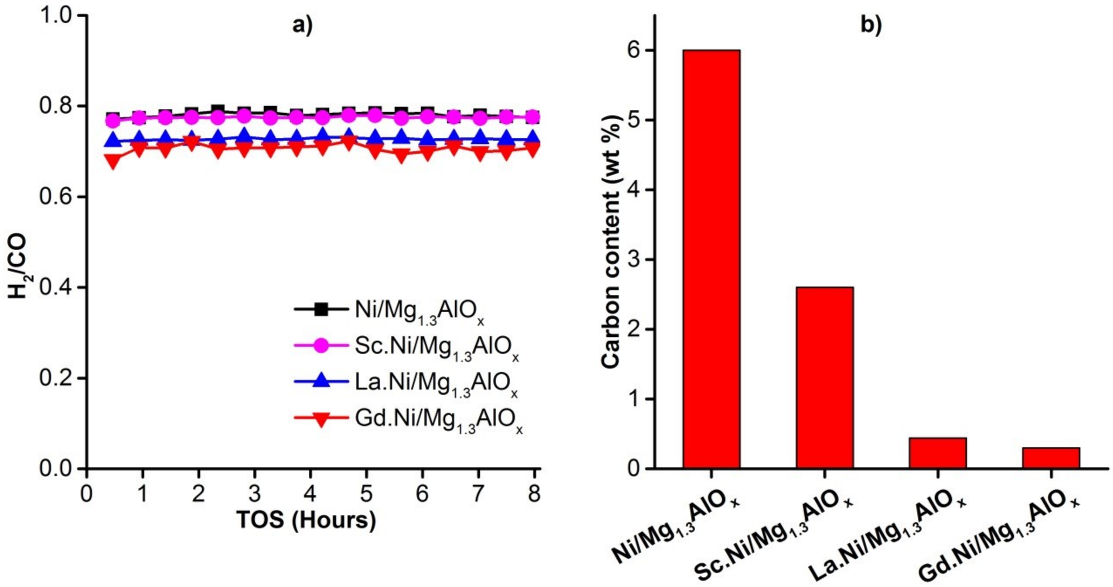

Figure 7.5. DRM performance of modified Ni catalysts with a) H_2/CO ratio and b) fraction of carbon deposits on spent catalysts after DRM (630 °C, 1 bar, $CH_4/CO_2 = 1$, GHSV = 170 L/(g_{cat}×h), TOS = 8 hours). All the catalysts were pre-reduced in situ at 700 °C for 1.5 hours prior to the reaction.

7.2.2 High temperature DRM

All the RE-modified catalysts were applied to DRM at more severe conditions, first by increasing temperature (T = 750 °C, GHSV = 170 L/(g_{cat}×h). According to the results in chapter 5, the Ni catalysts are less prone to high coking rate because the BD is not favoured at this temperature [50]. However, the catalysts are then deactivated by partial Ni re-oxidation by CO_2 that can oxidize both C and Ni. The carbon amounts deposited on all spent samples were negligible (< 1 wt%, not shown here) after 20 hours on stream. All catalysts expose stable activity over complete time on stream except Gd.Ni/$Mg_{1.3}AlO_x$, which is gradually deactivated by approximately 10% within 10 hours on stream (Figure 7.6). It should be noted that this deactivation occurred although the catalyst exposed strong MSI and low coking rate, probably reflecting the contribution of proposed Ni oxidation by CO_2.

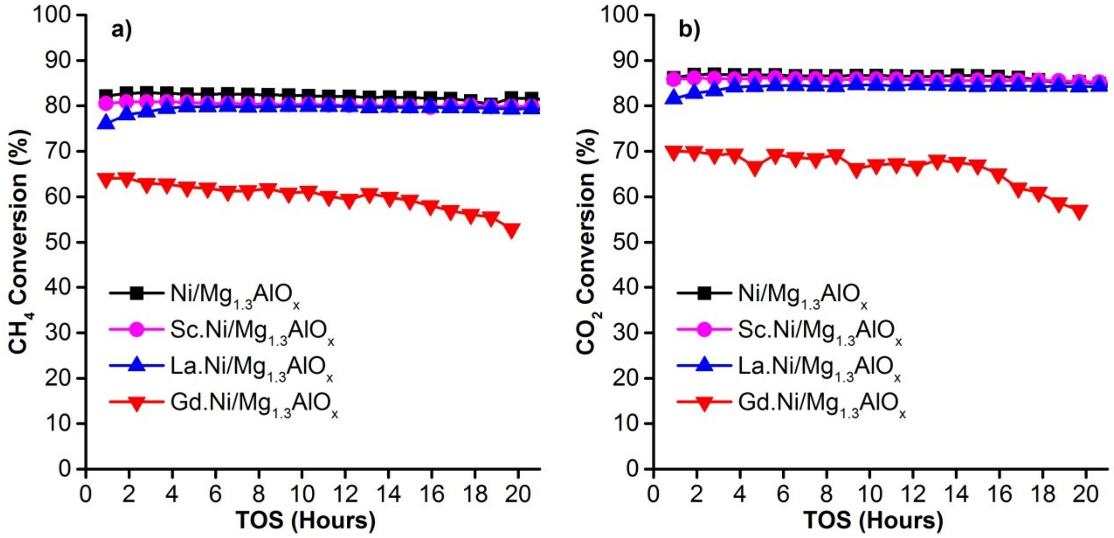

Figure 7.6. Conversions of a) CH_4 and b) CO_2 in DRM on modified Ni catalysts (750 °C, 1 bar, CH_4/CO_2 = 1, GHSV = 170 L/(g_{cat}×h)). All the catalysts were pre-reduced in situ at 700 °C for 1 hour prior to the reaction.

7.3 Performance of RE-modified catalysts in CH_4-rich DRM

Opposing to reaction with CH_4/CO_2 = 1, the DRM activity tests with CH_4/CO_2 = 2 were presumed to suppress the partial Ni re-oxidation by setting lower CO_2 partial pressure. All modified catalysts present stable conversions of CH_4 and CO_2 during 8 hours on stream while Ni/$Mg_{1.3}AlO_x$ is gradually deactivated. Among these samples, Gd.Ni/$Mg_{1.3}AlO_x$ and Sc.Ni/$Mg_{1.3}AlO_x$ maintain initial activity (Figure 7.7a) due to their high Ni dispersion and strong MSI, but the Gd-based sample reveals even higher stability which can be attributed to its better reducibility (Figure 7.3).

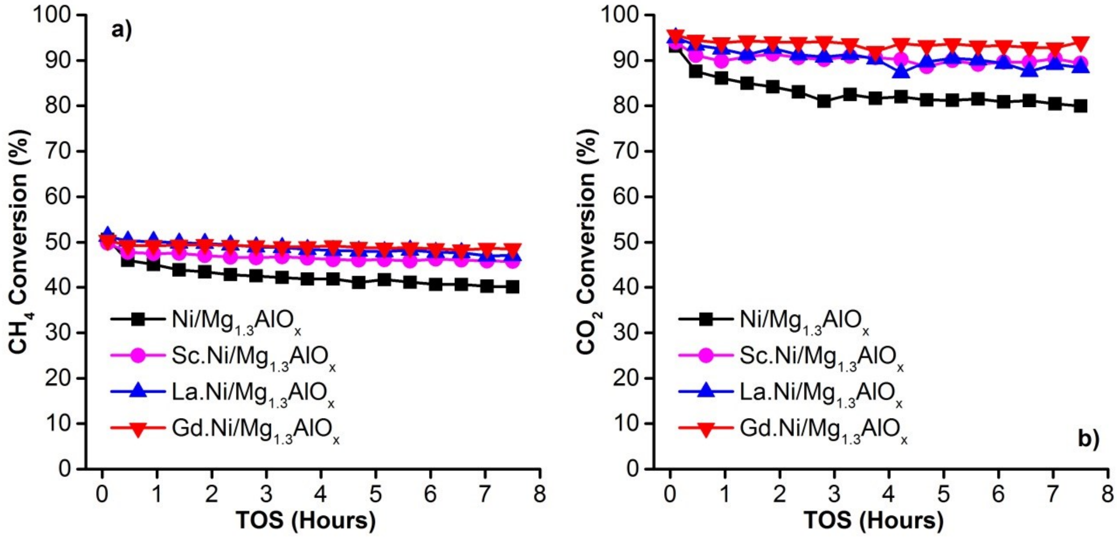

Figure 7.7. CH_4-rich DRM performance of RE-modified Ni catalysts with a) CH_4 conversions and b) CO_2 conversions (750 °C, 1 bar, CH_4/CO_2 = 2, GHSV = 170 L/(g_{cat}×h)). All the catalysts were in situ pre-reduced at 700 °C for 1.5 hours prior to the reaction.

Both samples also give high and stable H_2 selectivity with H_2/CO values near unity (Figure 7.8a). The coking rate on Ni catalysts was evaluated via analysis of the carbon deposition on spent catalysts after 8 hours on stream (Figure 7.8b). As suggested in chapter 6, DRM of CH_4-rich feed encounters serious issues with fast coking due to the shortage of CO_2 that causes insufficient carbon gasification. Among the catalysts, Gd and Sc modified samples show enhanced coking resistance, probably due to their strong MSI. However, the suppression of carbon deposition on these catalysts is even better than that of Ni catalysts prepared with CA at the same CH_4-rich DRM conditions (Figure 6.7b), probably due to other side effects rather than strong MSI. Among these two RE modified catalysts, the carbon elimination is more effective in case of Gd.Ni/$Mg_{1.3}AlO_x$ probably because of the higher impact of CO_2.

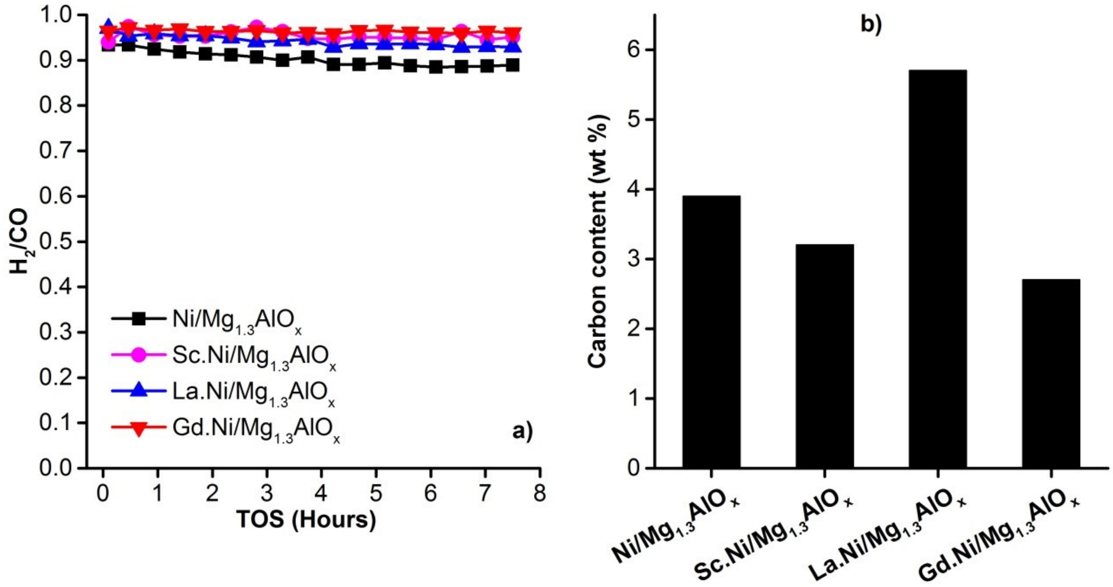

Figure 7.8. CH_4-rich DRM performance of RE modified Ni catalysts with a) H_2/CO ratio and b) fraction of carbon deposits after 8 hours on stream (750 °C, 1 bar, $CH_4/CO_2 = 2$, GHSV = 170 L/(g_{cat}×h)). All the catalysts were in situ pre-reduced at 700 °C for 1.5 hours prior to the reaction.

In order to indicate the main factors influencing the carbon deposition in CH_4-rich DRM of Gd.Ni/$Mg_{1.3}AlO_x$, the coking test (MD) with the feed of $CH_4/Ar = 2$ was additionally conducted (Figure 7.9). This test points out that, Gd.Ni/$Mg_{1.3}AlO_x$ disclosed the higher carbon deposition in CH_4-rich DRM compared to that of reaction with $CH_4/Ar = 2$. This behaviour of Gd.Ni/$Mg_{1.3}AlO_x$ is similar to other $Mg_{1.3}AlO_x$ supported Ni catalysts (Figure 6.11 and Figure 7.9), elucidating also the limitation of CO_2 activation for carbon removal via gasification in CH_4-rich DRM. As a result, the $Mg_{1.3}AlO_x$ supported Ni catalysts may achieve highest potential of CO_2

activation in stoichiometric DRM on Gd.Ni/$Mg_{1.3}AlO_x$ that is beneficial for carbon removal (Figure 5.11b and Figure 7.5b). However, this activation on Gd.Ni/$Mg_{1.3}AlO_x$ was insufficient to suppress the carbon formation when the CO_2 partial pressure was reduced.

Nevertheless, it should be noted that the low carbon deposition on spent Gd.Ni/$Mg_{1.3}AlO_x$ after the reaction with CH_4/Ar = 2 is exceptional among the Ni catalysts (Figure 6.11 and Figure 7.9) which can be assigned to the ability of such catalyst to prevent MD cracking.

It was previously observed that the rate of CH_4 activation step (Eq. 12) is slowed down compared to that of CO_2 dissociation in the presence of RE^{3+} elements [38]. Besides, the interaction of Ni species and the supports affects the activation of the C–H bond governing the extent of methane cracking [51]. In other words, as CH_4 forms a variety of CH_x species (x: number of H atom in CH_4 molecule, x = 0 - 4) through dissociative adsorption [38], higher MSI in Ni catalysts obviously leads to a higher value of x and consequently reduces the formation of C atoms as coke precursors. Therefore, these properties of Gd.Ni/$Mg_{1.3}AlO_x$ can be suggested to decrease the rate of CH_4 decomposition which is the main carbon source in both CH_4/Ar reaction and CH_4-rich DRM. Therefore, as CH_4 dissociation rate may be lower compared to that of CO_2, the high impact of CO_2 on Gd.Ni/$Mg_{1.3}AlO_x$ can be explained that rules the high coking resistance in both CH_4-rich and stoichiometric DRM.

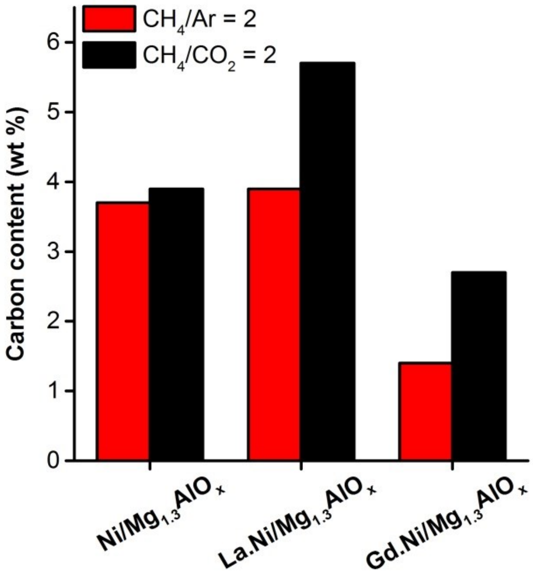

Figure 7.9. Carbon deposition on spent Gd.Ni/$Mg_{1.3}AlO_x$ after reaction with CH_4/CO_2 = 2 or CH_4/Ar = 2, in comparison with other $Mg_{1.3}AlO_x$ supported Ni catalysts (750 °C, 1 bar, GHSV = 170 L/(g_{cat}×h)). The catalysts were pre-reduced in situ at 700 °C for 1.5 hours prior to the reaction.

7.4 Long-term stability in DRM with $CH_4/CO_2 = 2$ and benchmark comparison

The two best catalysts in DRM of CH_4-rich feedstock from chapter 6 and 7 were employed in long-term tests over 100 hours at the same temperature of 750 °C and GHSV of 170 L/(g_{cat}×h) (Figure 7.10). Over 100 hours on stream of CH_4-DRM, both Gd.Ni/$Mg_{1.3}AlO_x$ and La.Ni(CA)/$Mg_{1.3}AlO_x$.1000 presented quite similar CH_4 and CO_2 conversions with a slightly decreasing trend which can mostly be assigned to the unavoidable Ni agglomeration. The spent catalysts were characterized and limited carbon amounts (~ 6 wt%) were determined on both samples (Figure 7.11). Such carbon deposition contents were predictably higher but did not significantly exceed the values in 8 hour DRM tests, pointing out the stable performance achieved with these two catalysts.

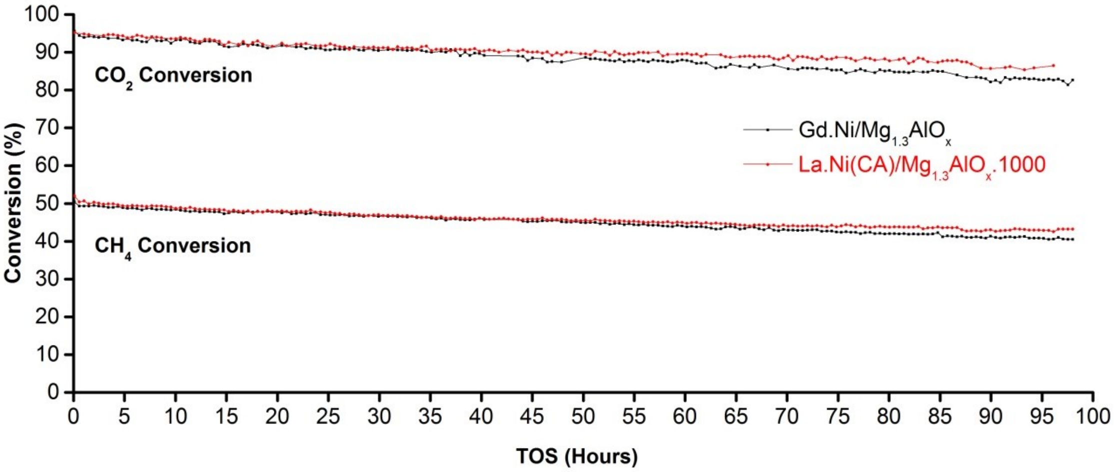

Figure 7.10. CH_4 and CO_2 conversions in long-term CH_4-rich DRM of Gd.Ni/$Mg_{1.3}AlO_x$ and La.Ni(CA)/$Mg_{1.3}AlO_x$.1000 (750 °C, 1 bar, $CH_4/CO_2 = 2$, GHSV = 170 L/(g_{cat}×h)). All the catalysts were pre-reduced in situ at 700 °C for 1.5 hours prior to the reaction.

It should be noted that, compared to La.Ni(CA)/$Mg_{1.3}AlO_x$.1000, Gd.Ni/$Mg_{1.3}AlO_x$ exposed lower carbon resistance potential in CH_4-rich DRM during 8 hours on stream. As a result, it can be suggested that these two catalysts disclosed dissimilar carbon suppression mechanisms with different efficiency within 8 hours on stream. However, after the long-term stability both catalysts reveal comparable carbon amounts (Figure 7.11). By that, the less stability of the main coking resistance pathway of La.Ni(CA)/$Mg_{1.3}AlO_x$.1000, CO_2 activation potential, can be suggested. This instability is probably related to the unavoidable agglomeration of Ni atoms during the reaction, leading to the loss of Ni surfaces and metal-support interfaces which are the preferable sites for dissociative CO_2 adsorption [51] (Figure 2.1). Therefore, Gd.Ni/$Mg_{1.3}AlO_x$ can be also considered as promising candidate for CH_4-

rich DRM that gives exceptional performance and stability comparable to that of La.Ni(CA)/$Mg_{1.3}AlO_x$.1000.

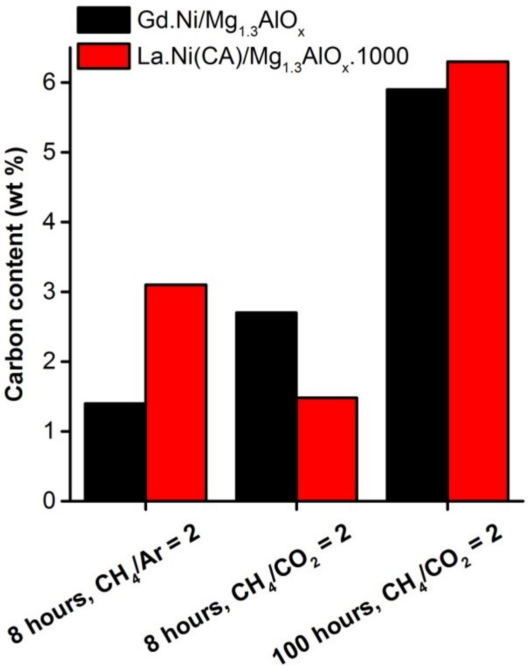

Figure 7.11. Carbon deposition on spent Gd.Ni/$Mg_{1.3}AlO_x$ and La.Ni(CA)/$Mg_{1.3}AlO_x$.1000 at different DRM conditions and time scales (750 °C, 1 bar, GHSV = 170 L/(g_{cat}×h)). The catalysts were pre-reduced in situ at 700 °C for 1.5 hours prior to the reaction

It was previously claimed that it should be almost impossible to fully avoid carbon accumulation at high CH_4/CO_2 ratio with Ni catalysts [215], and thus the quantity of studies focusing on DRM of CH_4-rich mixture is insignificant due to the commonly expected severe coking rate [66]. Such fast carbon deposition apparently makes transition metal catalysts impractical for maintaining stable performance [3]. However, in the present study, the applied catalyst modifications (use of RE and/or CA during preparation and proper support thermal pre-treatment) clearly better suppress carbon formation and stabilize the conversions of both reactants as compared to Ni/$Mg_{1.3}AlO_x$. Both Gd.Ni/$Mg_{1.3}AlO_x$ and La.Ni(CA)/$Mg_{1.3}AlO_x$.1000 show a remarkably low amount of carbon deposits after 8 hours on stream in CH_4-rich DRM and maintain this excellent stability over 100 hours. Actually, several studies were focusing on Ni-based catalysts for such harsh conditions [66]. Likely, they faced the obstacle with higher rate of coking than that observed in this study, causing fast deactivation or even reactor blockage [216, 217]. Only few investigations [124, 218, 219] presented results from DRM of CH_4-rich feed with low coking rates. However, in these investigations, the lower space velocities, application of noble promoters, and most important shorter time on stream, were selected that limit the meaningful comparison to the results achieved in this study.

7.5 Intermediate conclusion from chapter 7

Modification of Ni catalysts with Sc^{3+} and Gd^{3+} enhances performance and coke resistance in DRM of both stoichiometric and CH_4-rich mixtures. Among $Mg_{1.3}AlO_x$ supported catalysts, Gd^{3+} containing sample discloses lowest carbon deposition in both stoichiometric and CH_4-rich DRM, probably relating to its CH_4 cracking rate limitation.

Gd.Ni/$Mg_{1.3}AlO_x$ also showed the CO_2 activation but with lower potential compared to that of La.Ni(CA)/$Mg_{1.3}AlO_x$.1000 which discloses more limited application in stoichiometric DRM due to its higher Ni re-oxidation possibility by CO_2. However, as Gd.Ni/$Mg_{1.3}AlO_x$ obviously limits the rate of CH_4 cracking, it exposes relatively stable activity over 100 hours on stream with limited carbon amounts, making it comparable with La.Ni(CA)/$Mg_{1.3}AlO_x$.1000. These results are exceptional regarding the implementation of CH_4-rich DRM that provides opportunities for further synthesis gas production from biogas or CO_2-rich natural gas direct conversion.

8 Thesis conclusions

In this PhD research, various low Ni content catalyst formulations were elaborated that have an exceptionally high and stable performance at different DRM conditions. These formulations are based on Mg-Al mixed oxides offering the ability to adjust catalyst structure, metal coordination, reducibility and MSI via several pre-treatment and modification processes. It was found that La.Ni(CA)/$Mg_{1.3}AlO_x$ is the most promising catalyst for stoichiometric DRM because it maintained the high activity and H_2 productivity over 160 hours. On the other side, it is inefficient for the CH_4-rich reaction in terms of strictly required coking resistance. In contrast, La.Ni(CA)/$Mg_{1.3}AlO_x$.1000 and Gd.Ni/$Mg_{1.3}AlO_x$ showed promising application potential for operation at such severe DRM conditions over 100 hours on stream with exceptionally low carbon deposition but may be unsuitable for DRM with an equimolar mixture of CH_4 and CO_2 at chosen GHSV. Therefore, depending on the properties of the Ni catalysts, there are corresponding preferred applications in DRM at different conditions.

The Mg-Al supports play a key role in DRM performance of Ni catalysts. Each component, either MgO or Al_2O_3 in the support, has its specific tendency to form a stable structure with Ni^{2+}. By selecting suitable parameters, the precursor hydrotalcite is converted into the material $Mg_{1.3}AlO_x$ and to prepare a low Ni content catalyst that has high activity in stoichiometric DRM. The crystalline structure of resulting catalyst Ni/$Mg_{1.3}AlO_x$ is quite complicated, mainly comprising the mixed phases of solid solution and spinel structure formed by both oxides MgO and Al_2O_3. However, thanks to UV-Vis spectroscopy in the visible range, XPS and TPR, the coordination, location and metal-support interaction (MSI) of Ni species were revealed. These species were found octahedrally coordinated in solid solution of Ni-Mg-Al mixed oxides, preferably located on the support surface and obtained low MSI. These properties are responsible for its high activity observed via high CH_4 and CO_2 conversions even at low reaction temperature and high space velocity. Ni catalysts with other support composition and pre-treatment temperatures may preferably form Ni^{2+} in $NiAl_2O_4$ or NiO-MgO structures which are less reducible and/or available at the surface, thus lowering catalyst activity in DRM.

However, as predicted, the high availability of surface metal species with low MSI may lead to poor metal dispersion that negatively affects the catalyst stability and coking resistance in DRM. Therefore, different modification routes for Ni/$Mg_{1.3}AlO_x$ were implemented in terms of improving the dissociative adsorption of CO_2 and/or enhancement of Ni dispersion and MSI. The modified catalysts show different coking resistance mechanisms depending on their properties and the reaction conditions. It was figured out that, the Gd-, Sc- or CA-modified Ni catalysts with improved Ni dispersity and MSI were stabilized against rapid coke formation and metal agglomeration. Especially, Gd-modified sample exposes the additional effect of CH_4 cracking rate limitation. In contrast, the sample modified with rare earth metal oxide (La^{3+}) having only the CO_2 activation effect without the mentioned strong MSI may be insufficiently effective in reaction with the lower partial pressure of CO_2 (in CH_4-rich DRM) which is the vital oxidative species for removal of carbon atoms stemming from CH_4 cracking. The catalysts with support $Mg_{1.3}AlO_x$ pre-treated at 1000 °C disclosed preferable NiO-MgO interaction that enhances the catalyst stability and carbon suppression even in CH_4-rich DRM. Among all studied catalysts, La.Ni(CA)/$Mg_{1.3}AlO_x$.1000 and Gd.Ni/$Mg_{1.3}AlO_x$ offered the combinations of different improvement attributes leading to their most excellent performance with regard to coking resistance and activity stabilization in the severe reaction conditions of CH_4-rich DRM and high temperature. This is the DRM condition in which most Ni catalysts were seriously affected by rapid coking and/or metal agglomeration.

This study also revealed a less discussed deactivation pathway, namely Ni re-oxidation. This Ni transformation may only be observed in stoichiometric DRM on low Ni content catalysts that are modified to obtain high CO_2 activation potential. On these catalysts, both carbon and Ni react as the reducing agents that are oxidized at a high CO_2 partial pressure, leading to negligible coking but also the formation of Ni/$NiO_{1-\delta}$ clusters over the spent catalysts. The formation of these Ni/$NiO_{1-\delta}$ species results in the gradual decreasing of the activity of the catalysts in DRM. This deactivation pathway limits the application of particular modified Ni catalysts in stoichiometric DRM which is seen most critical in case of La.Ni(CA)/$Mg_{1.3}AlO_x$.1000. La.Ni(CA)/$Mg_{1.3}AlO_x$ appears to be the most promising candidate for stoichiometric DRM, not only showing coking resistance but also achieving exceptional high and stable DRM performance against mentioned Ni re-oxidation.

Although much progress has been made on those Ni catalysts in this thesis, the H_2/CO ratio as a measure for selectivity is always below 1, limiting the application of the DRM products. Therefore, further studies should be made on Ni-based catalyst from this work, combining DRM with partial oxidation of methane and/or steam reforming via autothermal reforming (ARM) or tri-reforming (TRM). These combinations can help to minimize the carbon deposition problem and to reduce amounts of heat required for operation as well as to control H_2/CO ratio.

This work focused less on the impact of catalyst preparation method on the DRM performance. According to the literature, Ni can also be substituted into the parent structure of Mg-Al mixed oxide by one-step sol-gel, co-precipitation or via hydrolysis/condensation methods. These are preferred to obtain defined powder particle size and uniform pores compared to impregnation. Furthermore, with a suitable preparation technology, the final powdered Ni catalyst can be anchored on a cordierite-based monolith as a carrier. The monolith catalyst applied for DRM will be a step closer to the industrial scale, where the catalyst has to be shaped before any utilization.

References

[1] İ. Yıldız, 1.12 Fossil Fuels, in: I. Dincer (Ed.) Comprehensive Energy Systems, Elsevier, Oxford, 2018, pp. 521-567.

[2] M. Usman, W.M.A. Wan Daud, H.F. Abbas, Renewable and Sustainable Energy Reviews, 45 (2015) 710-744.

[3] M.C.J. Bradford, M.A. Vannice, Catalysis Reviews, 41 (1999) 1-42.

[4] J.H. Butler, S.A. Montzka, The NOAA Annual Greenhouse Gas Index (AGGI), (2018).

[5] R.J.H. Dunn, D.M. Stanitski, N. Gobron, K.M. Willett, Global Climate, in: G. Hartfield, J. Blunden, D.S. Arndt (Eds.) State of the Climate in 2017, Bulletin of the American Meteorological Society, Boston, 2018, pp. S5-S68.

[6] D. Lüthi, M. Le Floch, B. Bereiter, T. Blunier, J.-M. Barnola, U. Siegenthaler, D. Raynaud, J. Jouzel, H. Fischer, K. Kawamura, T.F. Stocker, Nature, 453 (2008) 379.

[7] B. Bereiter, S. Eggleston, J. Schmitt, C. Nehrbass-Ahles, T.F. Stocker, H. Fischer, S. Kipfstuhl, J. Chappellaz, Geophysical Research Letters, 42 (2015) 542-549.

[8] W.-J. Jang, J.-O. Shim, H.-M. Kim, S.-Y. Yoo, H.-S. Roh, Catalysis Today, 324 (2019) 15-26.

[9] S. Faramawy, T. Zaki, A.A.E. Sakr, Journal of Natural Gas Science and Engineering, 34 (2016) 34-54.

[10] S. Sokolov, E.V. Kondratenko, M.-M. Pohl, A. Barkschat, U. Rodemerck, Applied Catalysis B: Environmental, 113-114 (2012) 19-30.

[11] G. Centi, S. Perathoner, Perspectives and State of the Art in Producing Solar Fuels and Chemicals from CO_2, in: G. Centi, S. Perathoner (Eds.) Green Carbon Dioxide, John Wiley & Sons, Inc, New Jersey, United States of America, 2014, pp. 1-24.

[12] R.O. Yusuf, Z.Z. Noor, A.H. Abba, M.A.A. Hassan, M.F.M. Din, Renewable and Sustainable Energy Reviews, 16 (2012) 5059-5070.

[13] B. Li, Energy Economics, 78 (2019) 91-108.

[14] BP Statistical Review of World Energy BP p.l.c., London, United Kingdom(2018).

[15] G.A. Olah, A. Goeppert, M. Czaun, T. Mathew, R.B. May, G.K.S. Prakash, Journal of the American Chemical Society, 137 (2015) 8720-8729.

[16] G. Karavalakis, T.D. Durbin, M. Villela, J.W. Miller, Journal of Natural Gas Science and Engineering, 4 (2012) 8-16.

[17] J.-H. Kim, D.J. Suh, T.-J. Park, K.-L. Kim, Applied Catalysis A: General, 197 (2000) 191-200.

[18] P. Djinović, I.G. Osojnik Črnivec, B. Erjavec, A. Pintar, Applied Catalysis B: Environmental, 125 (2012) 259-270.

[19] B. Raco, R. Battaglini, M. Lelli, Environmental Science and Pollution Research, 17 (2010) 1197-1206.

[20] D.A. Wood, C. Nwaoha, B.F. Towler, Journal of Natural Gas Science and Engineering, 9 (2012) 196-208.

[21] K. Huang, J.B. Miller, G.W. Huber, J.A. Dumesic, C.T. Maravelias, Joule, 2 (2018) 349-365.

[22] J.B. Claridge, A.P.E. York, A.J. Brungs, C. Marquez-Alvarez, J. Sloan, S.C. Tsang, M.L.H. Green, Journal of Catalysis, 180 (1998) 85-100.

[23] D. Li, Y. Nakagawa, K. Tomishige, Applied Catalysis A: General, 408 (2011) 1-24.

[24] S.D. Angeli, G. Monteleone, A. Giaconia, A.A. Lemonidou, International Journal of Hydrogen Energy, 39 (2014) 1979-1997.

[25] S. Sengodan, R. Lan, J. Humphreys, D. Du, W. Xu, H. Wang, S. Tao, Renewable and Sustainable Energy Reviews, 82 (2018) 761-780.

[26] D.J. Wilhelm, D.R. Simbeck, A.D. Karp, R.L. Dickenson, Fuel Processing Technology, 71 (2001) 139-148.

[27] Q. Jiang, S. Faraji, D.A. Slade, S.M. Stagg-Williams, Chapter 11 - A Review of Mixed Ionic and Electronic Conducting Ceramic Membranes as Oxygen Sources for High-Temperature Reactors, in: S.T. Oyama, S.M. Stagg-Williams (Eds.) Membrane Science and Technology, Elsevier, Oxford, 2011, pp. 235-273.

[28] S.T. Oyama, P. Hacarlioglu, Y. Gu, D. Lee, International Journal of Hydrogen Energy, 37 (2012) 10444-10450.

[29] G.A. Olah, A. Goeppert, M. Czaun, G.K.S. Prakash, Journal of the American Chemical Society, 135 (2013) 648-650.

[30] O. Deutschmann, H. Knözinger, K. Kochloefl, T. Turek, Heterogeneous Catalysis and Solid Catalysts, 3. Industrial Applications, in: B. Elvers (Ed.) Ullmann's Encyclopedia of Industrial Chemistry, Wiley-VCH Verlag GmbH & Co. KGaA, Weinheim, 2011, pp. 551-567.

[31] H. Jahangiri, J. Bennett, P. Mahjoubi, K. Wilson, S. Gu, Catalysis Science & Technology, 4 (2014) 2210-2229.

[32] B. Christian Enger, R. Lødeng, A. Holmen, Applied Catalysis A: General, 346 (2008) 1-27.

[33] Y.J.O. Asencios, E.M. Assaf, Fuel Processing Technology, 106 (2013) 247-252.

[34] R. Dębek, M. Motak, T. Grzybek, M.E. Galvez, P. Da Costa, Catalysts, 7 (2017) 32.

[35] A. Albarazi, M.E. Gálvez, P. Da Costa, Catalysis Communications, 59 (2015) 108-112.

[36] J. Ma, N. Sun, X. Zhang, N. Zhao, F. Xiao, W. Wei, Y. Sun, Catalysis Today, 148 (2009) 221-231.

[37] C.-j. Liu, J. Ye, J. Jiang, Y. Pan, ChemCatChem, 3 (2011) 529-541.

[38] J. Gao, Z. Hou, H. Lou, X. Zheng, Chapter 7 - Dry (CO_2) Reforming, in: D. Shekhawat, J.J. Spivey, D.A. Berry (Eds.) Fuel Cells: Technologies for Fuel Processing, Elsevier, Amsterdam, 2011, pp. 191-221.

[39] V.C.H. Kroll, H.M. Swaan, C. Mirodatos, Journal of Catalysis, 161 (1996) 409-422.

[40] J. Zhang, H. Wang, A.K. Dalai, Applied Catalysis A: General, 339 (2008) 121-129.

[41] X. Cai, Y.H. Hu, Energy Science & Engineering, 7 (2019) 4-29.

[42] H.-S. Roh, K.-W. Jun, Catalysis Surveys from Asia, 12 (2008) 239-252.

[43] A.F. Lucrédio, J.M. Assaf, E.M. Assaf, Biomass and Bioenergy, 60 (2014) 8-17.

[44] N. Habibi, H. Arandiyan, M. Rezaei, RSC Advances, 6 (2016) 29576-29585.

[45] J. Guo, H. Lou, H. Zhao, D. Chai, X. Zheng, Applied Catalysis A: General, 273 (2004) 75-82.

[46] H. Özdemir, M.A.F. Öksüzömer, M.A. Gürkaynak, Fuel, 116 (2014) 63-70.

[47] M. García-Diéguez, C. Herrera, M.Á. Larrubia, L.J. Alemany, Catalysis Today, 197 (2012) 50-57.

[48] L. Li, L.-m. Zhang, Y.-h. Zhang, J.-l. Li, Journal of Fuel Chemistry and Technology, 43 (2015) 315-322.

[49] A.P. Tathod, N. Hayek, D. Shpasser, D.S.A. Simakov, O.M. Gazit, Applied Catalysis B: Environmental, 249 (2019) 106-115.

[50] D. Pakhare, J. Spivey, Chemical Society Reviews, 43 (2014) 7813-7837.

[51] C. Papadopoulou, H. Matralis, X. Verykios, Utilization of Biogas as a Renewable Carbon Source: Dry Reforming of Methane, in: L. Guczi, A. Erdôhelyi (Eds.) Catalysis for Alternative Energy Generation, Springer New York, New York, NY, 2012, pp. 57-127.

[52] B.A. Rosen, S. Singh, Fossil Fuels: Coke-Resistant Nanomaterials for Gas-to-Liquid (GTL) Fuels, in: B. Raj, M. Van de Voorde, Y. Mahajan (Eds.) Nanotechnology for Energy Sustainability, Wiley-VCH Verlag GmbH & Co. KGaA, Weinheim, 2017, pp. 59-82.

[53] X. Yu, N. Wang, W. Chu, M. Liu, Chemical Engineering Journal, 209 (2012) 623-632.

[54] Q. Zhang, K. Long, J. Wang, T. Zhang, Z. Song, Q. Lin, International Journal of Hydrogen Energy, 42 (2017) 14103-14114.

[55] T.E. Klimova, D. Valencia, J.A. Mendoza-Nieto, P. Hernández-Hipólito, Journal of Catalysis, 304 (2013) 29-46.

[56] J. Guo, Z. Hou, J. Gao, X. Zheng, Chinese Journal of Catalysis, 28 (2007) 22-26.

[57] S. Arora, R. Prasad, RSC Advances, 6 (2016) 108668-108688.

[58] Y. Gao, J. Jiang, Y. Meng, F. Yan, A. Aihemaiti, Energy Conversion and Management, 171 (2018) 133-155.

[59] Exxon reaffirms Blue Whale commitment, The Oil & Gas Year, (2017).

[60] S. Wang, G.Q. Lu, G.J. Millar, Energy & Fuels, 10 (1996) 896-904.

[61] T.D. Gould, A. Izar, A.W. Weimer, J.L. Falconer, J.W. Medlin, ACS Catalysis, 4 (2014) 2714-2717.

[62] J.H. Edwards, A.M. Maitra, Fuel Processing Technology, 42 (1995) 269-289.

[63] M.D. Argyle, C.H. Bartholomew, Catalysts, 5 (2015) 145.

[64] D. Pakhare, C. Shaw, D. Haynes, D. Shekhawat, J. Spivey, Journal of CO_2 Utilization, 1 (2013) 37-42.

[65] D. Liu, X.Y. Quek, W.N.E. Cheo, R. Lau, A. Borgna, Y. Yang, Journal of Catalysis, 266 (2009) 380-390.

[66] A.N. Şener, M.E. Günay, A. Leba, R. Yıldırım, Catalysis Today, 299 (2018) 289-302.

[67] P. Djinović, I.G.O. Črnivec, J. Batista, J. Levec, A. Pintar, Chemical Engineering and Processing: Process Intensification, 50 (2011) 1054-1062.

[68] C. Crisafulli, S. Scirè, S. Minicò, L. Solarino, Applied Catalysis A: General, 225 (2002) 1-9.

[69] J.R. Rostrupnielsen, J.H.B. Hansen, Journal of Catalysis, 144 (1993) 38-49.

[70] P. Frontera, A. Macario, A. Aloise, P.L. Antonucci, G. Giordano, J.B. Nagy, Catalysis Today, 218-219 (2013) 18-29.

[71] N.A.K. Aramouni, J.G. Touma, B.A. Tarboush, J. Zeaiter, M.N. Ahmad, Renewable and Sustainable Energy Reviews, 82 (2018) 2570-2585.

[72] Y.H. Hu, E. Ruckenstein, Catalytic Conversion of Methane to Synthesis Gas by Partial Oxidation and CO_2 Reforming, in: H. Knüpffer (Ed.) Advances in Catalysis, Academic Press, Oxford, 2004, pp. 297-345.

[73] M.C.J. Bradford, M.A. Vannice, Applied Catalysis A: General, 142 (1996) 73-96.

[74] Y.H. Hu, E. Ruckenstein, Catalysis Reviews, 44 (2002) 423-453.

[75] R.-j. Zhang, G.-f. Xia, M.-f. Li, Y. Wu, H. Nie, D.-d. Li, Journal of Fuel Chemistry and Technology, 43 (2015) 1359-1365.

[76] D. Li, M. Koike, L. Wang, Y. Nakagawa, Y. Xu, K. Tomishige, ChemSusChem, 7 (2013) 510-522.

[77] K. Tomishige, O. Yamazaki, Y. Chen, K. Yokoyama, X. Li, K. Fujimoto, Catalysis Today, 45 (1998) 35-39.

[78] S.B. Tang, F.L. Qiu, S.J. Lu, Catalysis Today, 24 (1995) 253-255.

[79] J.-E. Min, Y.-J. Lee, H.-G. Park, C. Zhang, K.-W. Jun, Journal of Industrial and Engineering Chemistry, 26 (2015) 375-383.

[80] M. Abdollahifar, M. Haghighi, A.A. Babaluo, S.K. Talkhoncheh, Ultrasonics Sonochemistry, 31 (2016) 173-183.

[81] G. Zhang, J. Liu, Y. Xu, Y. Sun, International Journal of Hydrogen Energy, 43 (2018) 15030-15054.

[82] A. Tribalis, G. Panagiotou, K. Bourikas, L. Sygellou, S. Kennou, S. Ladas, A. Lycourghiotis, C. Kordulis, Catalysts, 6 (2016) 11.

[83] H. Liu, D. Wierzbicki, R. Debek, M. Motak, T. Grzybek, P. Da Costa, M.E. Gálvez, Fuel, 182 (2016) 8-16.

[84] Y. Kathiraser, W. Thitsartarn, K. Sutthiumporn, S. Kawi, The Journal of Physical Chemistry C, 117 (2013) 8120-8130.

[85] V.A. Tsipouriari, X.E. Verykios, Journal of Catalysis, 187 (1999) 85-94.

[86] J. Guo, J. Gao, B. Chen, Z. Hou, J. Fei, H. Lou, X. Zheng, International Journal of Hydrogen Energy, 34 (2009) 8905-8911.

[87] V.A. Suárez-Toriello, C.E. Santolalla-Vargas, J.A. de los Reyes, A. Vázquez-Zavala, M. Vrinat, C. Geantet, Journal of Molecular Catalysis A: Chemical, 404–405 (2015) 36-46.

[88] P. Castillo-Villalón, J. Ramirez, J.A. Vargas-Luciano, Journal of Catalysis, 320 (2014) 127-136.

[89] Z. Bian, Z. Xin, X. Meng, M. Tao, Y. Lv, J. Gu, Industrial & Engineering Chemistry Research, 56 (2017) 2383-2392.

[90] B. Li, X. Qian, X. Wang, International Journal of Hydrogen Energy, 40 (2015) 8081-8092.

[91] H. Liu, Y. Li, H. Wu, T. Miyake, D. He, International Journal of Hydrogen Energy, 38 (2013) 15200-15209.

[92] W. Li, Z. Zhao, F. Ding, X. Guo, G. Wang, ACS Sustainable Chemistry & Engineering, 3 (2015) 3461-3476.

[93] H.-P. Ren, Q.-Q. Hao, W. Wang, Y.-H. Song, J. Cheng, Z.-W. Liu, Z.-T. Liu, J. Lu, Z. Hao, International Journal of Hydrogen Energy, 39 (2014) 11592-11605.

[94] H.-P. Ren, Y.-H. Song, Q.-Q. Hao, Z.-W. Liu, W. Wang, J.-G. Chen, J. Jiang, Z.-T. Liu, Z. Hao, J. Lu, Industrial & Engineering Chemistry Research, 53 (2014) 19077-19086.

[95] H.-P. Ren, Q.-Q. Hao, S.-Y. Ding, Y.-Z. Zhao, M. Zhu, S.-P. Tian, Q. Ma, W.-Q. Song, Z. Miao, Z.-T. Liu, Industrial & Engineering Chemistry Research, 57 (2018) 16257-16263.

[96] M.H. Amin, K. Mantri, J. Newnham, J. Tardio, S.K. Bhargava, Applied Catalysis B: Environmental, 119-120 (2012) 217-226.

[97] J. Newnham, K. Mantri, M.H. Amin, J. Tardio, S.K. Bhargava, International Journal of Hydrogen Energy, 37 (2012) 1454-1464.

[98] S. Liu, L. Guan, J. Li, N. Zhao, W. Wei, Y. Sun, Fuel, 87 (2008) 2477-2481.

[99] Y.H. Hu, E. Ruckenstein, Catalysis Letters, 36 (1996) 145-149.

[100] R. Zanganeh, M. Rezaei, A. Zamaniyan, International Journal of Hydrogen Energy, 38 (2013) 3012-3018.

[101] F. Pompeo, D. Gazzoli, N.N. Nichio, International Journal of Hydrogen Energy, 34 (2009) 2260-2268.

[102] D. Liu, R. Lau, A. Borgna, Y. Yang, Applied Catalysis A: General, 358 (2009) 110-118.

[103] J. Chen, Q. Wu, J. Zhang, J. Zhang, Fuel, 87 (2008) 2901-2907.

[104] H.V. Fajardo, A.O. Martins, R.M. de Almeida, L.K. Noda, L.F.D. Probst, N.L.V. Carreño, A. Valentini, Materials Letters, 59 (2005) 3963-3967.

[105] R.K. Singha, A. Yadav, A. Agrawal, A. Shukla, S. Adak, T. Sasaki, R. Bal, Applied Catalysis B: Environmental, 191 (2016) 165-178.

[106] J. Huang, R. Ma, T. Huang, A. Zhang, W. Huang, Journal of Natural Gas Chemistry, 20 (2011) 465-470.

[107] J. Huang, R. Ma, Z. Gao, C. Shen, W. Huang, Chinese Journal of Catalysis, 33 (2012) 637-644.

[108] X. Zhu, P. Huo, Y.-p. Zhang, D.-g. Cheng, C.-j. Liu, Applied Catalysis B: Environmental, 81 (2008) 132-140.

[109] J. Ni, L. Chen, J. Lin, S. Kawi, Nano Energy, 1 (2012) 674-686.

[110] J.-S. Chang, S.-E. Park, H. Chon, Applied Catalysis A: General, 145 (1996) 111-124.

[111] B.M. Nagaraja, D.A. Bulushev, S. Beloshapkin, J.R.H. Ross, Catalysis Today, 178 (2011) 132-136.

[112] I. Luisetto, S. Tuti, C. Battocchio, S. Lo Mastro, A. Sodo, Applied Catalysis A: General, 500 (2015) 12-22.

[113] V. García, J.J. Fernández, W. Ruíz, F. Mondragón, A. Moreno, Catalysis Communications, 11 (2009) 240-246.

[114] W. Chen, G. Zhao, Q. Xue, L. Chen, Y. Lu, Applied Catalysis B: Environmental, 136-137 (2013) 260-268.

[115] Z. Hao, Q. Zhu, Z. Jiang, B. Hou, H. Li, Fuel Processing Technology, 90 (2009) 113-121.

[116] J. Zhu, X. Peng, L. Yao, X. Deng, H. Dong, D. Tong, C. Hu, International Journal of Hydrogen Energy, 38 (2013) 117-126.

[117] M. Zhang, S. Ji, L. Hu, F. Yin, C. Li, H. Liu, Chinese Journal of Catalysis, 27 (2006) 777-781.

[118] K.-M. Kang, H.-W. Kim, I.-W. Shim, H.-Y. Kwak, Fuel Processing Technology, 92 (2011) 1236-1243.

[119] H.-S. Roh, H.S. Potdar, K.-W. Jun, J.-W. Kim, Y.-S. Oh, Applied Catalysis A: General, 276 (2004) 231-239.

[120] W.-J. Jang, D.-W. Jeong, J.-O. Shim, H.-S. Roh, I.H. Son, S.J. Lee, International Journal of Hydrogen Energy, 38 (2013) 4508-4512.

[121] E. Ruckenstein, Y.H. Hu, Applied Catalysis A: General, 133 (1995) 149-161.

[122] L. Xu, H. Song, L. Chou, Applied Catalysis B: Environmental, 108-109 (2011) 177-190.

[123] X. Fan, Z. Liu, Y.-A. Zhu, G. Tong, J. Zhang, C. Engelbrekt, J. Ulstrup, K. Zhu, X. Zhou, Journal of Catalysis, 330 (2015) 106-119.

[124] M. Yu, K. Zhu, Z. Liu, H. Xiao, W. Deng, X. Zhou, Applied Catalysis B: Environmental, 148-149 (2014) 177-190.

[125] Z. Li, L. Mo, Y. Kathiraser, S. Kawi, ACS Catalysis, 4 (2014) 1526-1536.

[126] B. Djebarri, V.M. Gonzalez-Delacruz, D. Halliche, K. Bachari, A. Saadi, A. Caballero, J.P. Holgado, O. Cherifi, Reaction Kinetics, Mechanisms and Catalysis, 111 (2014) 259-275.

[127] Hydrotalcite – PURAL® MG (Product information), Sasol Germany GmbH.

[128] N. Wang, X. Yu, Y. Wang, W. Chu, M. Liu, Catalysis Today, 212 (2013) 98-107.

[129] A. Kvick, X-Ray Diffraction, Materials Science Applications, 2016, pp. 648-655.

[130] N. Kumar, S. Kumbhat, Characterization Tools for Nanomaterials, in: A. Lekhwani (Ed.) Essentials in Nanoscience and Nanotechnology, John Wiley & Sons, Inc, New Jersey, 2016, pp. 77-148.

[131] A.K. Singh, Chapter 4 - Experimental Methodologies for the Characterization of Nanoparticles, in: A.K. Singh (Ed.) Engineered Nanoparticles, Academic Press, Boston, 2016, pp. 125-170.

[132] S. Brunauer, P.H. Emmett, E. Teller, Journal of the American Chemical Society, 60 (1938) 309-319.

[133] M. Thommes, K. Kaneko, V. Neimark Alexander, P. Olivier James, F. Rodriguez-Reinoso, J. Rouquerol, S.W. Sing Kenneth, Pure and Applied Chemistry, 87 (2015) 1051.

[134] S. Storck, H. Bretinger, W.F. Maier, Applied Catalysis A: General, 174 (1998) 137-146.

[135] M. Fadoni, L. Lucarelli, Temperature programmed desorption, reduction, oxidation and flow chemisorption for the characterisation of heterogeneous catalysts. Theoretical aspects, instrumentation and applications, in: A. Dąbrowski (Ed.) Studies in Surface Science and Catalysis, Elsevier, Amsterdam, 1999, pp. 177-225.

[136] S. Oswald, X-Ray Photoelectron Spectroscopy in Analysis of Surfaces in: R.A. Meyers (Ed.) Encyclopedia of Analytical Chemistry, John Wiley & Sons, Ltd, New Jersey, 2013.

[137] A.M. Venezia, Catalysis Today, 77 (2003) 359-370.

[138] R.A. Schoonheydt, Chemical Society Reviews, 39 (2010) 5051-5066.

[139] B. Scheffer, J.J. Heijeinga, J.A. Moulijn, The Journal of Physical Chemistry, 91 (1987) 4752-4759.

[140] C. Jiménez-González, Z. Boukha, B. de Rivas, J.J. Delgado, M.Á. Cauqui, J.R. González-Velasco, J.I. Gutiérrez-Ortiz, R. López-Fonseca, Applied Catalysis A: General, 466 (2013) 9-20.

[141] S.J. Pennycook, A.R. Lupini, M. Varela, A. Borisevich, Y. Peng, M.P. Oxley, K. Van Benthem, M.F. Chisholm, Scanning Transmission Electron Microscopy

for Nanostructure Characterization, in: W. Zhou, Z.L. Wang (Eds.) Scanning Microscopy for Nanotechnology: Techniques and Applications, Springer New York, New York, NY, 2007, pp. 152-191.

[142] Y. Kotaka, Applied Physics Letters, 101 (2012) 133107.

[143] R. Ishikawa, E. Okunishi, H. Sawada, Y. Kondo, F. Hosokawa, E. Abe, Nature Materials, 10 (2011) 278.

[144] X. Zhao, Y. Cao, H. Li, J. Zhang, L. Shi, D. Zhang, RSC Advances, 7 (2017) 4735-4745.

[145] E. Okunishi, H. Sawada, Y. Kondo, Micron, 43 (2012) 538-544.

[146] D.E. Jesson, S.J. Pennycook, Proceedings of the Royal Society of London. Series A: Mathematical and Physical Sciences, 449 (1995) 273-293.

[147] O.L. Krivanek, M.F. Chisholm, V. Nicolosi, T.J. Pennycook, G.J. Corbin, N. Dellby, M.F. Murfitt, C.S. Own, Z.S. Szilagyi, M.P. Oxley, S.T. Pantelides, S.J. Pennycook, Nature, 464 (2010) 571.

[148] P.D. Nellist, S.J. Pennycook, The principles and interpretation of annular dark-field Z-contrast imaging, in: P.W. Hawkes (Ed.) Advances in Imaging and Electron Physics, Elsevier, Amsterdam, 2000, pp. 147-203.

[149] Q.L.M. Ha, U. Armbruster, H. Atia, M. Schneider, H. Lund, G. Agostini, J. Radnik, H.T. Vuong, A. Martin, Catalysts, 7 (2017) 157.

[150] A. Ananth, D. Gregory, Y. Mok, Applied Sciences, 5 (2015) 344.

[151] J. De Waele, V.V. Galvita, H. Poelman, C. Detavernier, J.W. Thybaut, Catalysis Science & Technology, 7 (2017) 3715-3727.

[152] P.A. Kumar, M.P. Reddy, B. Hyun-Sook, H.H. Phil, Catalysis Letters, 131 (2009) 85-97.

[153] H.A. Prescott, Z.-J. Li, E. Kemnitz, A. Trunschke, J. Deutsch, H. Lieske, A. Auroux, Journal of Catalysis, 234 (2005) 119-130.

[154] Y. Ono, H. Hattori, Preparation and Catalytic Properties of Solid Base Catalysts — II. Specific Materials for Solid Bases, Solid Base Catalysis, Springer Berlin Heidelberg, Berlin, Heidelberg, 2011, pp. 157-218.

[155] T. Stanimirova, I. Vergilov, G. Kirov, N. Petrova, Journal of Materials Science, 34 (1999) 4153-4161.

[156] K. Takehira, T. Kawabata, T. Shishido, K. Murakami, T. Ohi, D. Shoro, M. Honda, K. Takaki, Journal of Catalysis, 231 (2005) 92-104.

[157] M. Jafarbegloo, A. Tarlani, A.W. Mesbah, J. Muzart, S. Sahebdelfar, Catalysis Letters, 146 (2016) 238-248.

[158] C. Jiménez-González, Z. Boukha, B. de Rivas, J.R. González-Velasco, J.I. Gutiérrez-Ortiz, R. López-Fonseca, Energy & Fuels, 28 (2014) 7109-7121.

[159] J. Escobar, J. Antonio De Los Reyes, T. Viveros, Applied Catalysis A: General, 253 (2003) 151-163.

[160] S. Damyanova, B. Pawelec, K. Arishtirova, J.L.G. Fierro, International Journal of Hydrogen Energy, 37 (2012) 15966-15975.

[161] Y. Liu, G. Liu, C. Zhang, W. Qiu, S. Yi, V. Chernikova, Z. Chen, Y. Belmabkhout, O. Shekhah, M. Eddaoudi, W. Koros, Advanced Science, 5 (2018) 1800982.

[162] C. Li, Y.-W. Chen, Thermochimica Acta, 256 (1995) 457-465.

[163] J.L. Rogers, M.C. Mangarella, A.D. D'Amico, J.R. Gallagher, M.R. Dutzer, E. Stavitski, J.T. Miller, C. Sievers, ACS Catalysis, 6 (2016) 5873-5886.

[164] A.F. Lucrédio, J.D.A. Bellido, E.M. Assaf, Applied Catalysis A: General, 388 (2010) 77-85.

[165] Z. Jiang, J. Su, M.O. Jones, H. Shi, T. Xiao, P.P. Edwards, Energy & Fuels, 23 (2009) 1634-1639.

[166] L. Zhang, Q. Zhang, Y. Liu, Y. Zhang, Applied Surface Science, 389 (2016) 25-33.

[167] NIST X-ray Photoelectron Spectroscopy Database: Version 3.4 (Web Version), National Institute of Standards and Technology, Gaithersburg(2002).

[168] G.P. Szijjártó, Z. Pászti, I. Sajó, A. Erdőhelyi, G. Radnóczi, A. Tompos, Journal of Catalysis, 305 (2013) 290-306.

[169] A. Cimino, D. Gazzoli, V. Indovina, G. Moretti, M. Occhiuzzi, F. Pepe, Topics in Catalysis, 8 (1999) 171-178.

[170] E. Ruckenstein, Y. Hang Hu, Applied Catalysis A: General, 183 (1999) 85-92.

[171] Z. Boukha, C. Jiménez-González, B. de Rivas, J.R. González-Velasco, J.I. Gutiérrez-Ortiz, R. López-Fonseca, Applied Catalysis B: Environmental, 158–159 (2014) 190-201.

[172] E. Heracleous, A.F. Lee, K. Wilson, A.A. Lemonidou, Journal of Catalysis, 231 (2005) 159-171.

[173] A. Zecchina, G. Spoto, S. Coluccia, E. Guglielminotti, Journal of the Chemical Society, Faraday Transactions 1: Physical Chemistry in Condensed Phases, 80 (1984) 1875-1889.

[174] Z. Skoufa, G. Xantri, E. Heracleous, A.A. Lemonidou, Applied Catalysis A: General, 471 (2014) 107-117.

[175] M. Luneau, E. Gianotti, F.C. Meunier, C. Mirodatos, E. Puzenat, Y. Schuurman, N. Guilhaume, Applied Catalysis B: Environmental, 203 (2017) 289-299.

[176] M. Wu, D.M. Hercules, The Journal of Physical Chemistry, 83 (1979) 2003-2008.

[177] I. Pettiti, D. Gazzoli, P. Benito, G. Fornasari, A. Vaccari, RSC Advances, 5 (2015) 82282-82291.

[178] N.H. Elsayed, N.R.M. Roberts, B. Joseph, J.N. Kuhn, Applied Catalysis B: Environmental, 179 (2015) 213-219.

[179] M.-S. Fan, A.Z. Abdullah, S. Bhatia, ChemCatChem, 1 (2009) 192-208.

[180] J.-M. Lavoie, Frontiers in Chemistry, 2 (2014).

[181] Q.L.M. Ha, U. Armbruster, C. Kreyenschulte, H. Atia, H. Lund, H.T. Vuong, S. Wohlrab, Catalysis Today, 334 (2019) 203-214.

[182] Q. Wei, Y. Zhou, C. Xu, Y. Liu, Effects of Citric Acid as a Chelating Agent on the Performance of a Heavy Oil Hydrotreatment Catalyst, in: Y.H. Hu, X. Ma, E.B. Fox, X. Guo (Eds.) Production and Purification of Ultraclean Transportation Fuels, American Chemical Society, Washington, DC, 2011, pp. 3-13.

[183] D. He, Y. Luo, Y. Tao, V. Strezov, P. Nelson, Y. Jiang, Energy & Fuels, 31 (2017) 2353-2359.

[184] I. Rivas, J. Alvarez, E. Pietri, M.J. Pérez-Zurita, M.R. Goldwasser, Catalysis Today, 149 (2010) 388-393.

[185] V. Celorrio, E. Dann, L. Calvillo, D.J. Morgan, S.R. Hall, D.J. Fermin, ChemElectroChem, 3 (2016) 283-291.

[186] J.A. Mendoza-Nieto, F. Robles-Méndez, T.E. Klimova, Catalysis Today, 250 (2015) 47-59.

[187] A. Dugué, L. Cormier, O. Dargaud, L. Galoisy, G. Calas, Journal of the American Ceramic Society, 95 (2012) 3483-3489.

[188] A. Zecchina, E. Garrone, E. Guglielminotti, Structural characterization of surface species and surface sites by conventional optical spectroscopies, in: G.C. Bond, G. Webb (Eds.) Catalysis: Volume 6, The Royal Society of Chemistry, London, 1983, pp. 90-143.

[189] S.L. González-Cortés, I. Aray, S.M.A. Rodulfo-Baechler, C.A. Lugo, H.L. Del Castillo, A. Loaiza-Gil, F.E. Imbert, H. Figueroa, W. Pernía, A. Rodríguez, O. Delgado, R. Casanova, J. Mendialdua, F. Rueda, Journal of Materials Science, 42 (2007) 6532-6540.

[190] A. Zecchina, G. Spoto, S. Coluccia, E. Guglielminotti, Journal of the Chemical Society, Faraday Transactions 1: Physical Chemistry in Condensed Phases, 80 (1984) 1891-1901.

[191] M. Che, L. Bonneviot, pac, 60 (1988) 1369.

[192] V. Indovina, D. Cordischi, S. Febbraro, M. Occhiuzzi, Journal of the Chemical Society, Faraday Transactions 1: Physical Chemistry in Condensed Phases, 81 (1985) 37-48.

[193] D. Li, R. Li, M. Lu, X. Lin, Y. Zhan, L. Jiang, Applied Catalysis B: Environmental, 200 (2017) 566-577.

[194] M. Argyle, C. Bartholomew, Catalysts, 5 (2015) 145.

[195] A.P.E. York, T.c. Xiao, M.L.H. Green, J.B. Claridge, Catalysis Reviews - Science and Engineering, 49 (2007) 511-560.

[196] Y.H. Hu, E. Ruckenstein, Catalysis Letters, 43 (1997) 71-77.

[197] Y.-g. Chen, K. Tomishige, K. Yokoyama, K. Fujimoto, Applied Catalysis A: General, 165 (1997) 335-347.

[198] S. Wang, G.Q.M. Lu, Applied Catalysis B: Environmental, 16 (1998) 269-277.

[199] B. Steinhauer, M.R. Kasireddy, J. Radnik, A. Martin, Applied Catalysis A: General, 366 (2009) 333-341.

[200] H. Jiang, H. Li, H. Xu, Y. Zhang, Fuel Processing Technology, 88 (2007) 988-995.

[201] G. Andreas, M. Lubow, S.S. A., D. Olaf, ChemCatChem, 10 (2018) 751-757.

[202] Y.H. Hu, E. Ruckenstein, Cat. Rev. - Sci. Eng., 44 (2002) 423-453.

[203] Y. Yang, W. Li, H. Xu, Reaction Kinetics and Catalysis Letters, 77 (2002) 155-162.

[204] F. Pompeo, N.N. Nichio, O.A. Ferretti, D. Resasco, International Journal of Hydrogen Energy, 30 (2005) 1399-1405.

[205] S. Damyanova, B. Pawelec, K. Arishtirova, J.L.G. Fierro, International Journal of Hydrogen Energy, 36 (2011) 10635-10647.

[206] M. Nemeth, D. Sranko, J. Karolyi, F. Somodi, Z. Schay, G. Safran, I. Sajo, A. Horvath, Catalysis Science & Technology, 7 (2017) 5386-5401.

[207] M. Kogler, E.-M. Köck, B. Klötzer, T. Schachinger, W. Wallisch, R. Henn, C.W. Huck, C. Hejny, S. Penner, The Journal of Physical Chemistry C, 120 (2016) 1795-1807.

[208] M. Menetrey, A. Markovits, C. Minot, Surface Science, 524 (2003) 49-62.

[209] A.S. Al-Fatesh, Y. Arafat, H. Atia, A.A. Ibrahim, Q.L.M. Ha, M. Schneider, M. M-Pohl, A.H. Fakeeha, Journal of CO_2 Utilization, 21 (2017) 395-404.

[210] B. Sarkar, R. Goyal, C. Pendem, T. Sasaki, R. Bal, Journal of Molecular Catalysis A: Chemical, 424 (2016) 17-26.

[211] G. Zhang, Y. Wang, X. Li, Y. Bai, L. Zheng, L. Wu, X. Han, Industrial & Engineering Chemistry Research, 57 (2018) 17076-17085.

[212] W. Wang, C. Su, R. Ran, Z. Shao, Journal of Power Sources, 196 (2011) 3855-3862.

[213] M.N. Younis, Z.O. Malaibari, W. Ahmad, S. Ahmed, Energy & Fuels, 32 (2018) 7054-7065.

[214] J. Guo, Z. Hou, J. Gao, X. Zheng, Fuel, 87 (2008) 1348-1354.

[215] A.T. Ashcroft, A.K. Cheetham, M.L.H. Green, P.D.F. Vernon, Nature, 352 (1991) 225.

[216] L. Guczi, G. Stefler, O. Geszti, I. Sajó, Z. Pászti, A. Tompos, Z. Schay, Applied Catalysis A: General, 375 (2010) 236-246.

[217] S. Yasyerli, S. Filizgok, H. Arbag, N. Yasyerli, G. Dogu, International Journal of Hydrogen Energy, 36 (2011) 4863-4874.

[218] A. Horváth, G. Stefler, O. Geszti, A. Kienneman, A. Pietraszek, L. Guczi, Catalysis Today, 169 (2011) 102-111.

[219] J. Károlyi, M. Németh, C. Evangelisti, G. Sáfrán, Z. Schay, A. Horváth, F. Somodi, Journal of Industrial and Engineering Chemistry, 58 (2018) 189-201.

Appendix

Layer distance change in section 5.1

Such change is illustrated in STEM-ABF image of a Ni/$NiO_{1-\delta}$ particle from Ni/$Mg_{1.3}AlO_x$ spent catalyst. The lattice distance change from 0.20 nm to 0.24 nm indicates the existence of both Ni (101) and NiO (222) in a particle.

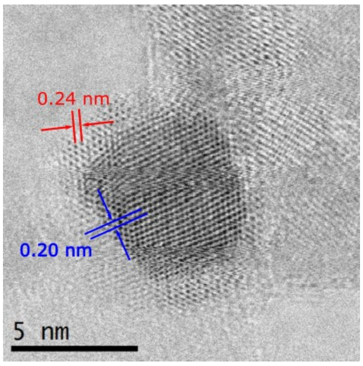

Figure S. 1. STEM-ABF image with lattice distance values of an individual particle on spent Ni/$Mg_{1.3}AlO_x$ mainly covered by $NiO_{1-\delta}$.

XRD patterns of the references NiO and $LaNiO_3$ used in chapter 4 and 5

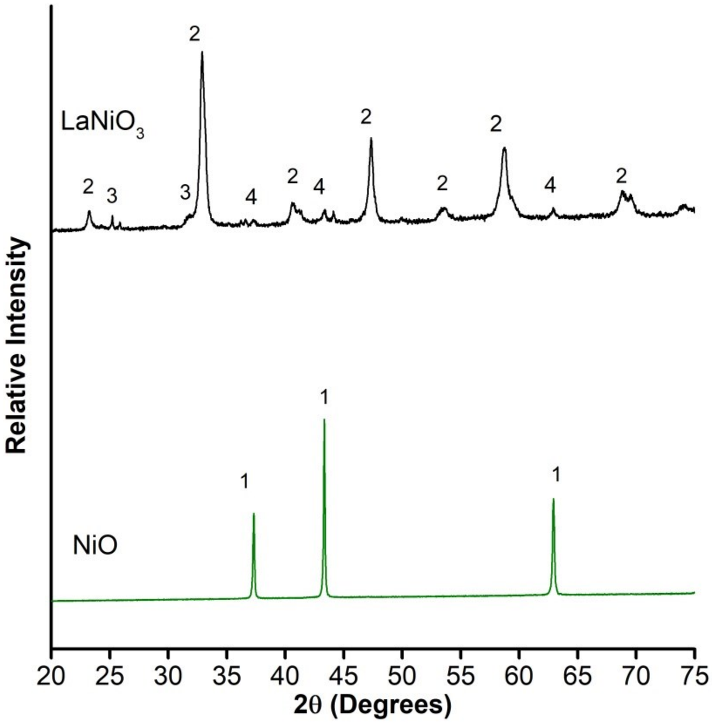

Figure S. 2. XRD patterns of the references NiO and $LaNiO_3$. Phase symbols and ICDD file Number: NiO (01-078-0643) (1), $LaNiO_3$ (00-033-0711) (2), La_2NiO_4 (00-034-0984) (3), NiO (01-075-0197) (4)

STEM characterization of Ni/$Mg_{1.3}AlO_x$ after reduction at 700 °C for 1.5 hours

STEM images of reduced Ni/$Mg_{1.3}AlO_x$ are shown exemplarily below. This reduced sample Ni/$Mg_{1.3}AlO_x$ has an inhomogeneous Ni distribution which may be due to NiO domains already observed in UV-Vis spectra of the precursory calcined sample (Figure 5.3b). Such NiO domains may result in larger Ni particles (5 nm) after 1.5 hour reduction at 700 °C and might be the origin of the serious agglomeration after additional 8 hours in DRM. Unlikely, the CA- and La-modified samples show less NiO lattices after calcination, which might explain the even distribution of Ni species at stable dispersion after both reduction and reaction (Figure 5.5).

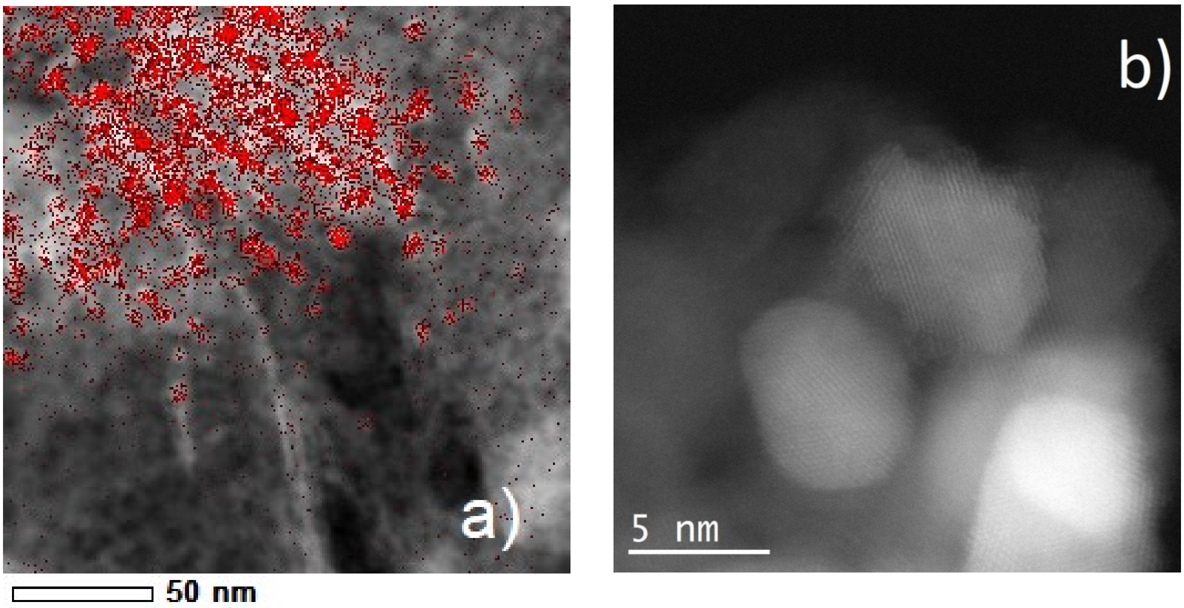

Figure S. 3. a) EDX elemental maps overlaid on STEM-HAADF image of reduced Ni/ $Mg_{1.3}AlO_x$ and b) its STEM-HAADF image focusing on Ni particles. Reduction conditions: 700 °C, 1.5 h

Representative Gas Chromatogram

The gas compositions before and after every reaction were analysed by an on-line gas chromatography (Agilent 6890) equipped with flame ionization detector (FID) and thermal conductivity detector (TCD) for analysis of hydrocarbons and permanent gases, respectively. Figure S. 4 illustrates two chromatogram examples from one representative DRM run. Before the reaction, there are CH_4 recorded by both TCD and FID, He and CO_2 in TCD. After feeding these compounds into the reactor, H_2 and CO were additionally recorded in TCD.

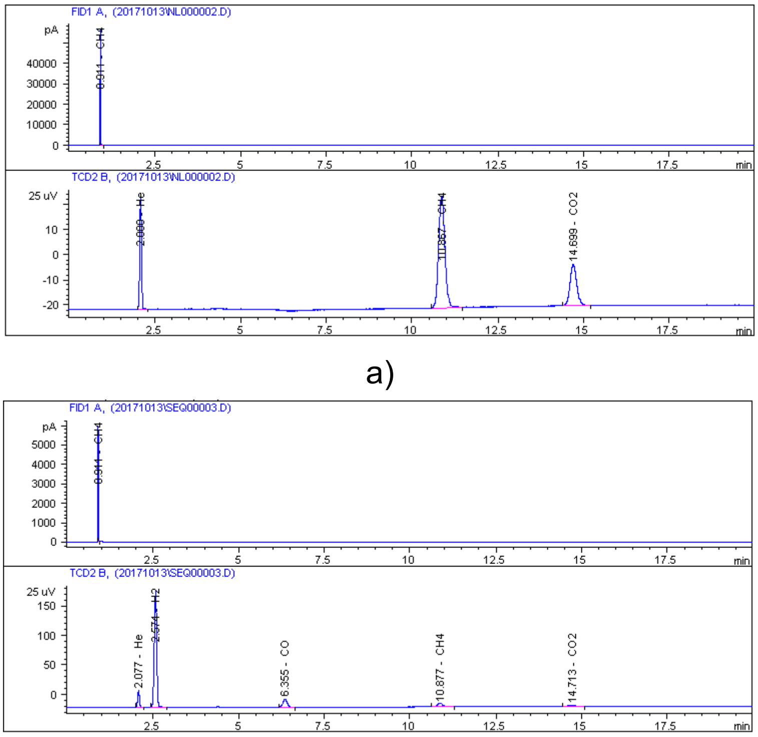

a)

b)

Figure S. 4. Representative chromatograms of the gas mixture a) before and b) after reaction

Representative DRM setup pictures

Figure S. 5. The oven with fixed bed reactor for DRM

Scientific publications

Parts of this thesis have been published:

Journal articles fully related to this work

Ha, Q. L. M.; Armbruster, U.; Kreyenschulte, C.; Atia, H.; Lund, H.; Vuong, H.; Wohlrab S., Stabilization of low nickel content catalysts with lanthanum and by citric acid assisted preparation to suppress deactivation in dry reforming of methane. *Catalysis Today* **2019**, 334, 203-214.

Ha, Q. L. M.; Armbruster, U.; Atia, H.; Schneider, M.; Lund, H.; Agostini, G.; Radnik, J.; Vuong, H. T.; Martin, A., Development of Active and Stable Low Nickel Content Catalysts for Dry Reforming of Methane. *Catalysts* **2017**, *7* (5), 157.

Additional articles

Al-Fatesh, A. S.; Arafat, Y.; Atia, H.; Ibrahim, A. A.; Ha, Q. L. M.; Schneider, M.; M-Pohl, M.; Fakeeha, A. H., CO_2-reforming of methane to produce syngas over Co-Ni/SBA-15 catalyst: Effect of support modifiers (Mg, La and Sc) on catalytic stability. *Journal of CO_2 Utilization* **2017**, *21*, 395-404.

Contributions in conferences

Oral presentations

Ha, Q. L. M.; Armbruster, U.; Wohlrab S., Promotion study on Ni catalysts for CH_4 rich DRM. 2nd RoHan DAAD SDG Workshop 2018 “Catalysis toward sustainable chemical industry”, Hanoi (Vietnam), September 17 - 21, **2018**.

Ha, Q. L. M.; Armbruster, U.; Wohlrab S., Development of low nickel content powder and structured catalysts for dry reforming of methane. 12th International Symposium on the "Scientific Bases for the Preparation of Heterogeneous Catalysts", Louvain-La-Neuve (Belgium), July 8 - 12, **2018**.

Ha, Q. L. M.; Armbruster, U.; Martin A., Development of active and stable low nickel content catalysts for dry reforming of methane. 13th European Congress on Catalysis (EUROPACAT 2017), Florence (Italy), August 27 - 31, **2017**.

Ha, Q. L. M.; Armbruster, U.; Martin A., Deactivation/Stabilization of low Ni content catalyst in dry reforming. 1st RoHan DAAD SDG Summer School 2017 “Challenges in Vietnamese Society – Impact of catalysis”, Rostock (Germany), May 01 - 12, **2017**.

Poster presentations

Ha, Q. L. M.; Armbruster, U., Deactivation and regeneration of low nickel content catalyst in methane dry reforming. Catalysis Fundamentals and Practice Summer School, Liverpool (UK), July 17 - 21, **2017**.

Ha, Q. L. M.; Armbruster, U.; Wohlrab S., Effect of Mg:Al ratio on performance of low nickel content catalysts for dry reforming of methane. ForschungsCampus, Rostock (Germany), November 23, **2017**.

Ha, Q. L. M.; Armbruster, U.; Martin A., The effect of support on perovskite catalysts for CH_4 dry reforming to synthesis syngas as fine chemicals feedstock. 11th international Congress on Catalysis and Fine Chemicals (CAFC-11), Lyon (France), September 05 – 08, **2016**.

Ha, Q. L. M.; Armbruster, U.; Martin A., The effect of support modification on perovskite catalysts for methane dry reforming with carbon dioxide. 49. Jahrestreffen Deutscher Katalytiker, Weimar (Germany), March 16 – 18, 2016.